Eidgenössische Technische Hochschule Zürich
Swiss Federal Institute of Technology Zurich

Prof. Dr. Božidar Stojadinović
Chair of Structural Dynamics and Earthquake Engineering
Institute of Structural Engineering
Department Civil, Environmental and Geomatic Engineering

Master's Thesis

Seismic Behavior of I-Shaped Unreinforced Masonry Walls with Soft-Layer Strip Bearings

Student:

Mr. Patrick Schönenberger

Supervisors:

Prof. Dr. Božidar Stojadinović

Dr. Nebojša Mojsilović

Advisor:

Mr. Miloš Petrović

Institute of Structural Engineering

Swiss Federal Institute of Technology

Zurich

30.06.2014

Abstract

So far the research of the seismic behavior of in-plane loaded unreinforced masonry (URM) walls concentrated almost exclusively on rectangular walls. But recent investigations as for example the one of Russel (2010) showed that flanges can significantly influence the seismic response of URM walls. Since rectangular URM walls are rather an exception in practice more sophisticated models are required to provide more economic seismic verifications. Furthermore often a soft-layer is applied to prevent moisture from rising in the wall. Also its influence has to be taken into account. Therefore the goal of this master's thesis is to characterize the seismic behavior, in particular the force and deformation capacity, of I-shaped URM walls with soft-layer strip (SLS) bearings.

In the first part of the thesis the general behavior of rectangular URM walls is investigated. Furthermore the theoretical modified effective pier model of Yi (2004) to predict the shear strength and failure mode of single-flanged URM walls is adopted for an I-shaped geometry to predict the behavior of the tests in the experimental part where an acceptable agreement to the results is found. Additionally a theoretical comparison of rectangular with I-shaped URM walls according to the effective pier model and its adapted modification for a cantilever boundary condition is presented.

In the second part of the thesis five tests on half scale I-shaped URM walls are conducted in the HIF laboratory of the ETH Zurich. The tests show that the application of a granulate SLS bearing leads to a reduced shear strength and an increased deformation capacity. Furthermore the soft-layer leads to an increased energy dissipation and less damage of the wall at corresponding displacements due to its load-distributing effect. The influence of an increase in the vertical load magnitude is clearly visible in the seismic response of the I-shaped URM walls with a higher shear strength and a reduced deformation capacity. It is also found that a higher level of precompression leads to a higher energy dissipation and a slightly higher damage of the granulate SLS bearing.

Since Vögeli (2014) tested equivalent rectangular walls the influence of the flanges can be investigated. In consideration of the different boundary condition of the rectangular and I-shaped tests it can be concluded that flanges definitely increase the shear strength and have also the potential to increase the deformation capacity. Although the energy dissipation is lower for I-shaped URM walls flanges can increase the seismic performance from a force-based as well as from a displacement-based point of view. This conclusion is further reinforced by the fact that the flanges do not affect the damage of the granulate SLS bearing compared to rectangular URM walls.

Acknowledgements

In awareness of the fact that writing is a solitary activity, the research in the scope of this master's thesis would not have been possible without the tremendous help of many people.

First of all I would like to thank my supervisors Božidar Stojadinović and Nebojša Mojsilović who offered me to gain a lot of valuable experiences in experimental research. I would like to express my gratitude for their support and guidance during this master's thesis.

I want to thank my advisor Miloš Petrović for his support in all organizational matters and his helpful advices based on his experiences of previous experimental tests.

It is a great pleasure to thank Jan Egeter who conducted the laboratory tests in collaboration with me. I really learned to appreciate his pragmatic manner in the laboratory and his patient and diligent work concerning the data evaluation. He was an awesome team mate and I appreciate his friendship throughout this master's thesis.

I would also like to express my deepest gratitude to Dominik Werne, Thomas Jaggi, Pius Herzog and Patrick Morph of the HIF laboratory team at ETH Zurich. They not only built up the whole test setup but also were constantly available providing their professional help and assistance. Without their experience and know how the laboratory work would not have been possible.

Furthermore I would like to thank Amir Salmanpour for his technical help and advises concerning the implementation and evaluation of the optical measuring system (DIC).

Finally, my thanks go to all my family, fellow students and friends for their unremitting support and encouragement.

Contents

List of Figures

List of Tables

1 Introduction

In the past 20 years a lot of research on masonry has been conducted. This has several reasons. On the one hand masonry is still a widely used building material which is economically interesting. On the other hand a lot of buildings being built 40 or 50 years ago are converted or retrofitted today. This leads to the need of a seismic verification that almost none of them can fulfill. That follows from the fact that before 1970 there were no seismic guidelines in the Swiss building codes. (Vogel, 2013) And since 1970 the requirements on seismic verification became more and more severe.

The seismic verification of unreinforced masonry (URM) buildings is quite challenging due to the ambitious behavior of masonry being a composite material with anisotropic behavior. In addition to the ambitious elastic analysis of composite materials masonry also shows some kind of plastic behavior in terms of an admissible plastic ductility capacity that has to be defined to conduct the seismic verification of a building. For practical application there are some computer programs to perform an elastic analysis of masonry walls as for example Murus that is a program part of Cubus. Recently Cubus launched the new program part Promur being able to verify URM buildings. To perform this verification an additional approach for the admissible plastic deformation is established. But still just rectangular walls can be analyzed and verified.

In this master's thesis the influence of flanges attached to rectangular walls is investigated. Furthermore the effects of an applied SLS bearing and the influence of the vertical load magnitude are discussed. Being able to take into account the influence of flanges is important to provide data for more sophisticated models to improve the seismic analysis and performance of URM buildings by where rectangular walls without flanges are rather an exception.

1.1 Seismic Hazard and Risk in Switzerland

Switzerland is classified as a moderate earthquake zone. In 2013 around 600 earthquakes were detected by the Swiss Seismological Service (SED) in Switzerland and its neighboring countries. Twenty-one of them had a magnitude more than 2.5 what is near the average of 23 over the past 38 years. (SED, 2014)

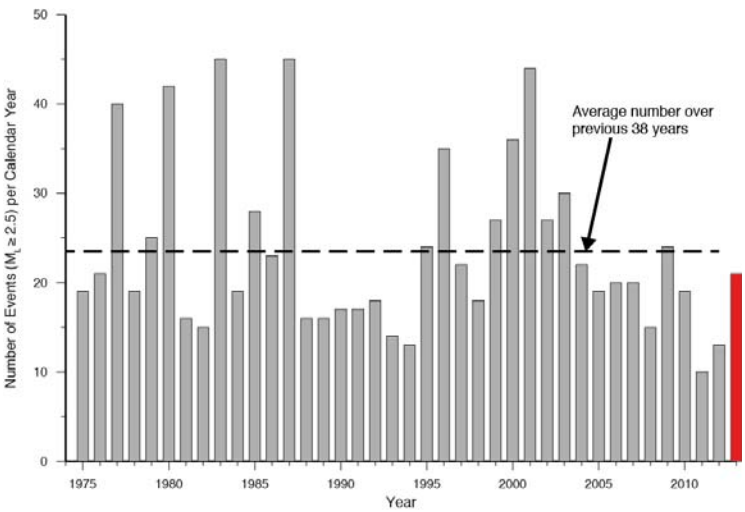

Figure 1.1: Earthquakes Switzerland and neighboring countries (M ≥ 2.5) (SED, 2014)

To account the risk of earthquakes not only the hazard has to be considered but also the impact (damage) has to be taken into account as risk is defined as a combination of both. Figure 1.2 shows the risk caused by earthquakes in Switzerland accounting the seismic hazard, amplification, values and the vulnerability. According to Figure 1.2 although in Switzerland the earthquake activity is moderate, there are many locations where the earthquake risk has to be classified as high (red areas).

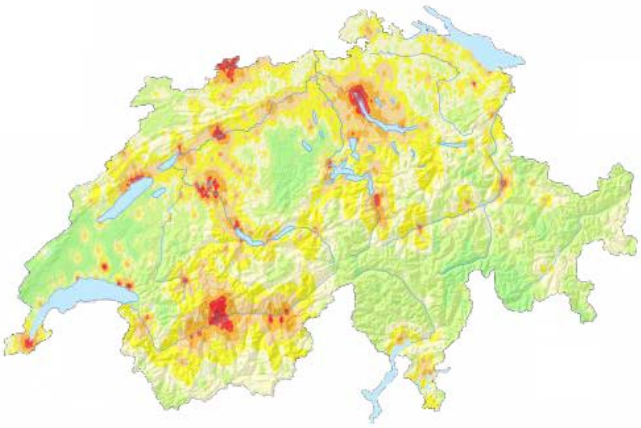

Figure 1.2: Seismic risk Switzerland (SED, 2014)

The high risk of earthquakes in Switzerland is also confirmed by a risk study of the Federal Office for Civil Protection where earthquakes (beside daily incidents as for example car crashes etc.) hold the highest risk of all disasters and emergencies (see *Figure 1.3*). *(Bundesamt für Bevölkerungsschutz, 2003)*

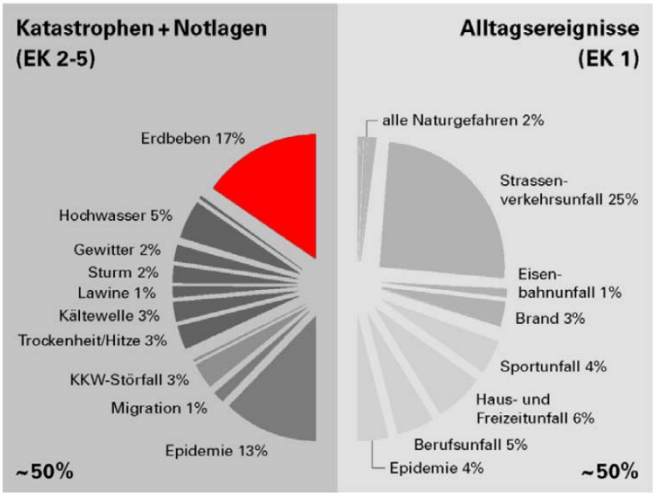

Figure 1.3: Total risks of disasters + emergencies and daily incidents (Bundesamt für Bevölkerungsschutz, 2003)

1.2 URM Buildings and Building Code in Switzerland

A majority of existing residential buildings in Switzerland are built out of URM walls and reinforced concrete slabs. Up to 1970 there were no code guidelines for earthquake resistant buildings. (Vogel, 2013) This does not mean that buildings built before 1970 are not able to resist any lateral forces. For these buildings in the static design for lateral forces the hazard scenario wind got decisive which covers a lot of seismic hazard scenarios. With the release of the new building codes in 1970 mostly reinforced concrete walls were used to provide the earthquake verification. However up to now masonry is a very common building material widely-used due to its advantages in terms of low cost, fast construction progress, high durability and thermal comfort.

Seismic analysis of URM walls gains more and more importance with the need of verifications of existing buildings being converted or retrofitted. But also the seismic verification of new buildings using only URM walls is economically interesting.

1.3 Objectives

Up to now there is only little literature about flanged unreinforced masonry (FURM) walls. In the last 5 to 10 years some theoretical work and experimental research has been done by different authors. The results of Russel (2010) for example show that there is a distinct influence on the behavior of the wall caused by the flanges. In addition to an increase in the shear strength flanges can also lead to an increase in the deformation capacity depending on the failure mode that is observed.

The objectives of this master's thesis include a practical as well as a theoretical part. In the practical part a test series of nine tests on I-shaped URM walls on half scale is provided. The tests are prepared and conducted in the HIF laboratory of the ETH Zurich in collaboration with Jan Egeter who is simultaneously writing his master's thesis about

the effects of flanges discussing additionally the influence of the SLS bearing material and thickness on the behavior of URM walls. Using the same test series as Vögeli (2014) used in his master's thesis about the behavior of rectangular URM walls with SLS bearings provides the possibility of a direct comparison and therefore a convincing statement about the influence of flanges on the behavior of URM walls.

In the theoretical part after a general study of the seismic behavior of rectangular URM walls the effects of flanges are investigated. Furthermore the influence of the vertical load magnitude is discussed. In the run-up to the tests also a theoretical model is developed to predict the failure mode and the maximum shear strength of the tested specimens which at the end are compared to the results of the tests. In addition a brief discussion about the influence of an applied SLS bearing is included in this part.

2 Material Characterization of Masonry

Before proceeding to the behavior of URM walls it seems to be suitable to briefly present masonry as a building material because compared to other building materials masonry is quite demanding to describe as can be seen in the following part.

Masonry is a composite material consisting of bricks and mortar. Failure occurs predominantly along the joints between the bricks and the mortar leading to an anisotropic behavior.

The strength of masonry subjected to in-plane loading is discussed by Mojsilović (2011). The failure criterions by means of stress fields are shown in Figure 2.1.

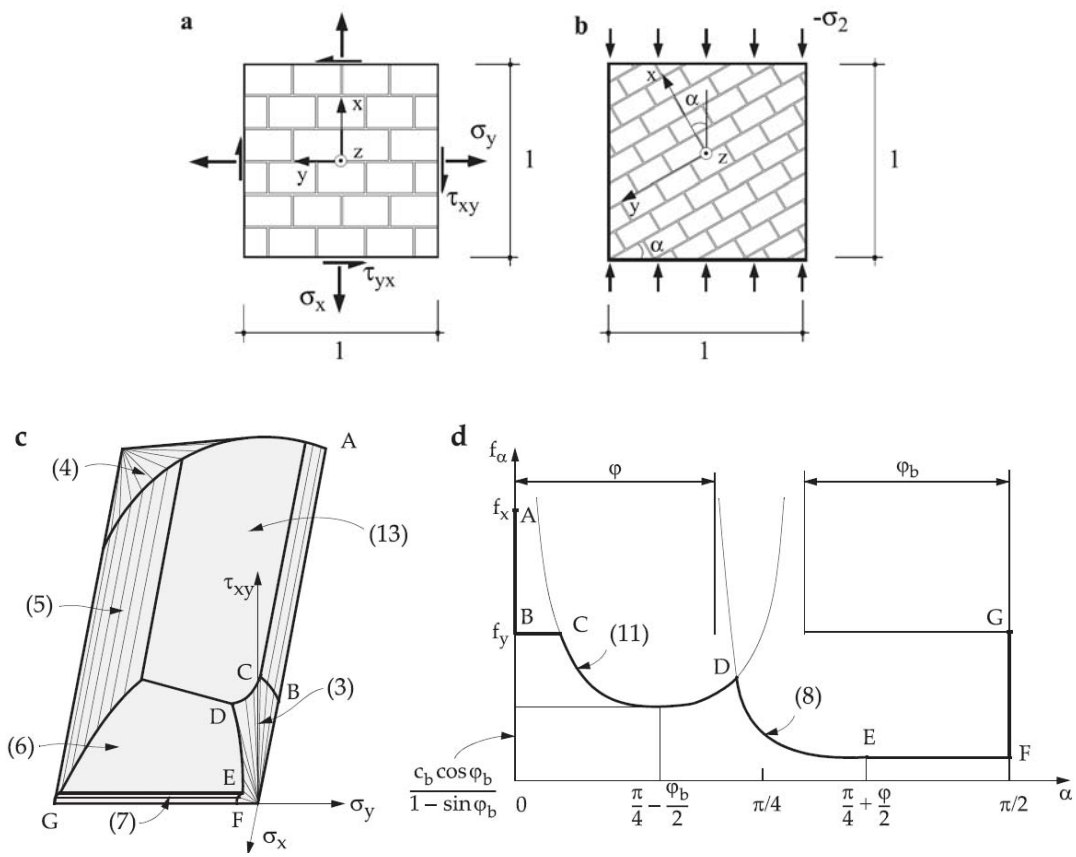

Figure 2.1: (a) notation, (b) uniaxially stressed masonry element, (c) failure surface and (d) uniaxial strength. (Mojsilović, 2011)

The failure surface of Figure 2.1 is built out of a set of six inequalities shown in Figure 2.2 and depends on six material properties, namely the masonry compressive strength perpendicular and parallel to the bed joints, the cohesion (c) and angle of friction (μ) in the bed joints and the cohesion (c_b) and friction (μ_b) of the brick material. The tension strength of masonry is neglected. (Mojsilović, 2011)

$$\tau_{xy}^2 - \sigma_x \sigma_y \leqslant 0$$
$$\tau_{xy}^2 - (\sigma_x + f_x)(\sigma_y + f_y) \leqslant 0$$
$$\tau_{xy}^2 + \sigma_y(\sigma_y + f_y) \leqslant 0$$
$$\tau_{xy}^2 - (c - \sigma_x \tan\varphi)^2 \leqslant 0$$
$$\tau_{xy}^2 + \sigma_x\left[\sigma_x + 2c\tan\left(\frac{\pi}{4} + \frac{\varphi}{2}\right)\right] \leqslant 0$$
$$\tau_{xy}^2 - \left(\frac{c_b}{2} - \sigma_y \tan\varphi_b\right)^2 \leqslant 0$$

Figure 2.2: Set of inequalities describing the failure criterions of masonry. (Mojsilović, 2011)

This sophisticated theoretical model and a distinct sensitivity to the quality of workmanship makes the analysis of masonry very demanding. Therefore experimental tests are essential for reliable design models.

3 Rectangular URM Walls

In the past there has been conducted a lot of research on rectangular URM walls. In the following first the failure modes will be discussed before proceeding to the results of some experimental tests, especially the ones of Vögeli (2014) and Barandun (2013).

3.1 Global Failure Modes

The load transfer in lateral loaded masonry walls can be described using stress fields or some clearly defined uniaxial stress fields (struts). Their failure criterions are illustrated in chapter 2. The collapse of the wall can theoretically be caused by failure of a single strut or a combination of different failure criterions reached in different stress fields at various locations of the wall.

As pointed out in Russell et al. (2014) the number of observed global failure modes of a URM wall varies up to six according to different authors. It can be distinguished between the following failure modes: “Rocking”, “Toe Crushing”, “Sliding” and “Diagonal Tension” whereat the sliding failure can be divided in sliding along a single bed joint or stair-stepped and for diagonal tension failure it can be distinguished between cracks propagating through the mortar joints and cracks propagating through the units. Rocking is regarded as a working condition rather than a failure mode. (Russel, Elwood, & Ingham, 2014) Nevertheless overturning considered as the ultimate level of rocking can cause the wall to fail. In reality due to the common aspect ratios and the boundary conditions given by the slab overturning seems to be a rather unlikely failure mode. Concerning the failure mode diagonal tension the name might be a little bit misleading. Actually it is a shear failure that causes the wall to break. It is the distinct opening of the diagonal crack that leads to the failure named diagonal tension. Since in the literature this type of failure mode is often referred to as “Diagonal Tension” it is called the same in the following chapters. Nevertheless the expression “Shear Failure” can also be found in the literature and is describing the same type of failure. So the four principal failure modes being referred to in the present thesis are namely “Rocking”, “Toe Crushing”, “Sliding” and “Diagonal Tension”. They are visualized for clearance in Figure 3.1.

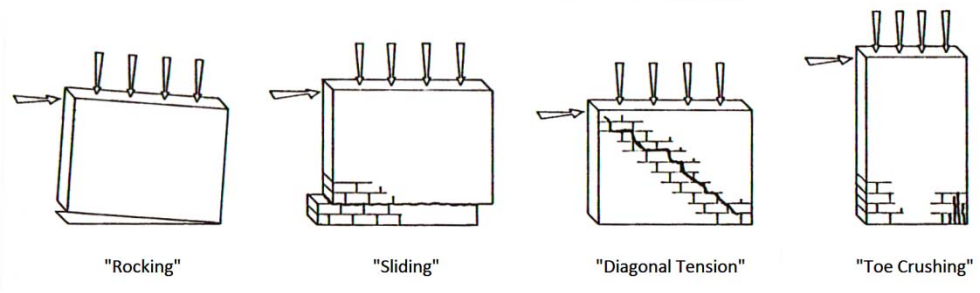

Figure 3.1: Failure modes of URM walls subjected to lateral forces (Tomaževič, 1999)

3.2 Shear Strength

As Tomaževič and Weiss (2012) concluded and what is also obvious and generally accepted from previous research is that the level of precompression is one of the most important governing parameter for the shear strength of an URM wall. However there are different approaches in theory and the country-specific building codes to evaluate the shear strength of an URM wall.

3.2.1 Swiss Code SIA 266

In the Swiss code SIA 266 the shear resistance is verified by the use of design diagrams based on the superposition of stress fields. (SIA D 0237, 2010) The seismic verification of the shear strength for a rectangular URM wall with a centric normal force (in the out-of-plane direction) has to be fulfilled according to equations 3-1 and 3-2.

$$V_d \leq k_v \cdot l_1 \cdot t_w \cdot f_{yd} \qquad \textit{(Eq. 3-1)}$$

$$l_1 = \frac{l_w - 2 \cdot M_{z1d}}{N_{xd}} \qquad \textit{(Eq. 3-2)}$$

The factor k_v has to be determined by means of the design diagrams shown in Figure 3.2 whereat t_{nom} is equal to t_w.

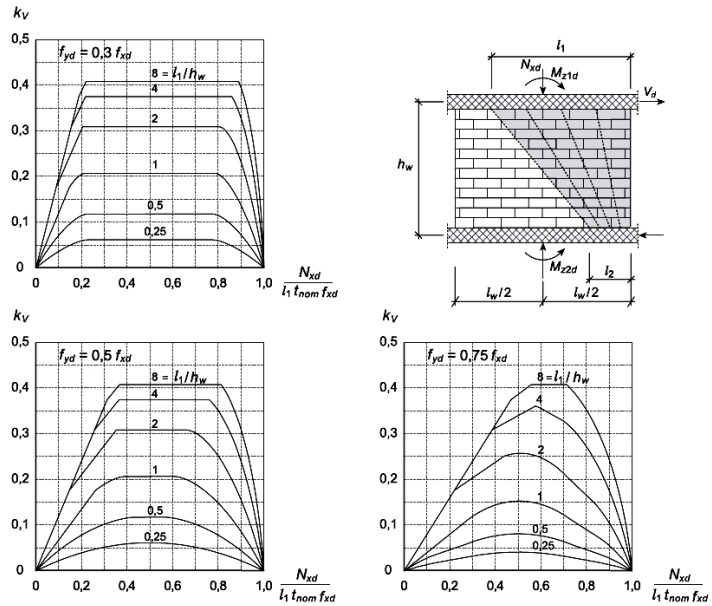

Figure 3.2: Shear resistance according to SIA 266 (SIA 266, 2003)

The design diagrams are based on the following three equilibriums of forces which have to be fulfilled by avoiding compression failure and sliding according to the three following inequalities:

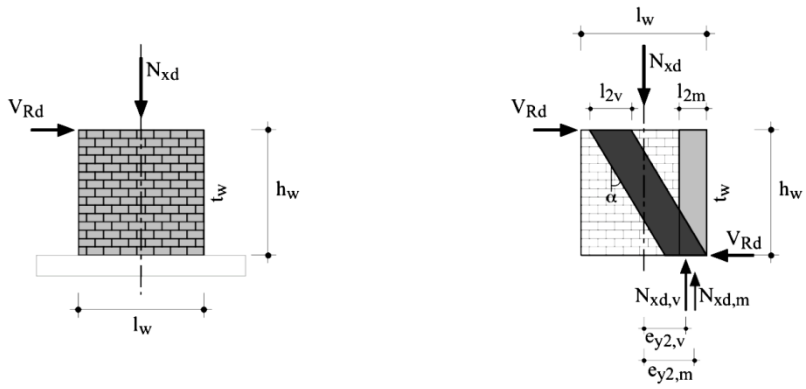

Gleichgewicht :

$$N_{xd,v} + N_{xd,m} = N_{xd}$$

$$N_{xd,v} \cdot e_{y2,v} + N_{xd,m} \cdot e_{y2,m} = M_{z2d} \text{ mit } M_{z2d} = M_{z1d} + V_{Rd} \cdot h_w$$

$$V_{Rd} = N_{xd,v} \cdot tg\alpha$$

Widerstand :

$$N_{xd,v} \leq f_{yd} \cdot l_{2v} \cdot t_w \cdot \cos^2 \alpha$$

$$N_{xd,m} \leq \left(f_{xd} - f_{yd}\right) \cdot l_{2m} \cdot t_w$$

$$tg\alpha \leq \mu_d$$

mit :

$$l_{2v} = l_w - 2 \cdot e_{y2,v}$$

$$l_{2m} = l_w - 2 \cdot e_{y2,m}$$

Figure 3.3: Equilibrium conditions and resistances (SIA D 0237, 2010)

This concept is more suitable for verifications than for evaluation of the shear strength. (SIA D 0237, 2010) And there is no model or recommendations to take into account the effects of flanges. Nevertheless the calculation of the shear strength is possible with an iterative procedure fulfilling the equilibrium conditions and resistances according to Figure 3.3. Using this approach the shear resistance is calculated independent of the failure mode and the normal force is assumed to act centric on the wall.

3.2.2 Effective Pier Model

Yi (2004) developed an effective pier model for the theoretical analysis of rectangular URM walls. This nonlinear macro model allows not only the evaluation of the shear strength but also the calculation of the deformation capacity of rectangular URM walls. The approach for the calculation of the shear strength is briefly discussed in the following. In chapter 4.4 the results of the model will be compared to the observations of the tests of Vögeli (2014) to examine the accuracy of the model which is refined for

flanged URM walls with one flange in chapter 4.2 and later adopted for I-shaped URM walls in chapter 4.3.

The effective pier model has been developed on the following basic assumptions:

- The stress distribution along the effective length of the wall is assumed to be linear.
- The tension strength of the bed-joint is neglected.
- The shear stress is assumed to be uniformly distributed over the effective length of the wall.

The model and its denotation are given in Figure 3.4. (Yi, 2004)

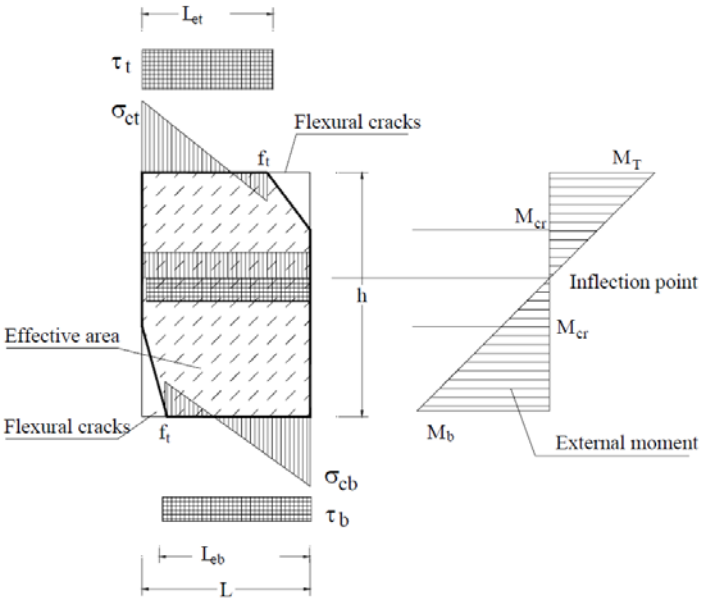

Figure 3.4: Effective pier model (Yi, 2004)

The shear strength according to the failure mode rocking and a cantilever boundary condition is given by equation 3-3 neglecting the tension strength of the bed-joint as mentioned in the basic assumptions.

$$V_r = \left(1 - \frac{2}{3} \cdot \frac{L_b}{L}\right) \cdot 0.5 \cdot (P_t + G) \cdot \frac{L}{h} \qquad \textit{(Eq. 3-3)}$$

Considering the failure mode sliding the cohesion of the bed-joints is conservatively neglected. This takes also an initial rocking behavior into account which destroys the cohesion before sliding occurs. This simplification leads to equation 3-4.

$$V_s = \mu \cdot (P_t + W) \qquad \textit{(Eq. 3-4)}$$

The toe crushing capacity for a cantilever boundary condition is given by equation 3-5.

$$V_{tc} = \frac{1}{2} \cdot (P_f + W) \cdot \left(\frac{L}{h}\right) \cdot \left(1 - \frac{(P_t + W)/(L \cdot t)}{0.75 \cdot \beta \cdot f_m}\right) \qquad \textit{(Eq. 3-5)}$$

The parameter β takes into account the error in the assumption of a linear stress distribution along the effective length of the wall. Yi (2004) recommends to set β equal to a value of 1.28.

The diagonal tension capacity is calculated considering a finite element in the middle of the wall. The element is loaded with a vertical normal stress given by the precompression and a shear stress given by the horizontal force acting on top of the wall. There is no lateral confining stress taken into account. Yi (2004) recommends taking into account such a lateral confinement for aspect ratios L/h > 1 and assumes no lateral confining stress for aspect ratios L/h < 0.5.

The specimens of Vögeli (2014) exhibit an aspect ratio of 1 leading to the conclusion that there is reasonably no confining stress present. Failure occurs when according to Mohr's Circle the principal tension stress reaches the diagonal tension strength of masonry leading to equation 3-6.

$$V_{dt} = \frac{1}{\zeta} \cdot (L \cdot t \cdot f_{dt}) \cdot \sqrt{1 + \frac{P_b}{L \cdot t \cdot f_{dt}}} \qquad \textit{(Eq. 3-6)}$$

The parameter ζ depends on the assumed shear stress distribution. While for slender walls (L/h > 0.5) a parabolic distribution is assumed and ζ is equal to 1.5, the distribution for stout walls (L/h > 2) is supposed to be constant leading to a ζ equal to 1.0. (Yi, 2004)

Gaining the value of the diagonal tension strength of masonry is quite challenging and therefore only few suggestions can be found in literature. One suggestion is given by Lee et al. (2008) who defines the diagonal tension strength of masonry in relation to the masonry compressive strength as shown in equation 3-7.

$$f_{dt} = 0.05 \cdot f_m \qquad \textit{(Eq. 3-7)}$$

Another suggestion in relation to the masonry compressive strength is given by Ali et al. (2012) in equation 3-8. They gained their formula directly based on experimental data.

$$f_m = 4.57 \cdot f_{dt}^{0.30} \qquad \textit{(Eq. 3-8)}$$

This two approaches indicate that there is a lot of uncertainty in the evaluation of this value leading to a wide spread of results.

3.3 Energy Dissipation

Energy dissipation is caused by damping. In real structures there are various damping sources like structural damping caused by internal friction of the material or coulomb damping caused by the friction of dry surfaces. In most cases all sources of damping are embraced and modeled as viscous damping in a way that the dissipated energy is equal. The corresponding coefficient is therefore called equivalent viscous damping ratio and defined by equation 3-9. Being strictly the equivalent viscous damping ratio (in the

following referred to as damping ratio) depends on the exciting frequency and should be calculated at $\omega=\omega_n$ where the system is most sensitive to damping. But the approximation with different exciting frequencies is accurate over a wide range of frequencies. (Chopra, 2012)

$$\xi = \frac{1}{4\cdot\pi} \cdot \frac{E_D}{E_{So}} \qquad \textit{(Eq. 3-9)}$$

The dissipated Energy (E_D) is represented by the area enclosed by a complete hysteresis loop. The strain energy (E_{So}) is defined as the area under the liner connection between the origin of ordinates and the point of maximum displacement.

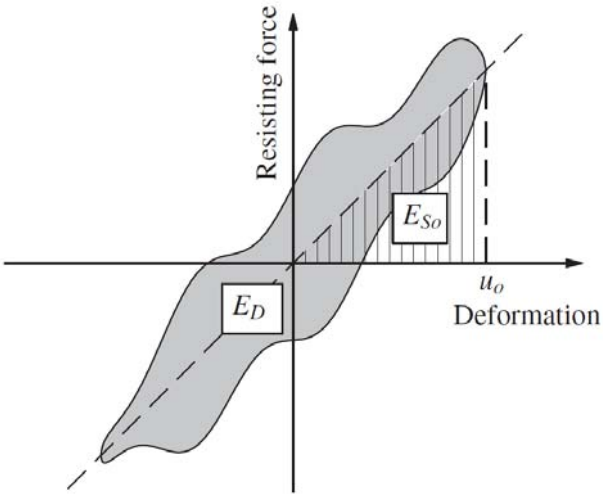

Figure 3.5: Equivalent viscous damping ratio (Chopra, 2012)

Viscous damping is present when a solid body is moving through liquid and it is directly proportional to the velocity. The reason why all sources of damping in structures are modeled with viscous damping is that this form of damping is the simplest and leading to a linear differential equation of motion (Chopra, 2012).

Knowing that most of the damping measured in our experiments of chapter 6 is caused by friction the equivalent viscous damping ratio may not be the best solution to compare the energy dissipation capacity. Because the force-deformation curves show a distinct plateau in case of rocking and sliding the relation to the strain energy is probably not the best approach. It may be more convenient to relate the dissipated energy to the whole input energy as the dissipated energy ratio does as shown in equation 3-10.

$$\zeta = \frac{E_{diss}}{E_{inp}} \qquad \textit{(Eq. 3-10)}$$

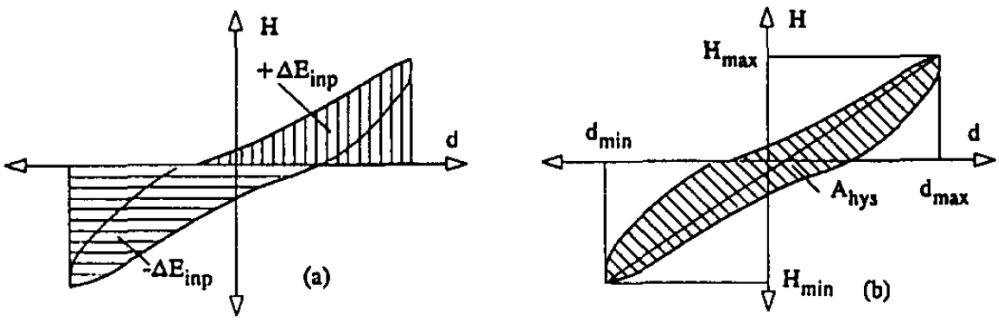

Figure 3.6: Dissipated energy ratio (Tomaževič, Lutman, & Petković, 1996)

The dissipated energy (E_{diss}) is defined as the area enclosed by a complete hysteresis loop. The input energy (E_{inp}) is defined as the area under the force-deformation loading curve till the maximum displacement is reached.

3.4 Experimental Tests of Vögeli (2014)

In the following the experimental tests of Vögeli (2014) are discussed in detail. The fact that he tested exactly the same wall specimens as being tested in chapter 6 except of the flanges provides a possibility for a direct comparison between the results and therefore allows to draw meaningful conclusions about the effects of flanges.

The test series of Vögeli (2014) is shown in Table 3.1.

Specimen	Applied axial force [kN]	Weight of beams [kN]	Total pre-compression [MPa]	Percentage of strength [%]
W0.10	101.5	6.4	0.62	13.2
WE3.10	102.5	6.4	0.62	13.2
WE10.10	102.4	6.4	0.62	13.2
WG3.5	52.5	6.4	0.33	7.0
WG3.10	103.5	6.4	0.62	13.2
WG3.15	157.5	6.4	0.93	19.8
WG10.5	51.4	6.4	0.33	7.0
WG10.10	102.6	6.4	0.62	13.2
WG10.15	155.9	6.4	0.93	19.8

Table 3.1: Test series (Vögeli, 2014)

All the tests were conducted in the HIF laboratory of the ETH Zurich. The test setup is shown in Figure 3.7.

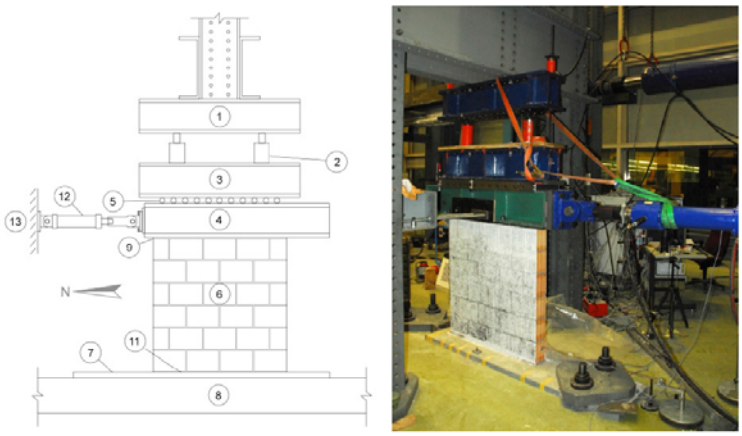

Figure 3.7: Test setup rectangular URM walls (Vögeli, 2014)

For his tests Vögeli (2014) used the cantilever boundary condition consisting of a fixed end at the bottom and free end at the top of the wall. The forces in the two jacks applying the vertical pressure were kept constant during the test so that no moment was induced on the top of the wall. The displacement pattern was the same used for the present tests of chapter 6 that is shown in Figure 6.12.

3.4.1 Shear Strength and Maximum Displacement

The maximum shear strength observed during the tests and the corresponding failure modes are listed in Table 3.2. When the failure mode could not be clearly defined more than one is listed mentioning the dominating one first.

Specimen	Name	Shear strength V_{max} [kN]	Failure mode	Ultimate displacement d_u [mm]	Ductility μ [-]
1	WE3.10	48.6	Toe Crushing	29.5	15.7
2	WE10.10	43.1	Toe Crushing / Diagonal Sliding	14.4	6.3
3	WG3.5	33.2	Toe Crushing / Horizontal Sliding	50.9	38.4
4	WG3.10	50.8	Toe Crushing / Diagonal Sliding	19.7	6.6
5	WG3.15	74.6	Diagonal Tension	14.6	5.0
6	WG10.5	36.5	Toe Crushing / Horizontal Sliding	42.7	5.0
7	WG10.10	46.8	Toe Crushing	26.4	4.1
8	WG10.15	60.5	Diagonal Tension	19.1	3.1
9	W0.10	52.5	Diagonal Sliding / Toe Crushing	15.0	8.3

Table 3.2: Test results rectangular URM walls (Vögeli, 2014)

All specimens showed an initial rocking behavior before failing according to the mentioned failure modes in Table 3.2.

High displacements are principally observed for low precompression and thin SLS bearings.

3.4.2 Influence of Precompression

The level of precompression has an essential influence on the behavior of URM walls under lateral load. Up to a certain level, which for most masonry material is around 30% of the masonry compressive strength, the influence of vertical compression is favorable meaning that a higher level of precompression leads to a higher lateral resistance. This effect is also visible in the results shown in Figure 3.8. (Vögeli, 2014)

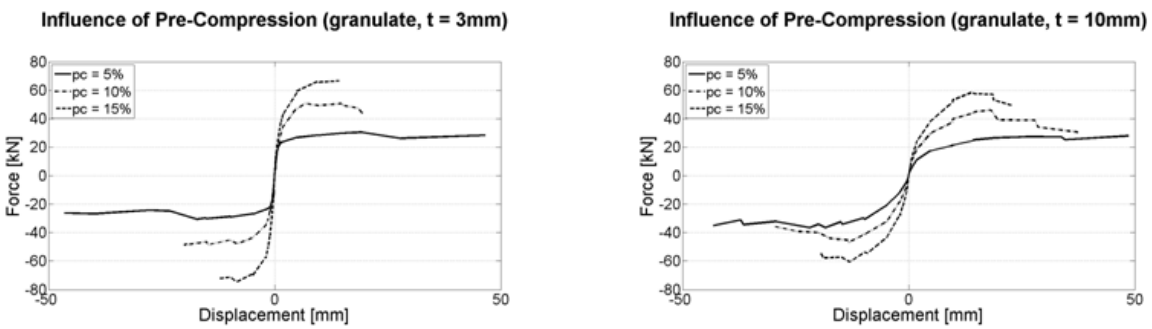

Figure 3.8: Influence of precompression (Vögeli, 2014)

Furthermore a higher precompression leads to a stiffer and less ductile behavior. The amount of stiffness reduction depends clearly on the thickness of the SLS layer. (Vögeli, 2014)

3.4.3 Influence of Layer

In general it can be said that the deformation capacity is clearly higher with the presence of a SLS bearing. For thick layers (10 mm) the granulate SLS bearing provides a clearly higher deformation capacity than the one out of extruded elastomer which is mainly caused by sliding. For thin layers (3 mm) this effect is not clearly present as can be seen in Figure 3.9. (Vögeli, 2014)

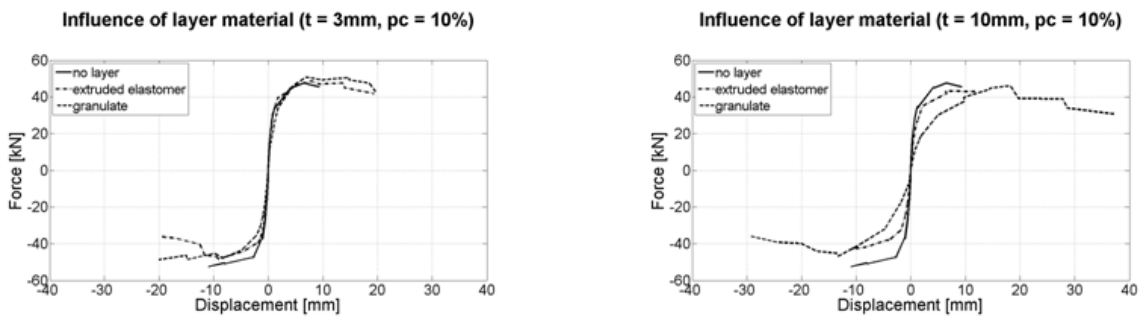

Figure 3.9: Influence of layer material (Vögeli, 2014)

Having a closer look at the layer thickness for extruded elastomer it can be concluded that an increasing layer thickness leads to a small reduction of shear strength. Concerning the deformation capacity no clear trend can be observed for a change in elastomer layer thickness (see Figure 3.10). Looking at the granulate SLS bearings in Figure 3.10 a distinct rise in the deformation capacity can be recognized when the layer thickness is increased. However, no clear trend regarding the shear strength can be concluded for granulate SLS bearings. (Vögeli, 2014)

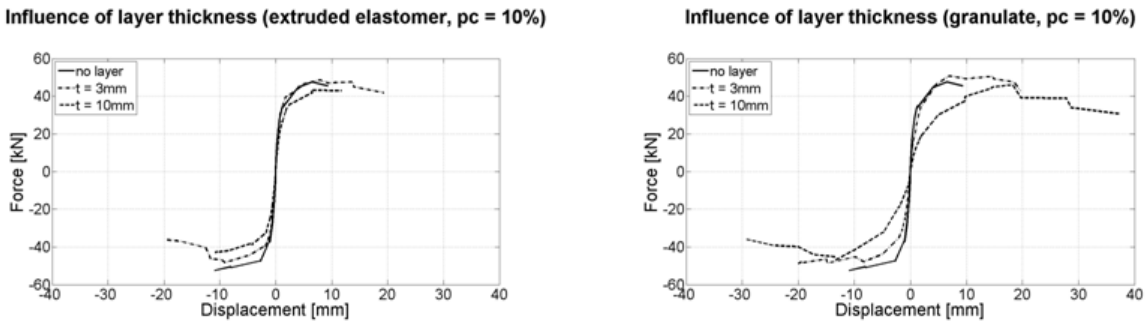

Figure 3.10: Influence of layer thickness (Vögeli, 2014)

3.4.4 Energy Dissipation

Having a look at the results of the specimens with elastomer SLS bearings and a precompression of 0.33 MPa it can be seen that the energy dissipation is very similar for a layer thickness of 3 mm as well as for one of 10 mm. Both exhibit an initial almost linear rise in the first small cycles of the damping ratio till a value of approximately 20% is reached at a displacement of 5 mm. This value keeps more or less constant until the point of failure where another rise in energy dissipation can be observed. (Vögeli, 2014)

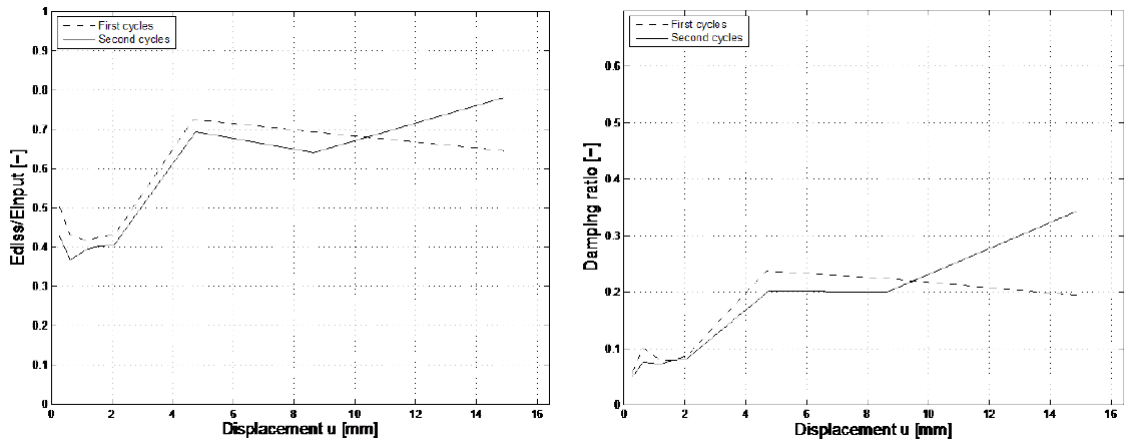

Figure 3.11: WE10.10, (l) Dissipated energy ratio, (r) Damping ratio (Vögeli, 2014)

These results do not differ much from the values achieved for the specimen without a SLS bearing which are shown in Figure 3.12.

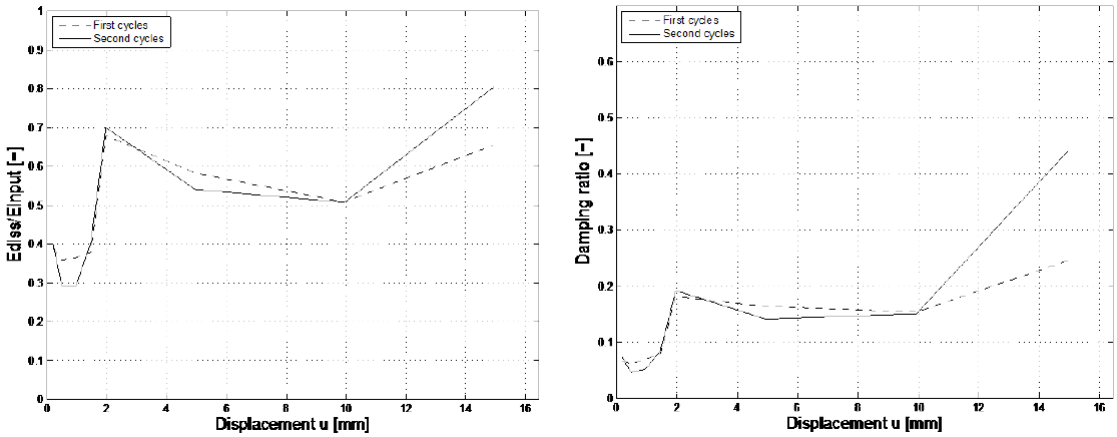

Figure 3.12: W0.10, (l) Dissipated energy ratio, (r) Damping ratio (Vögeli, 2014)

Concerning the granulate SLS bearings with a precompression of 0.33 MPa it can be seen in Figure 3.13 that the dissipated energy ratio exhibits a value between 50 and 70% and the damping ratio achieves a plateau of about 20% but after a distinct longer period of rise than the specimen with elastomer SLS or no bearings. (Vögeli, 2014)

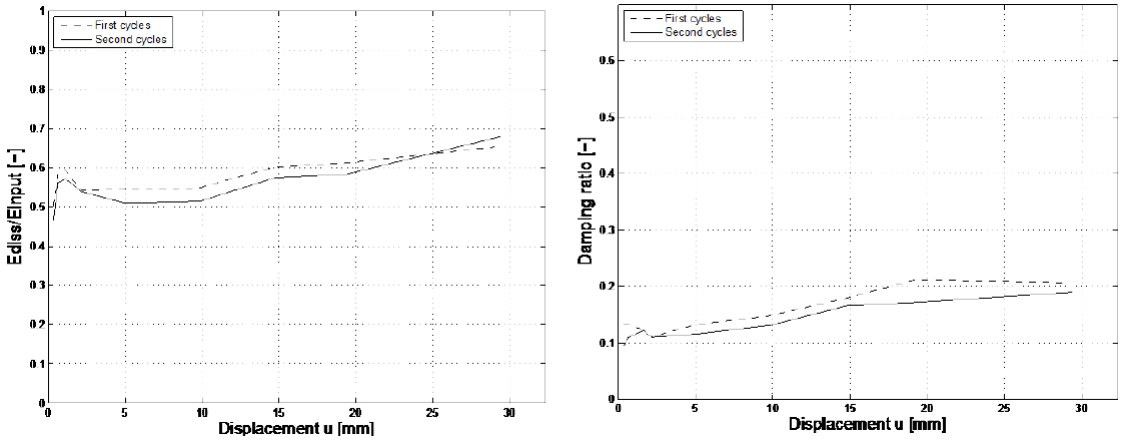

Figure 3.13: WG10.10, (l) Dissipated energy ratio, (r) Damping ratio (Vögeli, 2014)

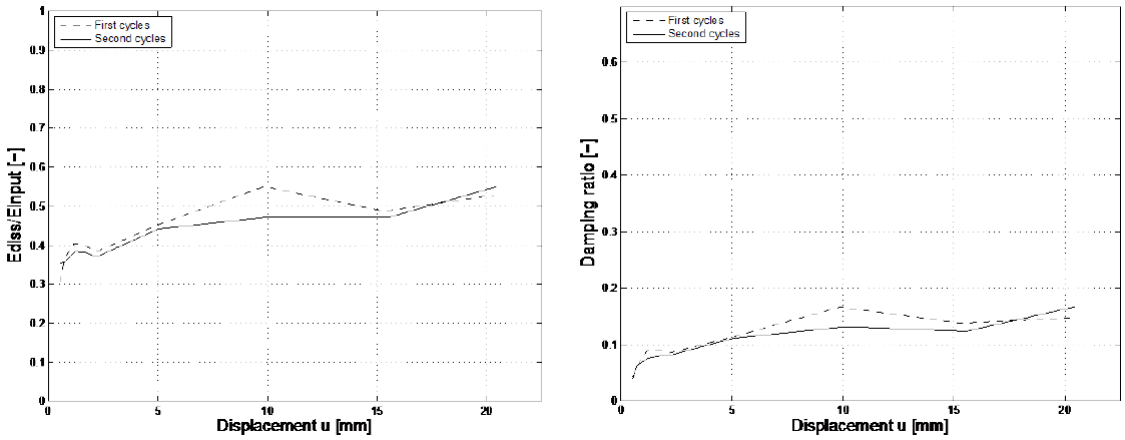

Figure 3.14: WG3.10, (l) Dissipated energy ratio, (r) Damping ratio (Vögeli, 2014)

Changing the precompression has no nameable influence on the energy dissipation as long as no sliding failure occurs. For a sliding failure a distinct higher energy dissipation is observed. (Vögeli, 2014)

3.4.5 Damage SLS Bearing

While for elastomer SLS bearings generally almost no damage is observed independent of the failure mode for granulate SLS bearings the failure mode is decisive for the amount of damage. In general more damage was observed for the granulate soft-layer due to the weaker material composition. Depending on the failure mode for granulate soft-layers distinct more damage was observed due to sliding than due to other failure modes.

Particular photographs are presented later when the experimental results of chapter 6.9 are compared to the observations of Vögeli (2014).

3.5 Experimental Tests of Barandun (2013)

Barandun (2013) tested wall specimens in his master's thesis with the same geometry as the ones Vögeli (2014) tested. The difference is that Barandun placed the SLS bearings in the first bed-joint and not in the interface between the concrete plate and the wall. All his tests were conducted under a precompression of 10% of the masonry compressive strength. He used the same test setup as Vögeli (2014) shown in Figure 3.7 with cantilever boundary condition. The same loading pattern was used for the tests as the one in chapter 6 that is visualized in Figure 6.12.

From all the tests he conducted shown in Table 3.3, only the ones with a 3 or 10 mm SLS layer (marked with a gray background) can theoretically be used for the comparison with the I-shaped URM walls in the present master's thesis.

Label	Material	Layer Thickness	Joint Thickness [mm]
W0	-	-	10
W0R	-	-	10
WG3	Rubber	3	10
WG5	Rubber	5	10
WG10	Rubber	10	15
WE3	Extruded	3	10
WE5	Extruded	5	10
WE10	Extruded	10	15
WE3R	Extruded	3	10
WE5R	Extruded	5	10

Table 3.3: Test series (Barandun, 2013)

3.5.1 Shear Strength

The shear resistances Barandun (2013) observed in his tests are shown in Table 3.4. He did not allocate specific failure modes to the tested specimens. So the decisive failure

mode given in Table 3.4 is defined by means of his crack description and the limited photographs published in his master's thesis.

Specimen	Shear strength V_{max} [kN]	Failure mode
WE3R	41.1	"Toe crushing" / "Sliding diagonal"
WE10	46.3	"Toe crushing" / "Sliding diagonal"
WG3	46.5	"Sliding horizontal"
WG10	49.3	"Sliding horizontal"
W0R	55.4	"Toe crushing"

Table 3.4: Shear strength and decisive failure modes (Barandun, 2013)

Since Barandun (2013) used a different position of the SLS bearings and did not change the level of precompression it will only be directly referred to the test results of Vögeli (2014) in the scope of this master's thesis. Nevertheless Barandun (2013) made an interesting observation concerning the energy dissipation shown in chapter 3.5.2.

3.5.2 Energy Dissipation

According to the data of Barandun (2013) the thickness of the elastomer SLS bearing has no significant influence on the damping ratio.

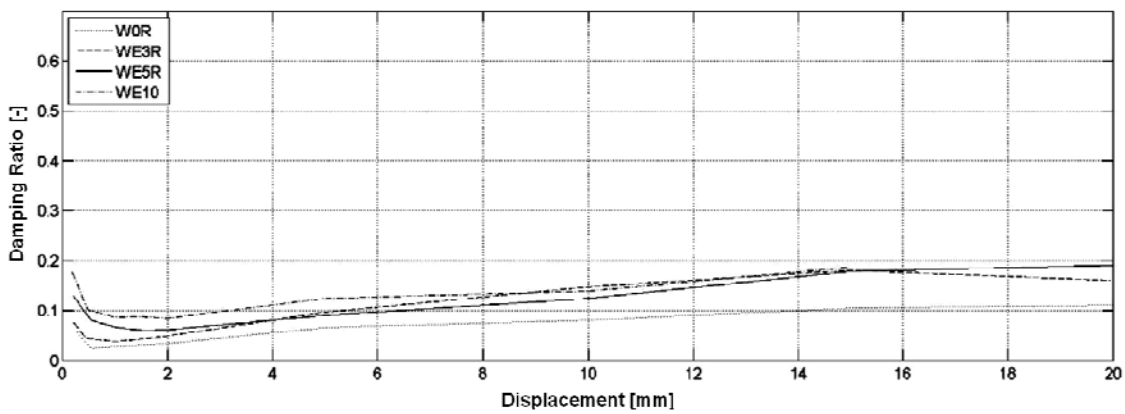

Figure 3.15: Damping ratio of first cycles WE-series (Barandun, 2013)

Having a look at the granulate SLS bearings the situation is completely different. The layer thickness has a distinct influence on the energy dissipation and as can be seen in Figure 3.16 the specimens with the thin granulate SLS bearings exhibit distinct higher damping ratios if the target displacement gets larger. Comparing the specimen WG3 with WG10 the higher damping ratio of the thin layer may be due to the fact that the thin layer is destroyed very fast and as soon as the layer is destroyed there is friction between mortar and bricks (both specimen failed due to horizontal sliding) which dissipates more energy than the friction with a soft layer in between reducing the friction coefficient. The faster deterioration of the thin soft-layer is shown in chapter 3.5.3.

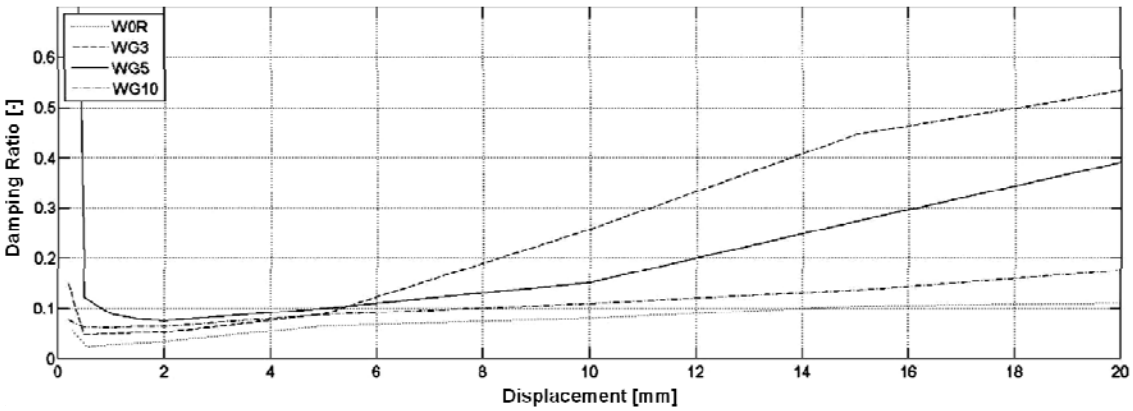

Figure 3.16: Damping ratio of first cycles WG-series (Barandun, 2013)

More about the influence of the soft-layer thickness can be read in Egeter (2014).

3.5.3 Damage SLS Bearing

The SLS bearings applied in the first bed-joint suffered much more damage than the ones applied in the interface between the concrete basement and the first mortar joint as can be seen in Figure 3.17. This is mainly caused by the rough surface of the bricks with all the holes in it. It seems therefore suitable to place the soft-layer in the interface joint.

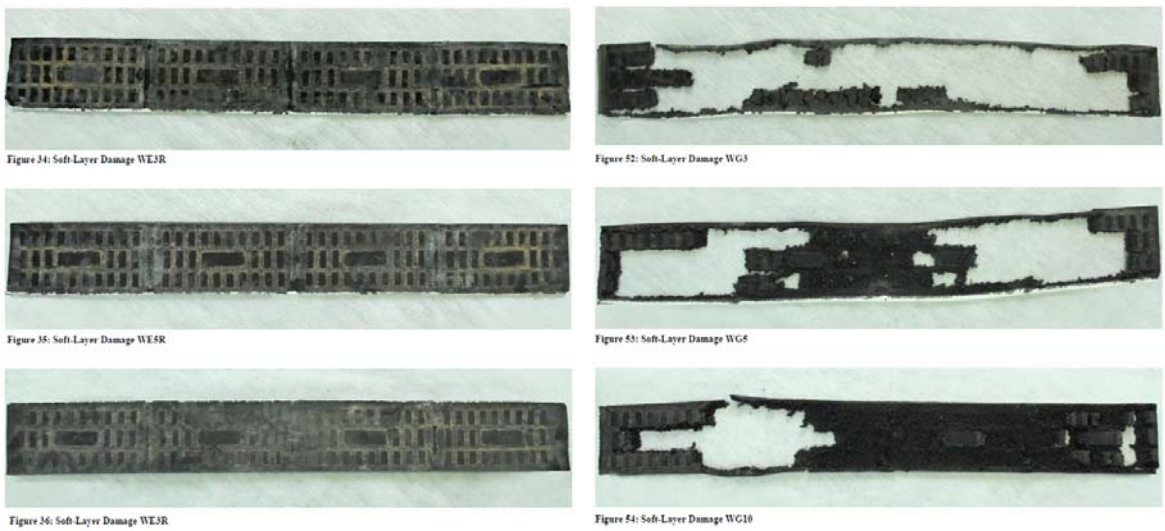

Figure 3.17: Damage SLS bearings (Barandun, 2013)

4 I-Shaped URM Walls

Concerning flanged URM walls and in particular I-shaped URM walls far less data is available and only few experimental tests were conducted. Regarding typical floor plans of residential buildings it is apparent that a single rectangular wall in most cases represents an exception. Most walls are connected to at least one perpendicular wall forming an L-, U- or I-shaped construction. Therefore the detailed analysis of the behavior of URM buildings demands a propagation of the experimental and theoretical knowledge about rectangular URM walls to FURM walls. In the following chapter the modified effective pier model of Yi (2004) that is based on the effective pier model presented in chapter 4.2 is introduced. This model allows taking into account a single flange perpendicular to the web of the wall. This modified effective pier model is adapted to I-shaped URM walls in chapter 4.3.

4.1 Shear Strength

As known from other materials as for example steel or reinforced concrete the shear strength of I-shaped walls is intuitively assumed to be higher than for rectangular walls. But as already mentioned in chapter 2 the material behavior of masonry is more complicated. Nevertheless according to a few single observations for example in Russel (2010) this assumption is also justified for I-shaped URM walls. To give the theoretical foundation for this assumption in this chapter each failure mode discussed in the modified effective pier model of Yi (2004) is adapted to an I-shaped geometry.

4.2 Modified Effective Pier Model

The effective pier model mentioned in chapter 3.2.2 was extended in Yi (2004) allowing the use for FURM walls. This modified effective pier model takes into account the effects of one perpendicular wall (flange) connected to the in-plane pier (see Figure 4.1).

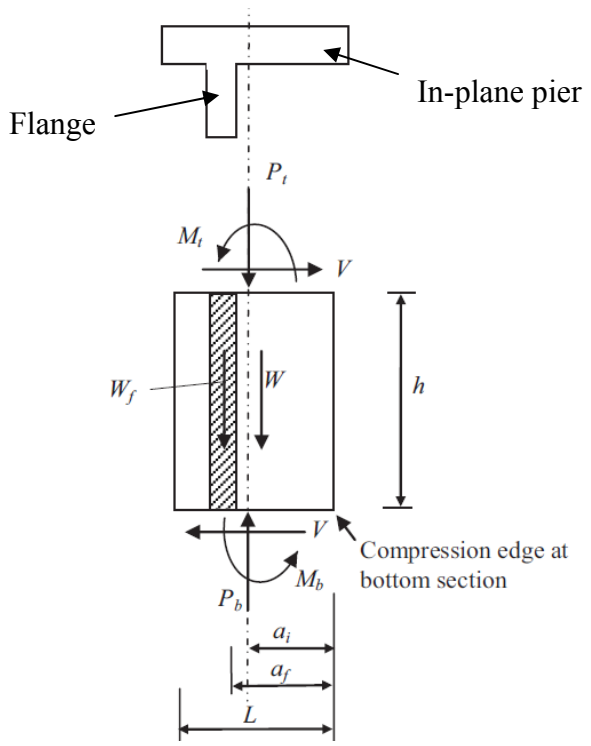

Figure 4.1: Modified effective pier model (Yi, Moon, Leon, & Kahn, 2008)

Since this model does only provide the basis for the equations presented in chapter 4.3 for I-shaped URM walls and is not used any more in this thesis the detailed formulas to calculate the shear resistance according to the different failure modes are not presented at this point. Furthermore there is a direct comparison of the formulas of the modified effective pier model and the equivalent adaptation of I-shaped walls in appendix E.

4.3 Adaptation to I-Shaped URM Walls

As mentioned the modified effective pier model was developed for a variable location of one flange along the in-plane pier. Therefore the model has to be adapted for the investigation of the I-shaped URM walls being tested in chapter 6. Based on the concept and findings of Yi (2004) and his presentation of the modified effective pier model the following equations of shear strength where developed by the author ending up in an I-shaped modified effective pier model.

Some of the basic assumptions of Yi et al. (2008) where adopted. For clarity and comprehension the basic assumptions of Yi et al. (2008) are repeated next:

1. The axial stress distribution along the bed joint (σ_v) is supposed to be linear.
2. The force is assumed to act centrically on the wall and possible torsion is neglected. For I-shaped walls this assumption is expected to be true.
3. It is known that there is a limit of the length of the flange that is participating on the lateral force resistance. This effective flange length can be determined for example by the projected crack pattern on the flange according to Yi (2004).

The assumptions are modified and extended in the following way:

- In the model the whole flange is supposed to be fully participating on the lateral force resistance. With respect to the 45°-rule presented in Yi (2004) and the used geometry of the tested specimens in chapter 6 this assumption seems reasonable.
- The connection of the flanges to the web is assumed to be proper and intact until the failure mode appears.
- Furthermore the vertical stress distribution in the flange is assumed to be constant over the length of the flange as well as the width of the flange. The level of vertical stress in the flange is taken as the level resulting in the pier in the middle of the width of the flange.

Opposite to the modified effective pier model of Yi (2004) the adapted modified effective pier model consists of an in-plane pier with two flanges at fixed locations at the ends of the in-plane pier (see Figure 4.2). To evaluate the shear strength of an I-shaped URM wall the four global failure modes presented in chapter 3.1 are analyzed and the one with the smallest resistance is expected to be decisive for the failure of the wall.

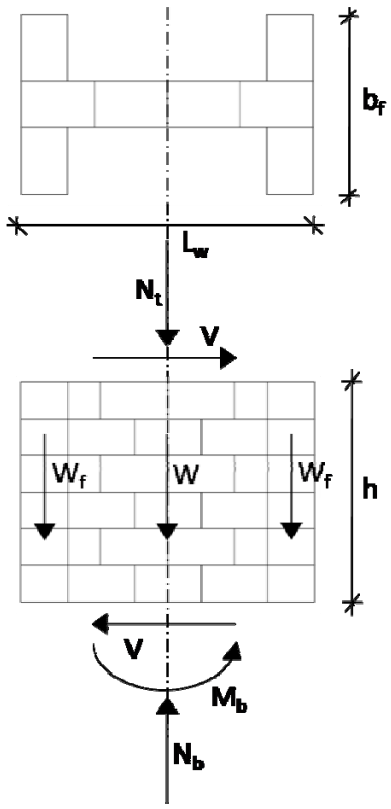

Figure 4.2: Adapted modified effective pier model for I-shaped URM walls

4.3.1 Rocking

To evaluate the shear resistance of the failure mode rocking two limit states are examined. The first limit state is defined by the moment when the heel of the walls is

lifting up. At this state the stress at the heel of the wall is equal to zero as can be seen in Figure 4.3. The equilibrium of forces and moments is given by equations 4-1 and 4-2:

$$P_b = P_t + W + 2 \cdot W_f \qquad \textit{(Eq. 4-1)}$$

$$M_b = V \cdot h \qquad \textit{(Eq. 4-2)}$$

Taking into account the two flanges at both ends of the in-plane pier the equilibrium based on the linear stress distribution in the bed-joint is given by equations 4-3 and 4-4:

$$P_b = \frac{1}{2} \cdot \sigma_{v,max} \cdot L_w \cdot t + A_f \cdot \sigma_{v,max} \qquad \textit{(Eq. 4-3)}$$

$$M_b = \frac{1}{12} \cdot L_w^2 \cdot \sigma_{v,max} \cdot t + A_f \cdot \left(\sigma_{v,max} - \frac{\sigma_{v,max}}{L_w} \cdot t_f\right) \cdot \left(\frac{L_w}{2} \cdot \frac{t_f}{2}\right) \qquad \textit{(Eq. 4-4)}$$

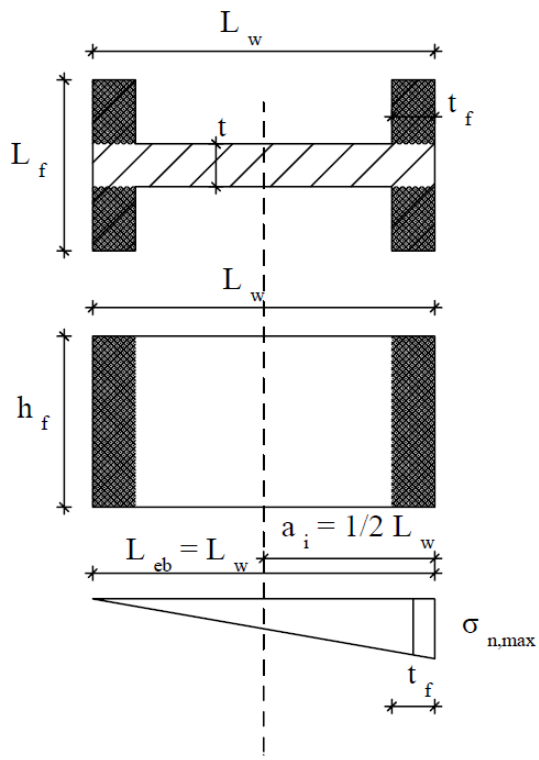

Figure 4.3: Vertical stress distribution at start of rocking

The maximum vertical stress ($\sigma_{v,max}$) can be calculated using equations 4-1 and 4-3. By combining equations 4-2 and 4-4 it can be solved for the shear resistance (V_r). And inserting $\sigma_{v,max}$, calculated before, leads to the following shear resistance limit for uplift:

$$V_r = \frac{P_b \cdot \left[L_w^3 \cdot t + 6 \cdot A_f \cdot (t_f - L_w)^2\right]}{6 \cdot h \cdot L_w \cdot (L_w \cdot t + 2 \cdot A_f)} \qquad \textit{(Eq. 4-5)}$$

Overturning occurs when the elongation of the resulting force acting on the specimen does no longer puncture the contour area of the footprint. To get the according shear

resistance a simple moment equilibrium can be done at the center of rotation represented by the toe of the wall leading to the following maximum shear resistance:

$$V_{ro} = \frac{L_w}{h} \cdot \left(\frac{W+P_t}{2} + W_f\right) \qquad \textit{(Eq. 4-6)}$$

4.3.2 Toe Crushing

For simplicity the masonry tension strength rectangular to the bed-joint is neglected. The vertical stress distribution at the bottom of the wall is assumed to be linear and the limit level of toe crushing is reached when the maximum vertical stress is equal to the masonry compressive strength (f_m).

$$\sigma_{v,max} = \beta \cdot f_m \qquad \textit{(Eq. 4-7)}$$

The factor beta is accounting for the nonlinear distribution of the vertical stress along the bed-joint. This factor is set to 1.3 according to Yi et al. (2005). (Yi T. , Moon, Leon, & Kahn, 2005)

Under the mentioned conditions above two cases for the vertical stress distribution at the bottom need to be investigated depending on the value of the effective length (L_{eb}) according to Figure 4.4.

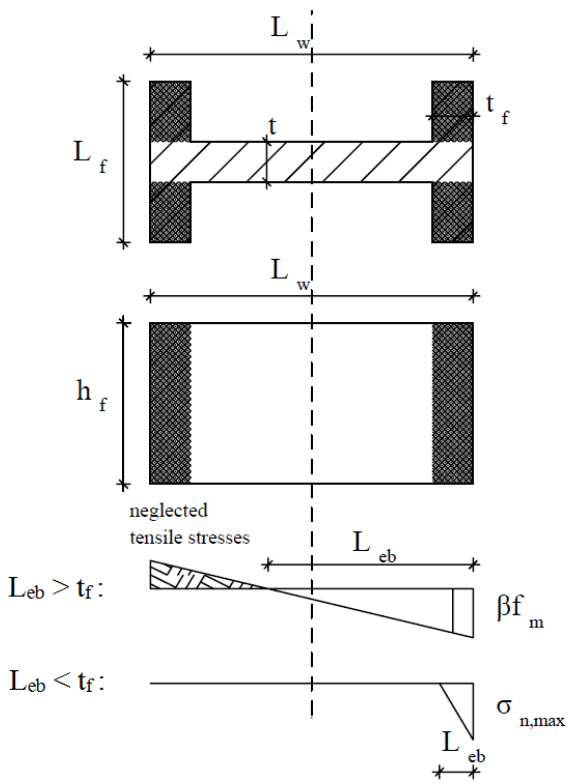

Figure 4.4: Vertical stress distribution toe crushing

For toe crushing equations 4-1 and 4-2 are still valid while equations 4-3 and 4-4 change to:

$$P_b = \frac{1}{2} \cdot \sigma_{v,max} \cdot L_{eb} \cdot t + A_f \cdot \left(\sigma_{v,max} - \frac{\sigma_{v,max}}{L_{eb}} \cdot \frac{t_f}{2}\right) \quad \textit{(Eq. 4-8)}$$

$$M_b = \frac{1}{2} \cdot \sigma_{v,max} \cdot L_{eb} \cdot t \cdot \left(\frac{L_w}{2} - \frac{L_{eb}}{2}\right) + \frac{1}{12} \cdot L_{eb}^2 \cdot \sigma_{v,max} \cdot t + A_f \cdot \left(\sigma_{v,max} - \frac{\sigma_{v,max}}{L_{eb}} \cdot \frac{t_f}{2}\right) \cdot \left(\frac{L_w}{2} - \frac{t_f}{2}\right) \quad \textit{(Eq. 4-9)}$$

The effective length (L_{eb}) at the bottom, which is the length that is under compressive stress only, can be found using equations 4-7 and 4-8:

$$L_{eb} = \frac{\sqrt{A_f \cdot f_m^2 \cdot \beta^2 \cdot (t_f \cdot t + A_f) - 2 \cdot A_f \cdot f_m \cdot P_b \cdot \beta + P_b^2} + (P_b - A_f \cdot f_m \cdot \beta)}{f_m \cdot \beta \cdot t} \quad \textit{(Eq. 4-10)}$$

These three equations above in combination with equations 4-1 and 4-2 lead to a shear resistance of:

$$V_{tc} = \frac{P_b \cdot [L_{eb}^2 \cdot (3 \cdot L_w - 2 \cdot L_{eb}) \cdot t + 3 \cdot A_f \cdot (2 \cdot L_{eb} - t_f) \cdot (L_w - t_f)]}{6 \cdot h \cdot [L_{eb}^2 \cdot t + A_f \cdot (2 \cdot L_{eb} - t_f)]} \quad \textit{(Eq. 4-11)}$$

If the effective length (L_{eb}) at the bottom is shorter than the width of the flange at the toe of the wall equations 4-8 and 4-9 have to be modified in the following way:

$$P_b = \frac{1}{2} \cdot \sigma_{v,max} \cdot L_{eb} \cdot t + L_{eb} \cdot (L_f - t) \cdot \frac{\sigma_{v,max}}{2} \quad \textit{(Eq. 4-12)}$$

$$M_b = \frac{1}{2} \cdot \sigma_{v,max} \cdot L_{eb} \cdot t \cdot \left(\frac{L_w}{2} - \frac{L_{eb}}{2}\right) + \frac{1}{12} \cdot L_{eb}^2 \cdot \sigma_{v,max} \cdot t + L_{eb} \cdot (L_f - t) \cdot \frac{\sigma_{v,max}}{2} \cdot \left(\frac{L_w}{2} - \frac{L_{eb}}{3}\right) \quad \textit{(Eq. 4-13)}$$

In this case a more accurate model for the stress distribution in the flange is used. The stress distribution along the length of the flange is still kept constant while a linear distribution according to the pier is assumed along the width of the flange. This leads to a new effective length and a new shear resistance:

$$L_{eb} = \frac{2 \cdot P_b}{\beta \cdot f_m \cdot L_f} \quad \textit{(Eq. 4-14)}$$

$$V_{tc} = \frac{P_b \cdot (3 \cdot L_w - 2 \cdot L_{eb})}{6 \cdot h} \quad \textit{(Eq. 4-15)}$$

4.3.3 Bed-Joint Sliding

Sliding can occur in different manners. In addition to the bed-joint sliding analyzed consecutively also sliding in an arbitrary joint or stair-stepped sliding are possible. The differences shall briefly be described. Bed-joint sliding and sliding in an arbitrary joint only differ when some kind of bearing (for example a soft-layer strip bearing) is applied in the bed-joint. Describing the shear resistance with the Mohr-Coulomb criterion

according to equation 4-16, these two kinds of sliding would differ in the parameters of friction (μ) and cohesion (τ_0).

$$V_s = P \cdot \mu + A_e \cdot \tau_0 \qquad \textit{(Eq. 4-16)}$$

For stair-stepped sliding also the tension strength of the head-joint has to be considered. But considering the small value of the head-joint tension strength and the quite large scattering due to the quality of workmanship it would be reasonable to neglect this resistance of the head-joints. Therefore equation 4-16 would also be valid for stair-stepped sliding.

Sliding occurs mainly in the bed-joint. This is because initial rocking eliminates the cohesion in the bed-joint by cracking and therefore the shear resistance in the bed-joint is reduced to:

$$V_s = P_b \cdot \mu \qquad \textit{(Eq. 4-17)}$$

Since according to equation 4-17 the shear resistance depends only on the total vertical load it can be concluded that the presence of flanges has no influence on the shear resistance caused by bed-joint sliding.

4.3.4 Diagonal Tension

The diagonal crack caused by diagonal tension starts to open when the principal tension stress (σ_1) exceeds the diagonal tension strength of masonry (f_{dt}). To evaluate the shear limit an increment of the middle of the in-plane pier (web) is analyzed, supposing that cracking caused by diagonal tension starts at the mid-height of the web an propagates diagonally. (Yi, 2004)

The stress state of this increment is shown in Figure 4.5, including Mohr's Circle that shows the corresponding principal stress state.

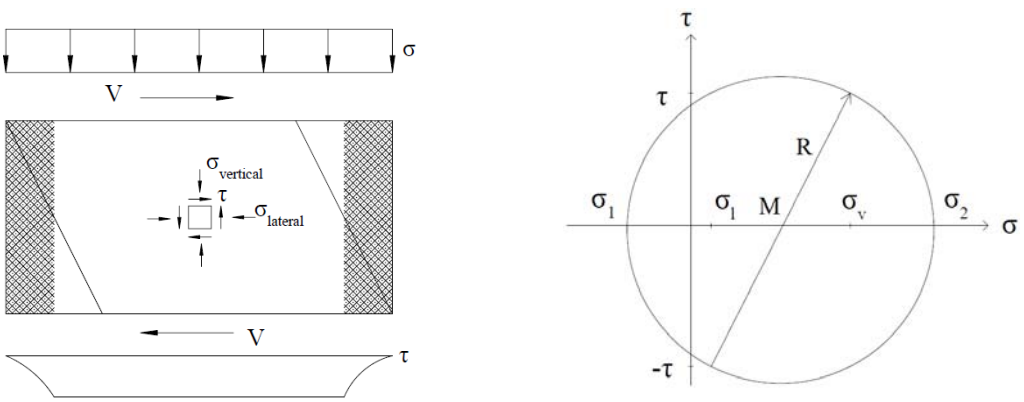

Figure 4.5: Stress state and Mohr's Circle diagonal tension

The limit state of diagonal tension failure is given by inequality 4-18.

$$|\sigma_1| \geq |f_{dt}| \qquad \textit{(Eq. 4-18)}$$

While the vertical stress (σ_v) is relatively simple to calculate according to equation 4-19, the lateral stress (σ_l) is more complicated. The lateral stress at the mid-height of the wall depends on the aspect ratio. For stout walls a lateral confining stress according to equation 4-21 with $\chi = 1$ can be assumed while for slender walls no lateral force is present (χ=0). Yi (2004) proposes to use $\chi = 1$ for aspect ratios $L_w/h \geq 1$ and to consider no lateral stress ($\chi = 0$) for aspect ratios $L_w/h \leq 0.5$.

$$\sigma_v = \frac{P_m}{A_{tot}} \qquad \textit{(Eq. 4-19)}$$

$$A_{tot} = A_w + 2 \cdot A_f \qquad \textit{(Eq. 4-20)}$$

$$\sigma_l = \frac{\chi \cdot V}{h \cdot t} \qquad \textit{(Eq. 4-21)}$$

The shear stress is assumed to be almost constant in the clear width of the in-plane pier due to the effects of the flanges and ζ therefore is equal to 1.0. Equation 4-22 gives the shear stress in the mid-height of the wall.

$$\tau = \frac{\zeta \cdot V}{L \cdot t} \qquad \textit{(Eq. 4-22)}$$

Using equations 4-19, 4-21 and 4-22 in combination with the rules of Mohr's Circle leads to the following shear resistance depending if there is a confining lateral stress or not:

$\chi = 0$:

$$V_{dt} = \frac{\sqrt{A_{tot}} \cdot \sqrt{f_{dt}} \cdot L_w \cdot t}{\sqrt{A_{tot}}} \qquad \textit{(Eq. 4-23)}$$

$\chi = 1$:

$$V_{dt} = \left[\frac{\sqrt{A_{tot} \cdot f_{dt} + P_m} \cdot \sqrt{A_{tot} \cdot f_{dt} \cdot (4 \cdot h^2 + L_w^2) + L_w^2 \cdot P_m} \cdot L_w}{2 \cdot A_{tot} \cdot h} + \frac{(A_{tot} \cdot f_{dt} + P_m) \cdot L_w^2}{2 \cdot A_{tot} \cdot h} \right] \cdot t \qquad \textit{(Eq. 4-24)}$$

In the present thesis only equation 4-23 ($\chi = 0$) is used supposing that for I-shaped URM walls with an aspect ratio of L_w/h=1 no lateral confinement is available.

4.4 Prediction of Shear Strength

To predict the shear strength of I-shaped URM walls in a first step the effective pier model by Yi (2004) in combination with the tests conducted by Vögeli (2014) were analyzed. To evaluate the accuracy of the effective pier model the shear strengths of the test specimens of Vögeli (2014) where calculated according to the four failure modes described in chapter 3. The smallest shear strength is decisive and defines the failure

mode. Sometimes the failure mode is not absolutely clear. In these cases more than one is mentioned whereat the more dominating one is mentioned first. The test results of Vögeli (2014) are repeated in Table 4.1 and complemented with the calculated values by the effective pier model shown in brackets. The failure modes are named in the following way:

V_{tc}: Toe crushing
V_s: Sliding
V_{sh}: Sliding horizontal
V_{sd}: Sliding diagonal
V_{dt}: Diagonal tension

Specimen	**Shear strength V_{max} [kN] (Prediction)**		**Difference**	**Decisive failure mode (Prediction)**	
W0.10	52.5	(49.3)	-6.1	V_{sd} / V_{tc}	(V_{tc})
WE3.10	48.6	(49.3)	+1.4	V_{tc}	(V_{tc})
WE10.10	43.1	(49.3)	+14.4	V_{tc} / V_{sd}	(V_{tc})
WG3.5	33.2	(27.4)	-17.5	V_{tc} / V_{sh}	(V_s)
WG3.10	50.7	(49.3)	-2.8	V_{tc} / V_{sd}	(V_{tc})
WG3.15	74.6	(66.7)	-10.6	V_{dt}	(V_{dt})
WG10.5	36.5	(27.4)	-24.9	V_{tc} / V_{sh}	(V_s)
WG10.10	46.8	(49.3)	+5.3	V_{tc}	(V_{tc})
WG10.15	60.5	(66.7)	+10.2	V_{dt}	(V_{dt})

Table 4.1: Results and prediction rectangular URM walls (Vögeli, 2014)

Not knowing the value for the diagonal tension strength of the used masonry its value was taken to fit the model best to the observed values. To do so only the tests where diagonal tension is decisive can be used because the diagonal tension strength has only a computational influence on this failure mode. This fitting leads to a value of 0.212 N/mm^2. This value is very close to 5% of the masonry compressive strength (0.24 N/mm^2) what Lee et al. (2008) are recommending as a value for the diagonal tension strength of masonry. All the material properties used for the prediction of Vögeli's (2014) tests are listed in Table 4.2. The levels of precompression were set according to Table 3.1 to the effective values of the tests.

Material properties	
f_m [MPa]	4.7
f_{dt} [MPa]	0.212
μ [-]	0.71 (no layer or elastomer) 0.44 (granulate)
γ [kN/m^3]	13

Table 4.2: Material properties prediction rectangular URM walls (Vögeli, 2014)

As can be seen in Table 4.1 with the mentioned choice of the diagonal tension strength the failure mode predicted by the effective pier model always fits the results although the model is not necessarily predicting the dominating one when there are two failure modes observed. When looking at the predicted values for shear strength it can be seen that except for the sliding failure mode the predicted values are within a range of ±15% of the observed maximum strength. Most values are even within a range of ±10% which is really precise considering the complex behavior of masonry. Overestimations are marked with a plus sign, underestimations therefore with a minus sign. The rather high difference in the predicted and observed values for the sliding failure mode is possibly due to an underestimation of the friction coefficient or the presence of cohesion in the middle part of the wall length despite the initial rocking behavior.

The observed consistency of the effective pier model to the tests lets us expect a plausible prediction of shear strength using the adapted modified model described in chapter 4.3. The predicted values of shear strength depend on the following parameters:

- the material properties
- the level of precompression
- the type of SLS bearing applied
- the boundary condition
- and the geometry of the wall.

The thickness of the soft-layer is not taken into account in the theoretical model.

Having tested three additional smaller wall specimens in the run-up to the tests of the I-shaped URM walls the actual compressive strength of 5.45 N/mm^2 (see chapter 6.3.3) can be used for the masonry to predict the shear strength of the specimens. All material properties used for the prediction of the shear strength for the I-shaped URM walls are listed in Table 4.3.

Material properties	
f_m [MPa]	5.45
f_{dt} [MPa]	0.212
μ [-]	0.71 (no layer or elastomer) 0.44 (granulate)
γ [kN/m^3]	13

Table 4.3: Material properties prediction I-shaped URM walls

Using the value of 0.212 N/mm^2 for the masonry diagonal tension strength due to the explanation above the following failure modes and corresponding values of shear strength are expected for I-shaped URM walls with a cantilever boundary condition.

Specimen	Predicted shear strength V [kN]	Predicted decisive failure mode
I-0.10	75.0	V_{dt}
I-E3.10	75.0	V_{dt}
I-E10.10	75.0	V_{dt}
I-G3.5	43.7	V_s
I-G3.10	75.0	V_{dt}
I-G3.15	87.7	V_{dt}
I-G10.5	43.7	V_s
I-G10.10	75.0	V_{dt}
I-G10.15	87.7	V_{dt}

Table 4.4: Prediction I-shaped URM walls

The levels of precompression for the prediction were set to the theoretical target values of 0.3 MPa (5%), 0.6 MPa (10%) and 0.9 MPa (10%) respectively. An overview of the shear strength for all failure modes in each case is given in Figure 4.6.

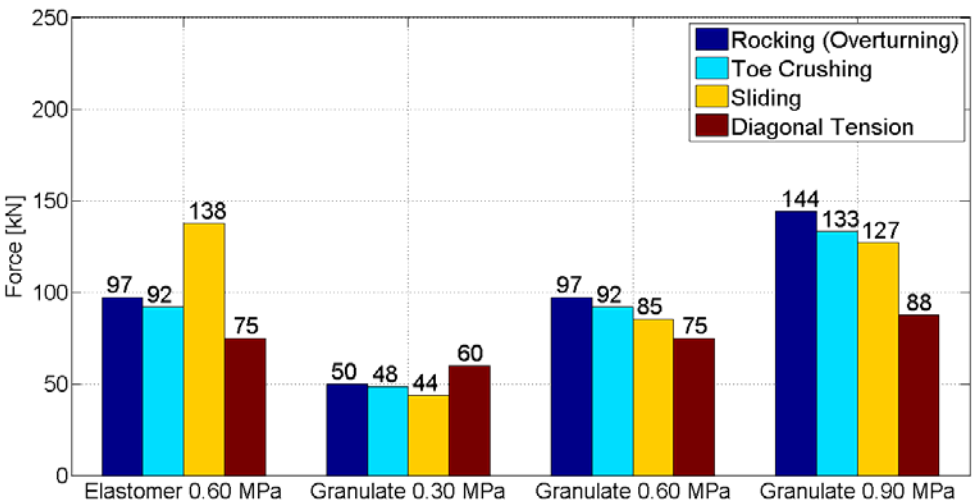

Figure 4.6: Visualization prediction I-shaped URM walls

In most cases the shear strengths are relatively well separated and the decisive failure mode is therefore clearly predictable. Only in case of the granulate layer and a small precompression of 0.3 MPa the failure mode is not completely distinct. In this case beside sliding which exhibits the smallest shear strength also toe crushing may occur. To name rocking as a failure mode the specimens would have to fulfill an overturning movement. This rigid body movement seems not very likely for a masonry wall. So when the residual compressed part of the bottom of the wall would get too small a toe crushing failure mode would be assumed to happen. Nevertheless this geometric stability problem has to be kept in mind during the test also because the flange provides a far better edge to overturn than a rectangular wall and also adds stability to the web making the wall more rigid.

5 Comparison of Results Based on Effective Pier Model with its Modification

In the following chapter the shear strength and failure modes of rectangular URM walls are compared to the ones of I-shaped URM walls. To compare the two wall types the masonry compressive strength is set according to Swiss code SIA 266. All material properties can be seen in Table 5.1.

Material properties	
f_{xd} [MPa]	7.0
f_{dt} [MPa]	0.212
μ [-]	0.71 (no layer or elastomer) 0.44 (granulate)
γ [kN/m^3]	13

Table 5.1: Material properties (SIA 266, 2003)

The values of precompression are set to 0.3 MPa, 0.6 MPa and 0.9 MPa which are the theoretical target values of precompression in the tests of chapter 6. Based on this information the shear strength according to the different failure modes is calculated by means of the effective pier model according to chapter 3.2.2 for the rectangular URM walls and by means of the adapted modified effective pier model according to chapter 4.3 for the I-shaped URM walls. All calculations are based on a cantilever boundary condition.

First of all it can be seen that the flanges lead to a general rise in shear resistance for all failure modes. This intuitive theoretical effect exists for elastomer and granulate SLS bearings and for all the different levels of precompression.

For the wall without a SLS bearing and the ones with elastomer SLS bearings the results are shown in Figure 5.1.

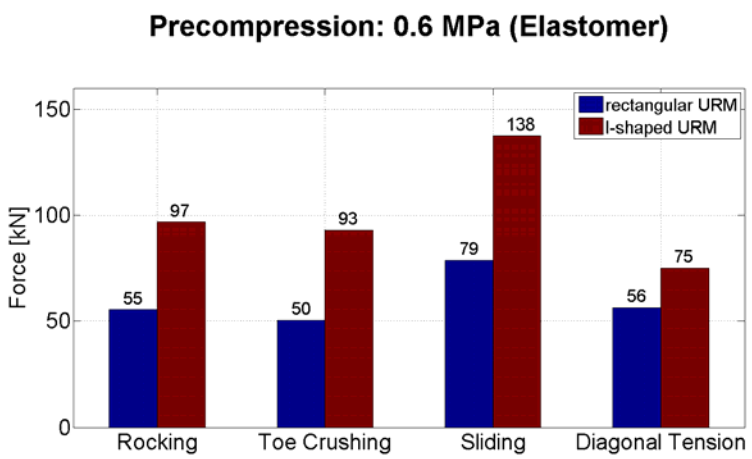

Figure 5.1: Prediction of shear strength 0.10, E3.10 and E10.10

Under the constraints mentioned above the flanges cause a change in the failure mode from toe crushing to diagonal tension. In the present case it leads to a higher shear resistance of 75 kN which is equal to a rise of 50 %.

The results of the computations for the wall specimens with granulate SLS bearings and a precompression of 0.3 MPa can be seen in Figure 5.2.

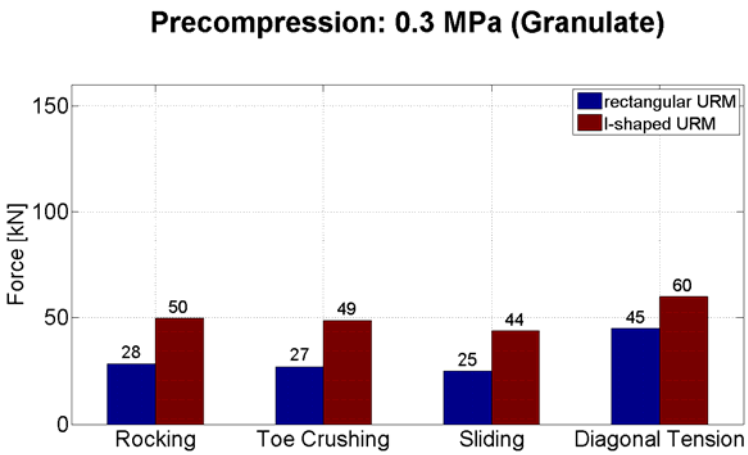

Figure 5.2: Prediction of shear strength G3.5 and G10.5

Since all the values of the different failure modes are close together probably a combined failure mode would be predicted in this case. Keeping strictly to the calculated values the walls would fail in sliding independent of the presence of flanges. The rise in shear strength of 34 % to a value of 44 kN for the wall with flanges is caused by a higher total vertical force. The applied vertical force in the case with flanges is higher because the cross-section area is bigger keeping the vertical stress constant for both cases.

Increasing the precompression from 0.3 to 0.6 MPa leads to the results of Figure 5.3.

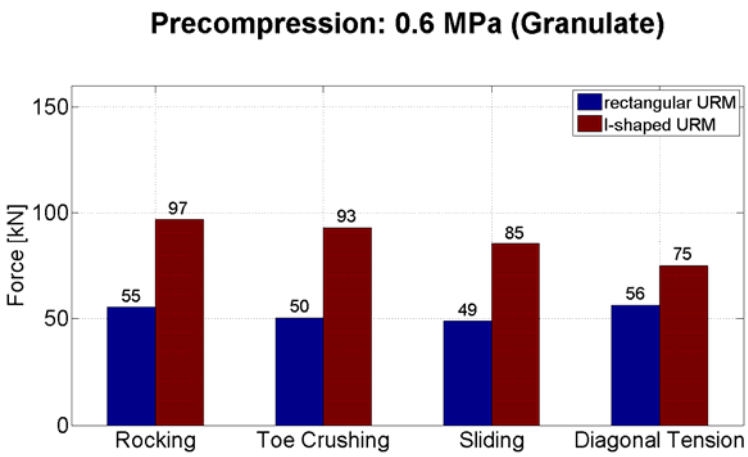

Figure 5.3: Prediction of shear strength G3.10 and G10.10

The increase of the normal force has a positive influence on the lateral strength of the wall. The rectangular URM walls as well as the I-shaped URM walls exhibit higher shear strengths for all failure modes. While for the rectangular URM walls the failure mode does not change for the I-shaped URM walls the higher normal force changes the failure mode form sliding to diagonal tension. Regarding the effect of flanges also a change from sliding to diagonal tension can be observed.

For a high precompression of 0.9 MPa the results are shown in Figure 5.4.

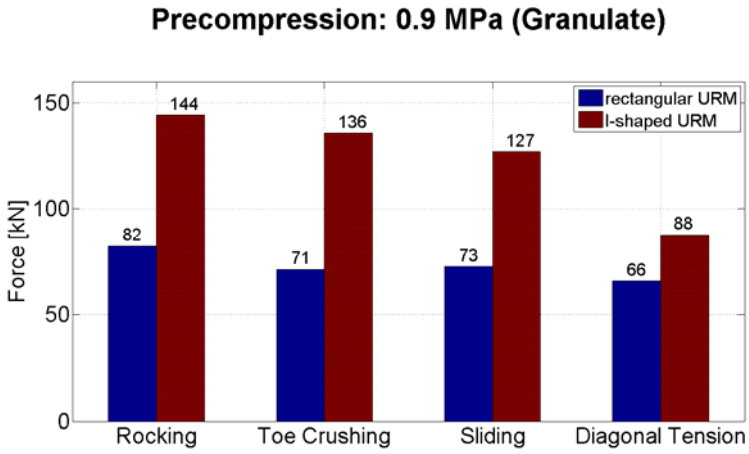

Figure 5.4: Prediction of shear strength WG3.15 and WG10.15

For high precompression no change in failure mode due to the flanges is observed expecting both rectangular and I-shaped URM walls to fail in diagonal tension. If the results are compared to the ones with a precompression of 0.6 MPa another general rise in shear strength can be observed.

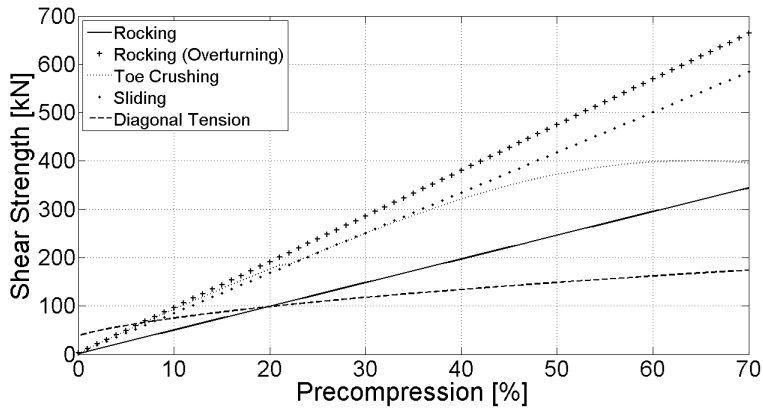

Figure 5.5: Shear strength I-shaped URM walls (granulate SLS bearings)

Figure 5.5 shows that there is an initial rocking behavior as long as the precompression is lower than about 20 % of the compressive strength. When the precompression is higher the wall will theoretically fail directly in diagonal tension without any rocking behavior.

6 Experimental Tests of I-Shaped URM Walls

The following test series is the first one testing flanged URM walls in the HIF laboratory of the ETH Zurich. The aim of the test is to understand the influence of flanges of I-shaped URM walls more in detail and to take them into account for the seismic verification of existing buildings and for the design of new buildings using URM walls to resist seismic forces.

6.1 Test Series

The test series that was planned to conduct in the HIF laboratory on the ETH Zurich is shown in Table 6.1.

Specimen	Material	Thickness [mm]	Vertical load [%]	Name
1	Elastomer	3	10	I-E3.10
2	Elastomer	10	10	I-E10.10
3	Granulate	3	5	I-G3.5
4	Granulate	3	10	I-G3.10
5	Granulate	3	15	I-G3.15
6	Granulate	10	5	I-G10.5
7	Granulate	10	10	I-G10.10
8	Granulate	10	15	I-G10.15
9	No layer	-	10	I-0.10

Table 6.1: Test series I-shaped URM walls

To conduct the tests a new test setup had to be installed (see chapter 6.4). Due to a delay of the delivery of the force transmission plate on top of the wall and a defective jack the test program had to be reduced to five tests for the present master's thesis. The five specimen tested are marked with a gray background.

It seems noteworthy that the control specimen I-0.10 without a SLS bearing suffered from poor workmanship and therefore the results have to be handled with particular caution. Furthermore this specimen served as a prototype specimen to check the test setup and expose potential problems during the tests.

6.2 Wall Specifications

The wall specifications are given in Figure 6.1. The specimens are 1.2 m high, 1.2 m long and 0.15 m thick. The flanges are added at the ends of the walls giving them an I-shaped profile. The thickness of the flanges is 0.15 m and therefore identical to the one of the web. The remaining clear width of the web is equal to 0.90 m. The specimens are built in running bond and the bed- and head-joints are fully filled with mortar.

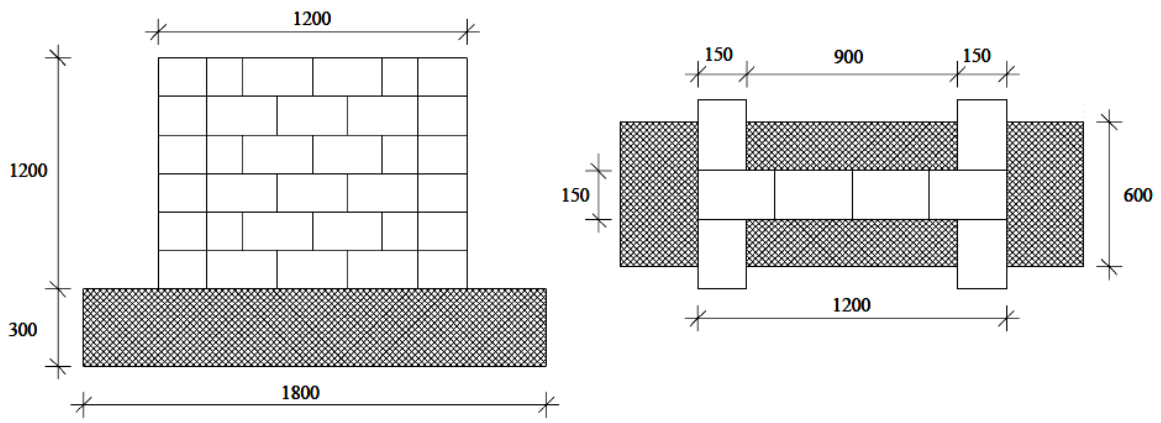

Figure 6.1: Geometry of I-shaped specimens

The Specimens are built on a 30 cm thick concrete basement which can be tightened to the strong floor at both ends.

Figure 6.2: Building process I-shaped URM walls

6.3 Material Properties

To evaluate the material properties of the masonry and its components six tests of mortar specimens and three tests of masonry specimens were conducted within the scope of the present thesis. The brick used for the masonry wall specimens is the same as the one Vögeli (2014) used for his tests and was manufactured by the same supplier. So only the test results of Vögeli (2014) are repeated for convenience.

6.3.1 Mortar

The mortar used to build the five wall specimens was mixed using the following ratio of the components 1:0:4 (cement:lime:sand by mass). The ratio of cement and water was equal to w/z = 0.6. When the wall specimens were built on the 22nd of January 2014 also six four-sided mortar prisms with nominal dimensions of 40 x 40 x 160 mm were prepared. Three of the six prisms were stored directly next to the wall specimens in the HIF laboratory and the other three prisms were stored in a separate climatic chamber at constant temperature of 20° Celsius and constant relative air humidity of 95%.

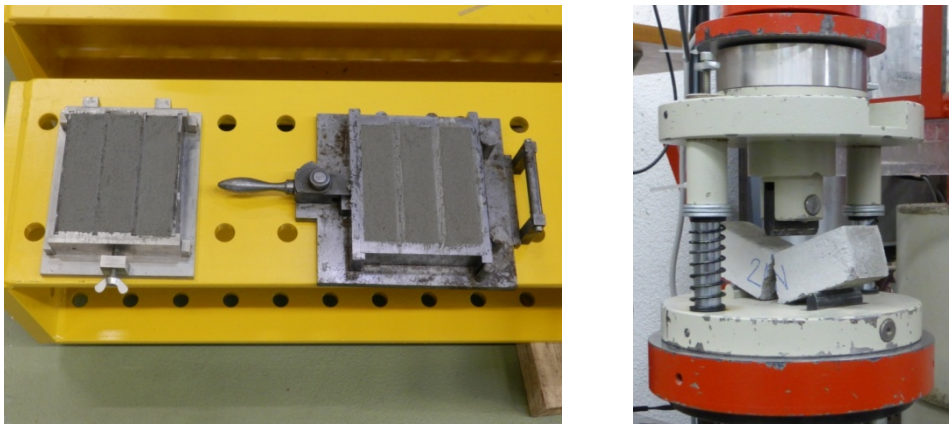

Figure 6.3: Mortar test: (l) Preparation of the six mortar specimen, (r) Three-point bending test specimen 2N

All six prisms were tested on the 3rd of June 2014. Both groups of three prisms where tested the same way according to the following procedure:

1. Three-point bending test on the first of the three prisms.
2. Compressive strength test (force-controlled) on each of the two resulting pieces of the first prism.
3. Test of the modulus of elasticity on the other two specimens up to a stress-level of 30% of the measured compressive strength under point 2.
4. Three-point bending test on the other two specimens.
5. Compressive strength test (force-controlled) on each half of the other two specimens.

The three-point bending tests and the compressive tests were conducted according to SIA 262/1 appendix G while the test of the modulus of elasticity was conducted according to EN 196-1:2005.

The results of the tests are listed in the following two separate tables according to their storage. In the case of the values marked with a star the compressive strength differs more than 10% from the average of the six test results therefore these results have to be neglected for the calculation of the average (SIA 266/1, 2003).

Prism	Compressive strength [MPa]	Bending strength [MPa]	Modulus of elasticity [MPa]
1 N	17.35 / 17.63	4.47	-
2 N	16.21 / 17.43	5.06	14598
3 N	17.36 / 20.66*	5.27	14263
Average	17.19	4.93	14431

Table 6.2: Results mortar test prisms stored in the climatic chamber (not considered for calculation of the average)*

Prism	Compressive strength [MPa]	Bending strength [MPa]	Modulus of elasticity [MPa]
1 T	1.94 / 1.90	0.76	-
2 T	1.93 / 1.99	0.86	4032
3 T	2.18* / 1.84	0.82	4214
Average	1.92	0.81	4123

Table 6.3: Results mortar test prisms stored next to the wall specimens (not considered for calculation of the average)*

The results of the mortar prisms stored next to the wall specimens attract attention because the observed test values are very small, far below the values required for standard mortar according to SIA 266. Not even the minimum required mortar compressive strength of f_{mk} > 5.0 MPa is fulfilled for the prisms stored next to the wall specimens. But following strictly the Swiss code SIA 266/1 only the prisms stored in the climatic chamber have to fulfill this criterion.

6.3.2 Bricks

The bricks are the same as Vögeli (2014) used and were manufactured by the same supplier with nominal dimensions of 290 x 150 x 190 mm. In the scope of his master's thesis 15 bricks were tested according to SIA 266 (2013), SN EN 771-1 (2011) by the testing and research institute "p+f Sursee". (Vögeli, 2014) The results are repeated her for convenience.

SwissModul B 15/19	
Length [mm]	288
Width [mm]	148
Height [mm]	190
Form factor [-]	1.21
Void area [%]	45
Compressive strength [MPa]	27.8
Normalized compressive strength [MPa]	33.6
Transverse tensile strength [MPa]	7.7
Mass of a Brick [g]	7288
Gross density [kg/m³]	905
Moisture suction [kg/(m²*min)]	2.7

Table 6.4: Results brick tests (Vögeli, 2014)

6.3.3 Masonry

Typically the mortar is weaker than the bricks. For Swiss standard masonry the minimal vertical strength of the mortar is equal to f_{mk}=15.0 N/mm^2 while the minimal vertical strength of the bricks is equal to f_{bk}=28.0 N/mm^2. The different stress-strain behavior of

the materials leads to a distinct smaller vertical strength of masonry equal to f_{xk}=7.0 N/mm^2. (SIA 266, 2003)

To evaluate the vertical compressive strength (f_{xk}) and the modulus of elasticity (E) of the tested masonry walls three additional specimens where built named with the capital letter R (Rilem) numbered 1 to 3. They were tested according to EN 1052-1 (1998) in the HIF laboratory of the ETH Zurich. The specimens were built at the same time as the I-shaped wall specimens with the same type of bricks and the same mortar. They were stored next to them in the HIF laboratory. The geometry of the three additional specimens is given by a length of 0.60 m, a height of 1.0 m and a thickness of 0.15 m.

Figure 6.4: Additional specimen R1 in the test setup

To test the specimens they were placed centrically between two steel beams. To guarantee a uniformly distributed load transmission a soft wood fiberboard was placed on top of the wall. The loading was applied deformation-controlled by means of three speed steps. At the beginning the loading speed was set to 2.0 mm/min till a force of 100 kN was reached. At this point the speed was increased to 1.0 mm/min up to a force of approximately 350 kN and finally the speed was set to 0.2 mm/min until failure occurred. Using this procedure the failure of all three specimens was reached in a time frame of 15 to 30 minutes demanded in EN 1052-1. The loading curves are plotted in Figure 6.5.

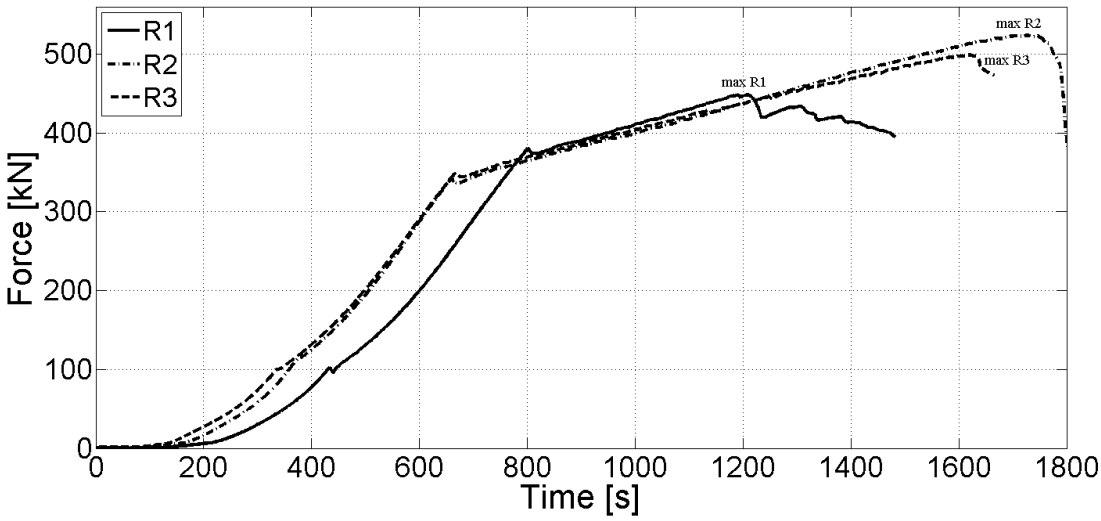

Figure 6.5: Loading curves compression tests

The average compressive strength of the three tests is equal to 5.45 MPa and the young's modulus is equal to 2364 N/mm^2. To get the characteristic values the average of the compressive strength of the three tests has to be divided by the factor 1.2 and rounded to 0.1 N/mm^2. The average young's modulus of the three tests has to be rounded to 100 N/mm^2. All the values are given in Table 6.5.

Specimen	Compressive strength f_x [MPa]	Young's modulus E [MPa]	Time to failure T [min]
R1	4.98	2241.0	20.2
R2	5.82	2407.5	28.8
R3	5.54	2443.7	27.0
Average	**5.45**	**2364.1**	**25.3**
	f_{xk} [MPa]	**E_k [MPa]**	
Average char.	4.5	2400	

Table 6.5: Results of compression tests

6.3.4 SLS Bearings

Two types of SLS bearings, elastomer and granulate, were used in the tests of chapter 6. As usual in practice the soft-layer is placed in the interface between the concrete basement and the first mortar bed-joint as can be seen in Figure 6.6. Its main functions are to avoid stress peaks and to prevent the moisture from rising in the bricks caused by their capillarity.

Figure 6.6: Position of SLS bearing (granulate 10 mm)

The material properties of the SLS bearings are listed in Table 6.6. Both products are provided by the same supplier "mageba sa" and shown in Figure 6.7. Very low information is given in the technical report. In the scope of this thesis only the friction coefficient is used.

Figure 6.7: SLS bearings: (l) Elastomer, (r) Granulate

Material Properties	Elastomer	Granulate
μ [-]	0.71	0.44
$\sigma_{v,max}$ [MPa]	5	5

Table 6.6: Material properties SLS bearings (Mojsilović, 2012) (Vögeli, 2014)

6.4 Test Setup

The walls were tested in the HIF laboratory of the ETH Zurich. The test setup is shown in Figure 6.9. The lateral force is applied on the upper beam by a horizontal hydraulic actuator and transferred through the lower beam and a steel plate to the wall specimen. The steel plate between the lower beam and the top of the wall exhibits dimensions of 2.70 x 0.80 x 0.09 m and guarantees a direct load transfer from the lower beam to the web and the whole flanges of the wall and therefore provides a uniform distribution of the vertical loading and an equal horizontal load transmission.

The lower side of the steel plate had to be prepared with a layer of silica sand (see Figure 6.8) because the friction coefficient of blank steel would be far too low to transmit the lateral forces to the specimen.

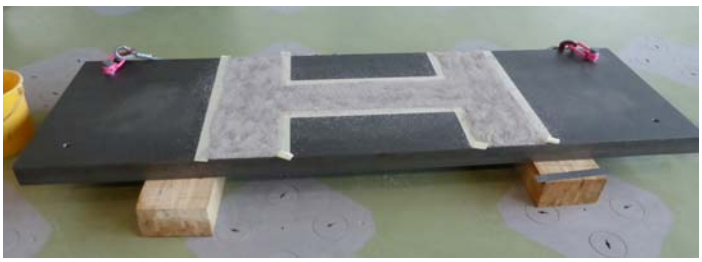

Figure 6.8: Application of silica sand on load transmission plate

The vertical load is applied by two vertical hydraulic actuators on both ends of the wall by pulling down the upper beam. To set the correct precompression level the self weight of the complete steel construction resting on the two vertical hydraulic actuators has to be determined. In addition to the green shaded parts in Figure 6.9, which are arranged symmetrically to the center of the wall, there is also a certain weight to be considered caused by the bearing parts (red shaded parts on the left in Figure 6.9) of the horizontal hydraulic actuator and a certain part of its self weight transferred to the upper beam marked with a red arrow in Figure 6.9. This weight has to be counterbalanced by some extra weight on the right end of the upper beam (red shaded parts on the right in Figure 6.9) to provide a uniformly distributed vertical loading to the specimen. The total weight of the green and red marked parts of the test setup is equal to 54.7 kN and has to be subtracted from the pulling force of the two vertical hydraulic actuators applying the target level of precompression.

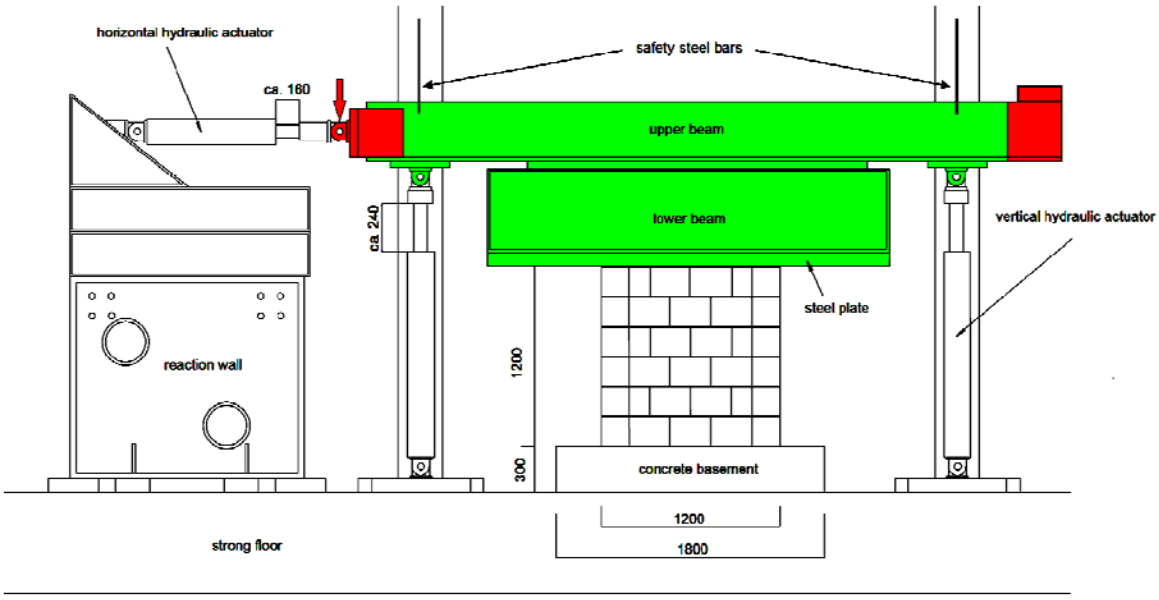

Figure 6.9: Test setup I-shaped URM walls

This setup presumes the vertical hydraulic actuators to be hinged on both ends to prevent any restraints when moving the system in the lateral direction. Using this test setup, applying the axial force by pulling, roller bearings between the vertical pushing actuator(s) and the loading beam are no longer needed making the mechanical setup more simple. But having a look at the statics of the system the height difference between the top of the wall and the horizontal actuator leads to a moment that is induced on top of the wall. The value of this moment depends on the horizontal force and is equal to 43% of the moment at the bottom of the wall. The statics of the test setup are shown in Figure 6.10.

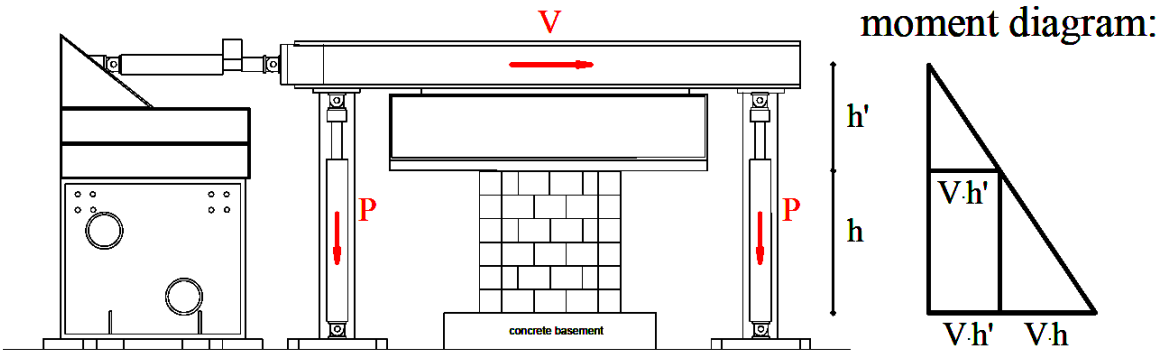

Figure 6.10: Statics test setup

Therefore the boundary condition of the tests of chapter 6.9 can no longer be assumed as cantilever and the influence of the moment on top of the wall has to be taken into account for the theoretical model of chapter 4. The induced additional moment leads to a higher effective aspect ratio (h/L) of the walls or a higher shear span (H_0) to express it in other words. The direct comparison of the shear spans of the different tests is shown in Figure 6.11.

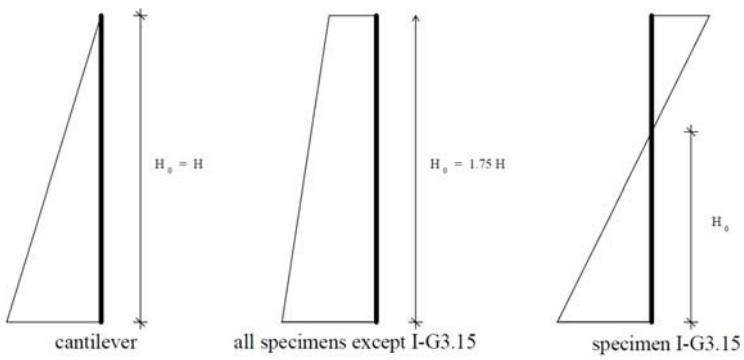

Figure 6.11: Shear span I-shaped URM walls

Due to this change the adapted modified effective pier model was therefore adjusted in chapter 6.7 for the prediction of the shear strength.

6.5 Test Procedure

The specimens tested in the context of the present master's thesis were not tested using a cantilever boundary condition as initially intended. Due to the geometry of the new test setup an additional moment is applied at the top of the wall when the force in both vertical actuators is kept constant during the tests. The bottom of the wall is fixed. The specimens are loaded in the following way.

In a first step the axial load is applied monotonically until the provided precompression level of the wall specimens is reached. In a second step the lateral load is applied by a static cyclic displacement pattern according to Table 6.7. The cycles are applied sinusoidal and each cycle is repeated twice.

Amplitude step number	**Target displacement [mm]**	**Average loading speed [mm/min]**	**Duration 2 cycles [min]**	**Frequency [10^{-3} Hz]**
1	0.2	1	1.6	10.42
2	0.5	1	4.0	4.17
3	1.0	1	8.0	2.08
4	1.5	1	12.0	1.39
5	2.0	3	5.3	3.14
6	5.0	3	13.3	1.25
7	10.0	3	26.7	0.62
8	15.0	10	12.0	1.39
9	20.0	10	16.0	1.04
10	30.0	10	24.0	0.69
11	40.0	20	16.0	1.04
12	50.0	20	20.0	0.83

Table 6.7: Horizontal displacement pattern

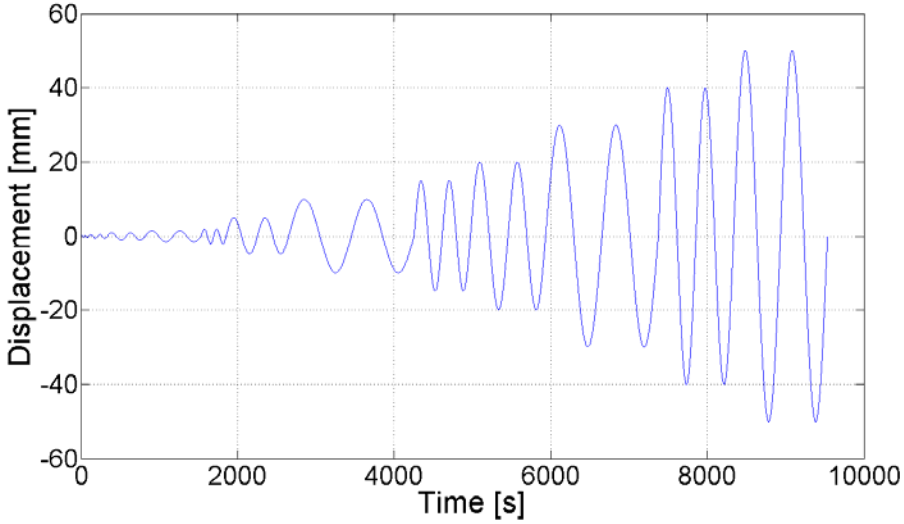

Figure 6.12: Plot horizontal displacement pattern

As shown in Tomažević (1996) the type of imposed lateral displacement pattern has a significant influence on the force displacement response of the specimen. Although there are differences between the results by applying a static cyclic displacement pattern compared to a dynamic simulation of an earthquake response the results are much more realistic than by applying a static monotonic displacement pattern. And as many experimental tests are conducted this way the gained data is comparable to other test results. In Figure 6.13 the resulting hysteresis envelopes of different lateral displacement patterns are shown for an applied precompression of 1 MPa. It can be seen that for a static monotonic displacement pattern the resulting maximum force and displacement would be clearly overestimated.

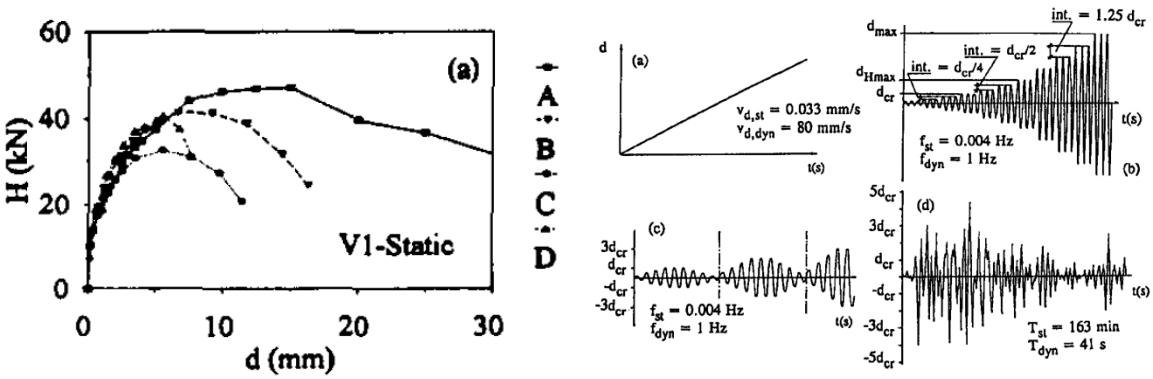

Figure 6.13: Influence of imposed lateral displacement pattern (Tomaževič, Lutman, & Petković, 1996)

6.6 Methods of Result Evaluation

Often the direct comparison and calculation of characteristic values of the measured data is not suitable. Therefore they have to be idealized. The procedures and formulas used in this master's thesis are shown in the following sub-chapters.

6.6.1 Bilinear Idealization of Hysteresis Loops

In a first step the measured hysteresis loops of the tests are simplified by means of a capacity curve. The capacity curve is attained by connecting all points with maximum displacement of each first cycle of all conducted loading steps. In a second step the capacity curve is transferred to a bilinear idealization according to Tomažević (1999). In this procedure the effective stiffness (K_e) is calculated using the point of the capacity curve where the force is equal to 0.7 times the maximum force of the capacity curve (V_{max}). The ultimate force (V_u) is found by presuming the area under the experimental and the idealized capacity curve to be equal. The ultimate displacement (d_u) is defined to be the displacement after a 20% drop of the maximum force or the maximum displacement measured if no drop of 20% of the maximum force is observed.

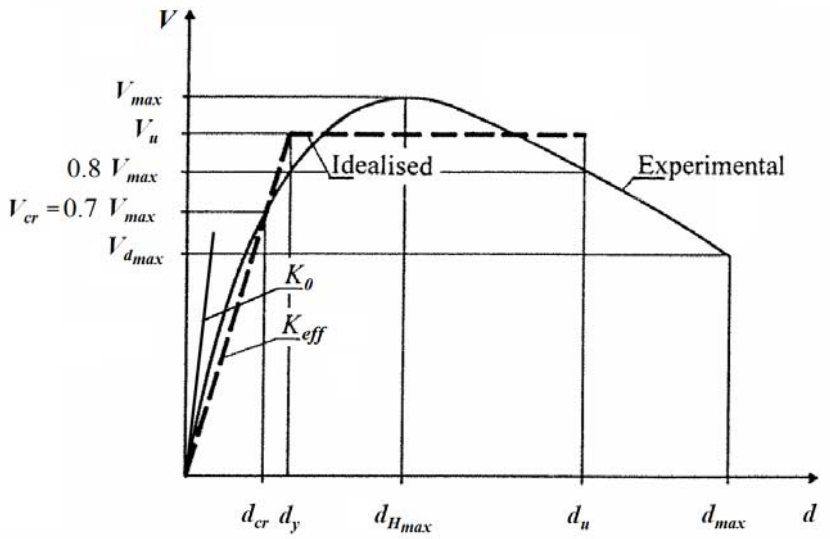

Figure 6.14:Bilinear idealization (Tomaževič, 1999)

6.6.2 Calculation of Characteristic Values

The initial stiffness is calculated according to equation 6-1 by using the first measured data point. Since the consequent use of the first measured data point might lead to unrealistic high values the second measured data point was used in such cases.

$$K_0 = \frac{V_0}{d_0} \qquad \textit{(Eq. 6-1)}$$

The effective stiffness is calculated the same way according to equation 6-2 using the data point where 70% of the maximum force is reached.

$$K_{eff} = \frac{V_{cr}}{d_{cr}} \qquad \textit{(Eq. 6-2)}$$

The ductility factor is calculated according to equation 6-3.

$$\mu = \frac{u_m}{u_y} \qquad \textit{(Eq. 6-3)}$$

This factor describes the ability of the specimen to sustain plastic deformations without failing. Although unreinforced masonry is known to be a brittle material experimental tests show some kind of plastic deformation capacity.

6.7 Adjustment of the Modified Effective Pier Model

The adapted modified effective pier model derived in chapter 4.3 is based on a cantilever boundary condition where rotations and displacements are prevented on the bottom of the wall and are not restraint on top of the wall. Due to the construction details of the test setup this boundary condition could not be fulfilled during the tests. As shown in chapter 6.4 there is a moment induced on top of the wall. To take this change in the boundary condition into account the adapted modified effective pier model is adjusted.

6.7.1 Shear Resistance according to the Different Failure Modes

Basically the additional moment M'=V*h' has to be taken into account in the moment equilibrium of the equations derived in chapter 4.3. In the following the changes are described more in detail.

Concerning the failure mode rocking equation 4-2 has to be adjusted to equation 6-4.

$$M_b = V \cdot h + V \cdot h' \qquad \textit{(Eq. 6-4)}$$

This leads to the new smaller maximum lateral force for the start of a rocking motion and for the resistance of overturning as shown in equations 6-5 and 6-6.

$$V_r = \frac{P_b \cdot \left[L_w^3 \cdot t + 6 \cdot A_f \cdot \left(t_f - L_w\right)^2\right]}{6 \cdot L_w \cdot \left(L_w \cdot t + 2 \cdot A_f\right) \cdot (h + h')} \qquad \textit{(Eq. 6-5)}$$

$$V_{ro} = \frac{L_w}{2} \cdot \frac{(W_{tot} + P_t)}{(h + h')} \qquad \textit{(Eq. 6-6)}$$

For the failure mode toe crushing in both cases, $L_{eb} > t_f$ and $L_{eb} < t_f$, the equilibrium of moments (equation 4-11 and 4-15) has to be adjusted. The new maximum lateral forces for toe crushing are given in the equations 6-7 and 6-8. The adjustments cause a reduction in the shear resistance for this failure mode.

$L_{eb} > t_f$:

$$V_{tc} = \frac{P_b \cdot \left[L_{eb}^2 \cdot (3 \cdot L_w - 2 \cdot L_{eb}) \cdot t + 3 \cdot A_f \cdot \left(2 \cdot L_{eb} - t_f\right) \cdot \left(L_w - t_f\right)\right]}{6 \cdot \left[L_{eb}^2 \cdot t + A_f \cdot \left(2 \cdot L_{eb} - t_f\right)\right] \cdot (h + h')} \qquad \textit{(Eq. 6-7)}$$

$L_{eb} < t_f$:

$$V_{tc} = \frac{P_b \cdot (3 \cdot L_w - 2 \cdot L_{eb})}{6 \cdot (h + h')} \qquad \textit{(Eq. 6-8)}$$

The lateral resistance of the failure mode sliding depends only on the total vertical load applied. The additional moment changes only the distribution of the vertical stress at the bottom but the total load applied remains the same. Therefore the additional moment has no influence on the lateral strength for the failure mode sliding.

To determine the influence on the failure mode diagonal tension the stress exposure of an increment in the middle of the wall has to be analyzed. The elastic stress distribution according to the normal force and the additional moment on top of the wall is visualized in Figure 6.15. In the present cases of the tests in chapter 6 the moments do not decompress the top cross section of the walls.

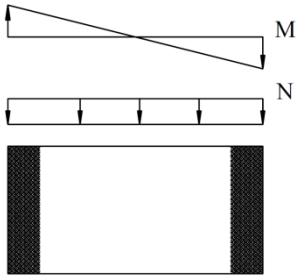

Figure 6.15: Stress distribution on top of the wall

If the cross section on the bottom of the wall could withstand tension and under the assumption of a linear stress distribution the additional moment would have no influence on the stress exposure of the increment in the middle of the wall. This is different when tension is neglected. In this case the vertical stress distribution is much more complicated and is also changing over the height of the wall. As a simplification the influence of the additional moment is neglected in this model adjustment knowing that this is a rather rough approximation of the reality. Some more detailed analysis of this failure mode considering top moments should be done.

6.7.2 Adjustment of the Prediction of the Shear Strength

For a later comparison of the experimental results of the tests with the results according to the theoretical adapted modified effective pier model, the prediction of the shear strength of chapter 4.4, which presumes a cantilever boundary condition, has to be adapted to the adjustments of the model done in chapter 6.7.1.

For a certain boundary condition the predicted shear strength depends on the material properties, the geometry, the level of precompression and on the type of SLS bearing applied. The results of the prediction are shown diagrammatically in Figure 6.16. Only the predicted shear strength for the tests conducted in chapter 6 are shown. Since the

thickness of the soft-layer is not taken into account in the theoretical model the predicted shear strength for specimens with a different soft-layer thickness but the same level of precompression is identical. Therefore the prediction for the five specimens tested in chapter 6 consists only of three different values. Since due to a manipulation failure the boundary condition of specimen I-G3.15 was neither equal to the rest of the tested specimens nor equal to cantilever no prediction of the shear strength is available for this test.

For each case the shear resistances for all four failure modes according to the equations of chapter 6.7.1 are calculated and the lowest value is assumed to be decisive for the ultimate failure of the specimen. In Figure 6.16 the strength prediction is visualized including the shear strength limit for the start of a rocking motion.

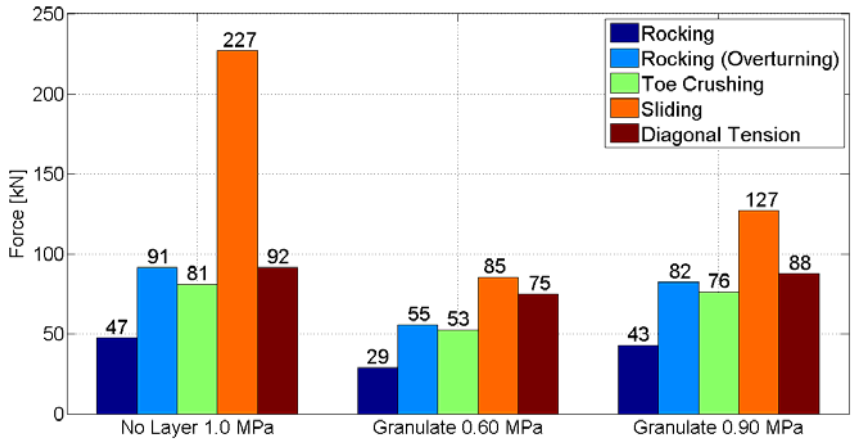

Figure 6.16: Adjusted prediction of shear strength I-shaped URM walls

Having a closer look at the predicted values of the different failure modes it can be seen that in all cases the shear resistance due to sliding is distinct higher than the other values and therefore a sliding failure is not expected for any test. The calculated shear resistances according to the other three failure modes are relatively close together. In all three cases toe crushing is expected to be decisive showing the lowest value of shear resistance. The shear resistance due to rocking (overturning) is always a little bit higher than the shear resistance due to toe crushing what seems to be reasonable. Due to the additional moment and the expected distinct rocking behavior in all three prediction cases overturning might be theoretically plausible but in reality for the applied levels of precompression it seems much more likely to observe a toe crushing failure before overturning what is also predicted by the model.

Figure 6.17 shows the shear resistances of the four failure modes as a function of the level of precompression for no layer and a granulate SLS bearing.

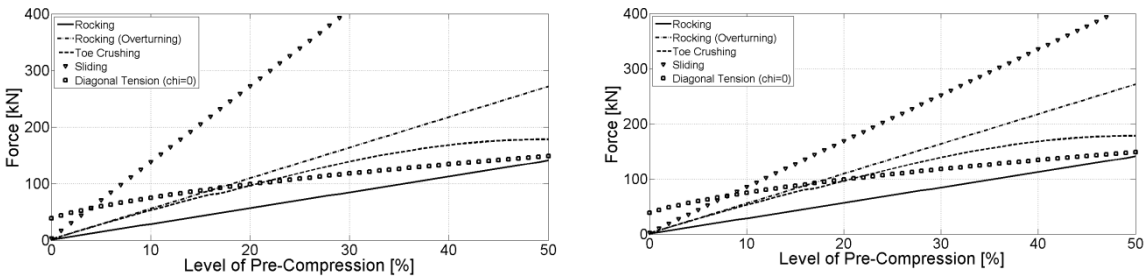

Figure 6.17: Shear resistance as a function of the level of precompression: (l) No layer, (r) Granulate SLS bearing

With a higher level of precompression the shear resistance due to the failure mode diagonal tension gets lower than the one due to toe crushing but is not expected to be decisive in the present cases. It can also be seen that a sliding failure is not expected at any level of precompression under the adjusted boundary conditions. The difference between rocking (overturning) and toe crushing is growing with an increasing level of precompression what seems to be reasonable.

Combining the findings of chapter 6.7.1 with the predicted failure modes of the present chapter it can be concluded that a shear span bigger than 1 (leading to an additional moment on the top of the wall) leads to a smaller shear resistance.

6.8 Measurement Instrumentation

During the tests the applied forces on the specimens were measured with load cells installed on the top of the pistons of the three hydraulic actuators. The hydraulic actuators were also equipped with liner variable differential transformers (LVDT) measuring directly the path of the cylinder piston. The displacements measured on the walls are described in chapter 6.8.1. In addition to the conventional measurement of the displacements digital image correlation (DIC) was established. This measuring method is described in chapter 6.8.2. The cracks were identified by eye with the help of a crack light and marked on the back of the wall after every two cycles of each target displacement. To simplify the identification of the cracks the wall specimens were completely painted in white.

6.8.1 Linear Variable Differential Transformer (LVDT)

Conventionally the deformations of wall specimens are recorded by measuring the displacement between some pairs of clearly defined points. For this measuring technique usually linear variable differential transformers (LVDT's) are used because they are simple to handle and easily available due to their widely use in experimental research. They consist of a coil assembly and a core. Each part is fixed to a well defined point of the wall and their relative displacement leads to a change of the position of the core in the coil assembly. An electronic signal is generated by means of magnetic induction and transformed to a displacement value. (Santhosh & Roy, 2012)

The setup of LVDT's on the wall specimens is shown in Figure 6.18. In total 16 LVDT's are installed. Eight LVDT's measure the deformations of the wall specimen itself, two of them on the flanges. For the first test four LVDT's were installed to measure the uplift of the specimens, two on the web and two of them on the flanges. After the first test the LVDT number nine was removed so that one of the limited connections for data recording could be used to install a laser device on the top of the wall. Furthermore there are two LVDT's measuring the absolute displacements on the bottom and on the top of the wall. LVDT number seven and twelve are controlling if there is a slip occurring during the test between the load transmission plate and the specimen and between the basement and the strong floor respectively.

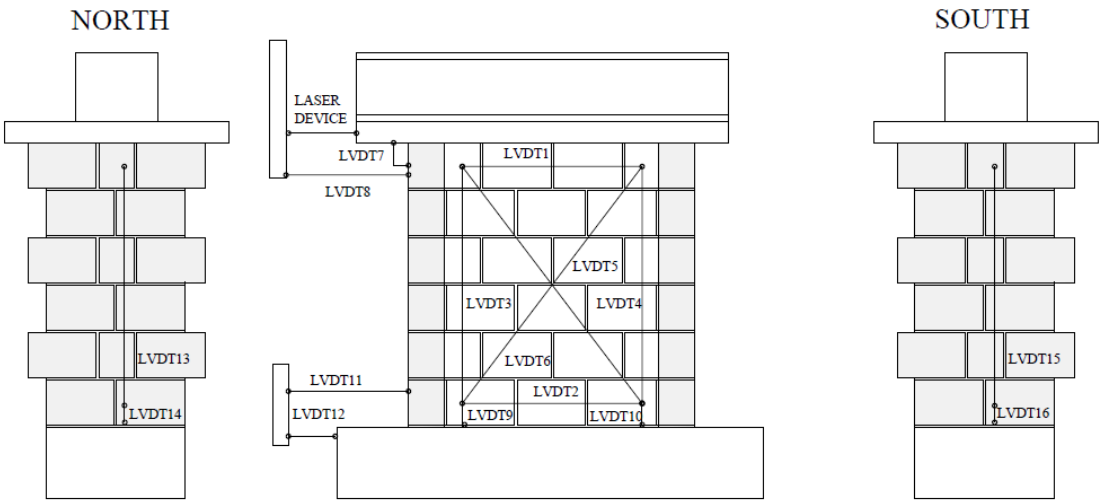

Figure 6.18: Setup LVDT's

With this measuring method an accuracy of 0.3% of the measurement range can be reached. For the tests LVDT's with a measurement span up to 100 mm were used. Therefore the accuracy of the measurements is ±0.3 mm or even more precise for LVDT's with a smaller measurement range.

6.8.2 Digital Image Correlation (DIC)

Masonry has a very complex failure behavior that cannot be sufficiently described by a point-wise measurement of displacements. Digital image correlation (DIC) is a non-interferometric optical measuring technique that allows surface deformation measurement which is more satisfying in describing the behavior of a masonry wall under lateral load. Because DIC is a non-contact optical method it provides not just full-field displacements and strains but also further advantages, namely no risk of damage during the test by fragments falling down when the wall gets heavily damaged and low requirements of measurement environment. (Pan, Qian, Xie, & Asundi, 2009)

The general principle of DIC is to compare digital images of the specimen surface in different loading states (Pan, Qian, Xie, & Asundi, 2009). In our case a 2D DIC method is used that requires a planar surface of the specimen and only in-plane movements are

measured being completely sufficient for our purpose. The instrumentation is schematically shown in Figure 6.19. The camera was placed in a 90 degree angle to the web of the wall specimen at a distance of 3.13 m. The type of camera installed was a Nikon D800E with an AF-S NIKKOR 50 mm 1:1.4 G lens. Two professional flashlights, i.e. Elinchrom Style RX 1200 , were placed in a way that an aperture of approximately 5.6 on the whole web and flanges can be reached. The exposure was chosen with a shutter speed of 1/250 seconds.

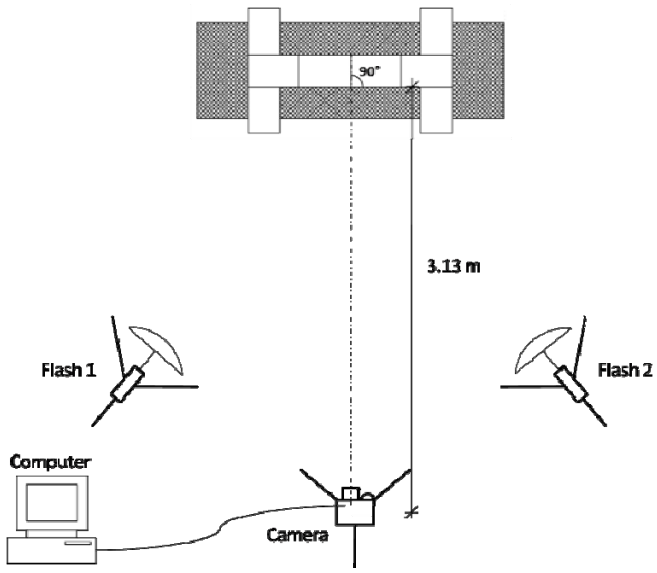

Figure 6.19: Instrumentation DIC

With a camera and two flashes only low measurement equipment is needed. To achieve a systematic shooting process of the specimens and for reasons of convenience a program code written by A. Salmanpour could be used to control the trigger of the camera during the tests. Therefore an additional connection between the camera and the computer of the test setup was needed. With this technique approximately 400-500 pictures are taken during one test.

The applied speckle pattern on the web and on the flanges can be seen in Figure 6.20. A random distribution of the dots was used with a coverage of 40%. The choice of the diameter of the dots primarily depends on the resolution of the images and the distance between the surface and the camera. For the setup shown in Figure 6.19 a diameter of 2 mm was chosen for the dots. To apply the speckle pattern on the surface of the wall a self-adhesive foil printed by a cutting plotter was used. The foil was stuck to the white painted wall specimens and the black color was applied using paint brush technique. The results can be seen in Figure 6.20.

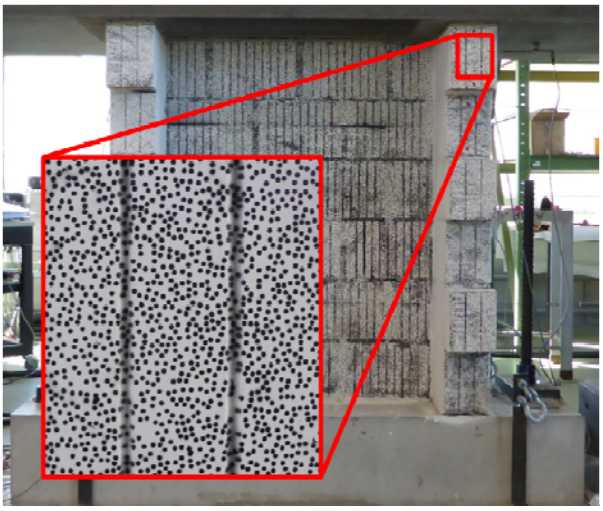

Figure 6.20: Speckle pattern on wall specimen I-0.10

There were some problems applying the speckle pattern properly in the joints so that they had to be partially refinished by hand.

6.9 Results

A brief overview of the observed results is presented in Table 6.8. More detailed results about each test are given in the following sub-chapters. After the separate presentation of the results they are discussed and compared in the following chapters.

Specimen	Applied precom-pression σ_v [MPa]	Shear strength V_{max} [kN]	Deformation capacity d_u/h [%]	Failure mode
I-0.10	1.0	91.9	0.89	Diagonal tension
I-G3.10	0.6	56.6	2.51	Toe crushing
I-G3.15	var	101.3	1.24	Diagonal tension
I-G10.10	0.6	50.4	3.34	Toe crushing / Sliding
I-G10.15	0.9	71.1	2.50	Diagonal tension

Table 6.8: Results I-shaped URM walls

During the first test of specimen I-0.10 some problems were discovered which have mainly been solved in the further tests. In addition it has to be mentioned that specimen I-G3.15 had been tested under wrong boundary condition due to a manipulation failure in the test preparation. This problem is discussed more detailed in chapter 6.9.3.

6.9.1 Specimen I-0.10

At first is has to be mentioned that the specimen I-0.10, built on the 12th of December 2013, suffered from bad workmanship. As a consequence the other specimen where built by a different manufacturer on the 22nd of January. The Specimen I-0.10 was tested on the 24th of April 2014. The ultimate failure occurred in the first pushing cycle of

displacement amplitude step 11, after amplitude step 10 was skipped. The displacement and lateral force time history can be seen in Figure 6.21. The maximum force achived is marked with a red dot.

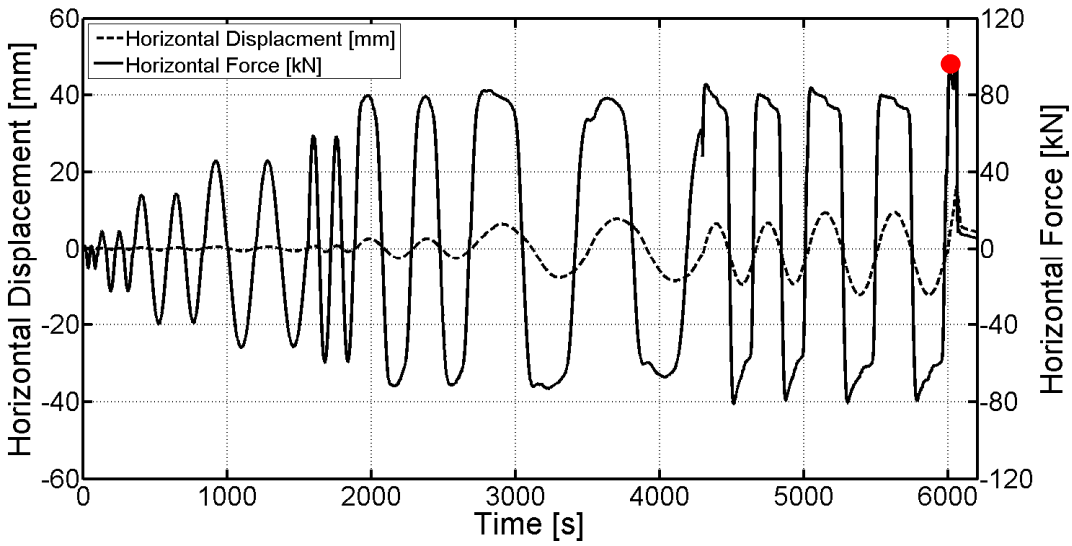

Figure 6.21: Horizontal displacement and horizontal force time history I-0.10

When comparing the conducted horizontal displacements in Figure 6.21 with the ones in the horizontal displacement pattern of Table 6.7 a difference of almost factor two can be recognized. The reason for this deviation from the target value can be found in the geometrical arrangement of the test setup. Since the vertical hydraulic actuators have a defined length and zero-position the horizontal hydraulic actuator has to induce the lateral displacement at almost double the height of the top of the wall. Since the lateral stiffness of the wall is changing during the tests and the presence of various construction components influencing the horizontal displacement induced by the horizontal cylinder this problem could not be solved by simply multiplying the displacement of the horizontal cylinder. Therefore a laser device was installed. This device allows a direct and precise control of the horizontal displacement of the load transmission plate on the top of the wall.

Furthermore after a calibration test of the vertical load cells during the replacement of the first specimen a calibration failure was detected. It turned out that the applied vertical force was 1.69 times the target value. The specimen was therefore tested under a vertical precompression of 1.0 MPa. Due to this change in the precompression level the prediction for the lateral strength and governing failure mode was updated in Table 6.8.

Due to the facts and problems mentioned above the following results of this test have to be handled with particular caution.

6.9.1.1 Force-Displacement Response

The specimen was tested up to an amplitude of 12 mm (measured with LVDT number 8) The maximum lateral force of 91.9 kN was reached in the first cycle of amplitude step 11 (cylinder controlled) in the pushing direction. The hysteresis loops and the corresponding capacity curve are shown in Figure 6.22.

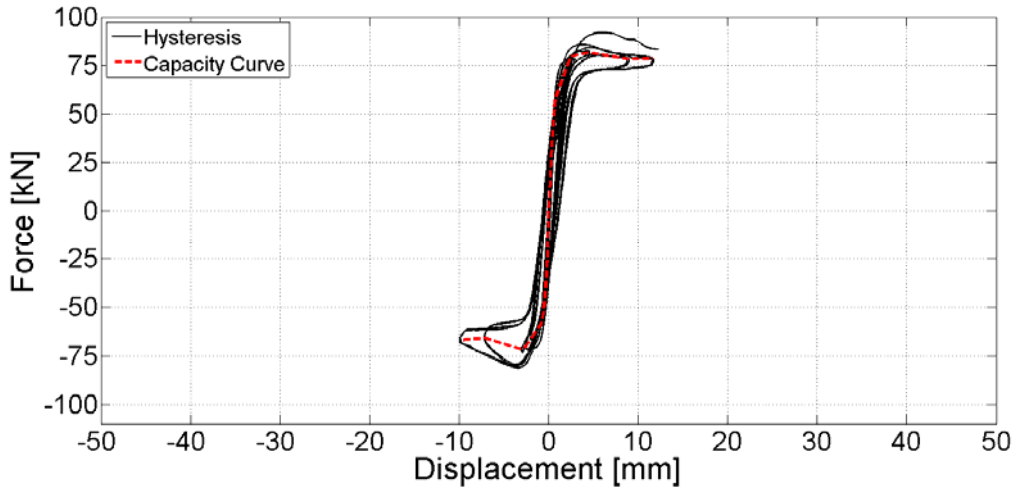

Figure 6.22: Hysteresis loops and capacity curve I-0.10

The hysteresis shows very narrow loops and a S-shape typical for rocking behavior. The uplift of the flanges can be seen in Figure 6.23. Since the uplift was not concentrated to the interface joint as observed in the tests of the specimens with a soft-layer applied the data of LVDT 14 and 16 does not represent the rocking behavior accurately. This fact can be explained having a look at the opening of the horizontal cracks in the photo of the southern flange in Figure 6.23 on the right.

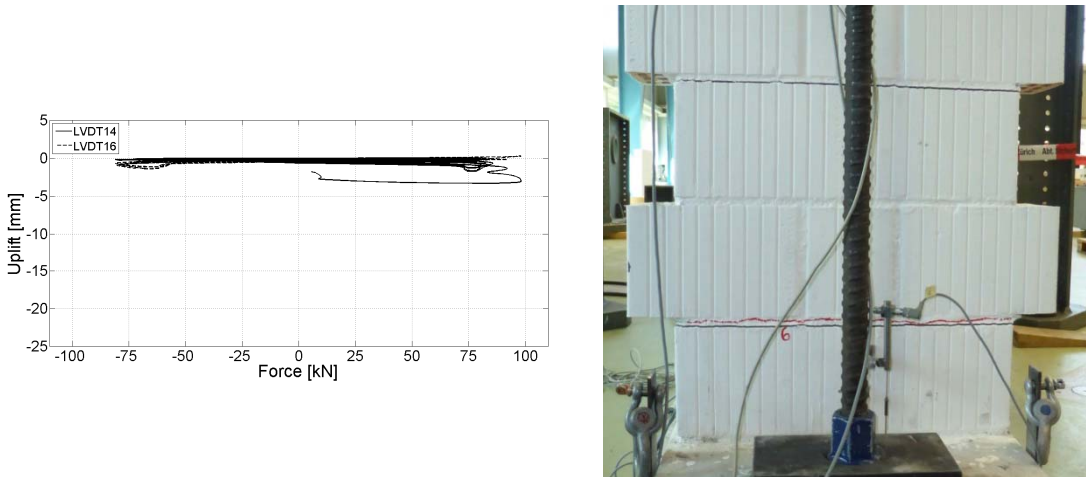

Figure 6.23: (l) I-010 LVDT 14 (uplift flange north) and LVDT 16 (uplift flange south), (r) cracks flange south

The capacity curve and its bilinear idealization according to Tomaževič (1999) are shown in Figure 6.24.

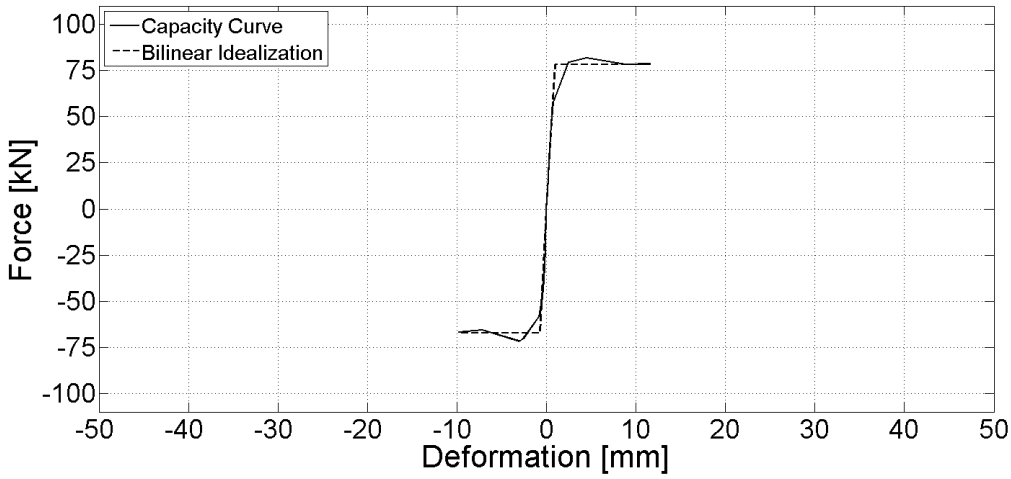

Figure 6.24: Capacity curve and bilinear idealization I-0.10

All characteristic values of the capacity curve and its bilinear idealization are summarized in Table 6.9.

I-0.10	**K_0 [kN/mm]**	**K_{eff} [kN/mm]**	**K_{eff}/K_0 [%]**	**V_{max} [kN]**	**V_u [kN]**	**d_u/h_w [%]**	**d_u [mm]**	**d_y [mm]**	**μ [-]**
Pushing	86.80	78.05	89.92	91.93	78.24	0.96	11.57	1.00	11.54
Pulling	126.90	97.02	76.45	81.01	67.42	0.82	9.86	0.69	14.20

Table 6.9: Results I-0.10

6.9.1.2 Crack Pattern and Failure Mode

After an initial rocking behavior the specimen failed in diagonal tension. Figure 6.25 shows the crack pattern after the first pushing cycle of amplitude step 11 when also the maximum lateral force was observed.

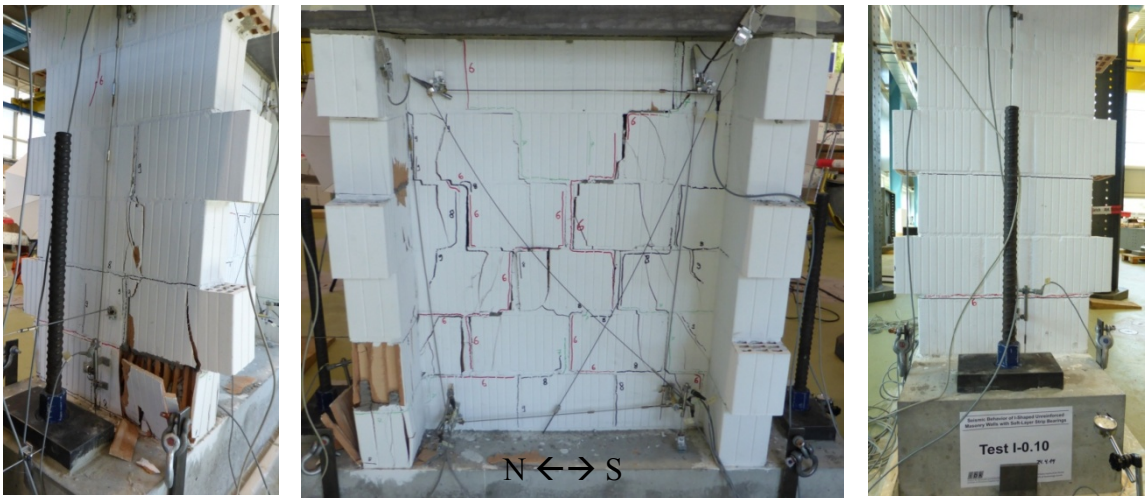

Figure 6.25: Final crack pattern I-0.10

The propagation of the crack pattern is shown in a series of photos in appendix D. Having a look at the final crack pattern of Figure 6.25 the failure mode diagonal tension can

clearly be recognized on the web where distinct diagonal cracks are visible following mainly the head- and bed-joints. But there are also some cracks passing through the bricks. There is no sliding of the bottom edge bricks of the web and the flange-web intersection stays almost perfectly intact.

Having a look at the crack pattern on the flanges it can be seen that there are very few cracks. Only the flange on the north exhibits some vertical cracks concentrated in the middle and lower part of the flange.

6.9.1.3 Energy Dissipation

The dissipated energy during the test is visualized in Figure 6.26. On the left side of figure the energy dissipation is represented by means of the dissipated energy ratio while on the right side the energy dissipation is represented by the damping ratio.

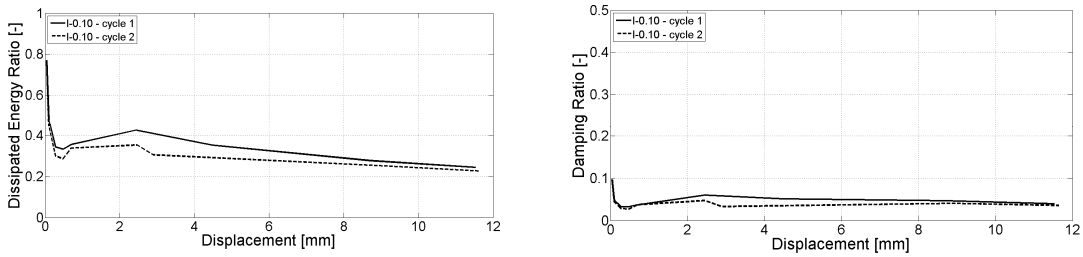

Figure 6.26: I-0.10:(l) Dissipated energy ratio, (r) Damping ratio

According to both characteristic ratios the energy dissipation is very high at the beginning. This can be explained by the shape of the first cycle that is almost rectangular. From a displacement of 0.5 mm the ratios do not change much. Both ratios reach their limit at a displacement of about 2.5 mm. The dissipated energy ratio for the first cycle at this point is equal to 0.43 and 0.06 for the damping ratio respectively. There is no big difference in the energy dissipation between the first and the second cycle observed whereat the energy dissipation in the second cycle is lower over the whole range. This can be explained by the observation that most of the additional damage in a higher displacement amplitude step occurs in the first cycle. And there is a close connection between damage and energy dissipation because a lot of energy is dissipated due to the propagation of cracks and friction.

6.9.2 Specimen I-G3.10

The specimen I-G3.10 was built on the 22nd of January 2014 and tested on the 5th of Mai 2014. The ultimate failure occurred at the end of the second cycle of displacement amplitude step 10 which induces a maximum lateral displacement of 30 mm. This time the target displacements could be reached exactly by using the laser device to control the horizontal displacement of the top of the wall as also can be seen in Figure 6.27. The maximum force of 56.6 kN that was reached during the test is marked with a red dot in Figure 6.27.

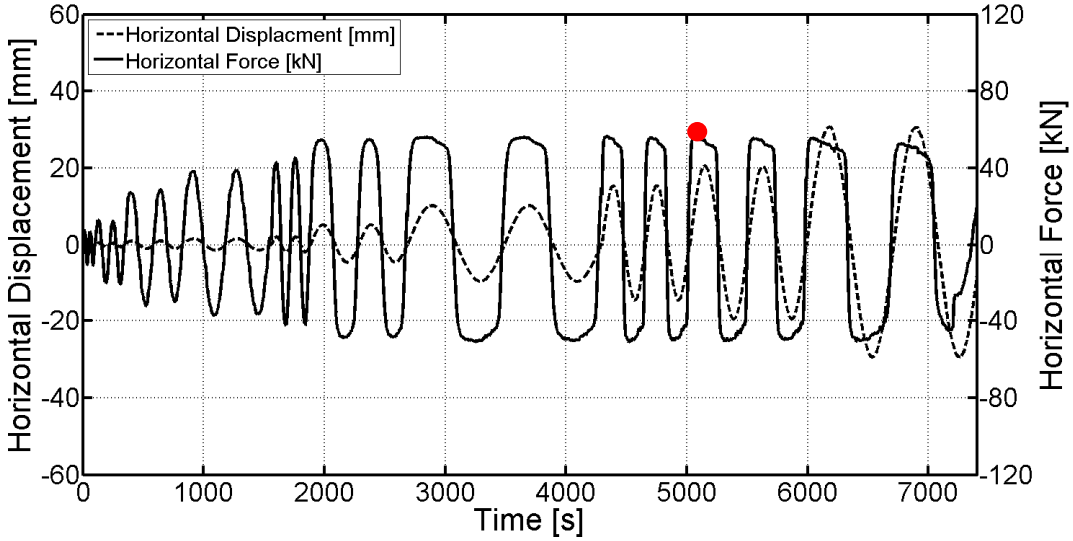

Figure 6.27: Horizontal displacement and horizontal force history I-G3.10

6.9.2.1 Force-Displacement Response

The Specimen was tested up to an amplitude of 30 mm. The maximum lateral force of 56.6 kN was reached in the first pushing cycle of amplitude step 9 at a displacement of 20mm. The hysteresis loops and the corresponding capacity curve are shown in Figure 6.28.

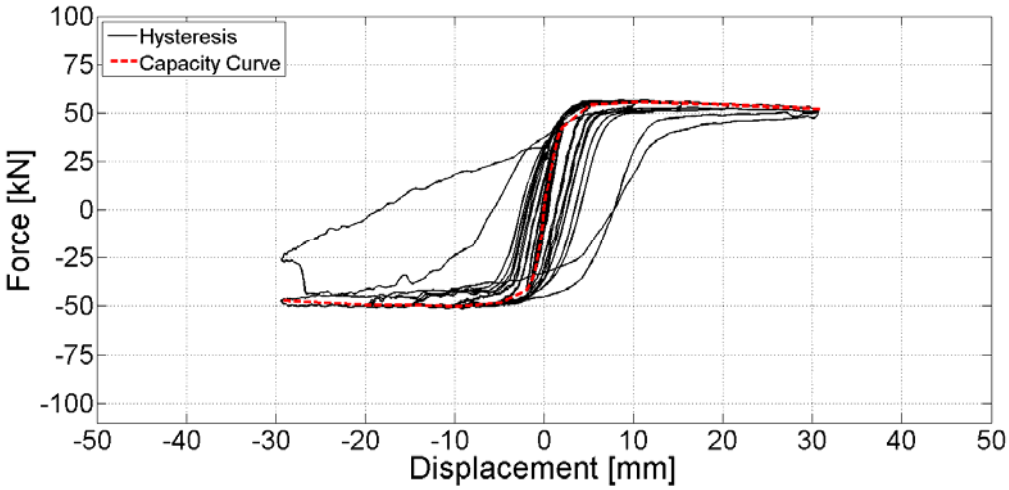

Figure 6.28: Hysteresis loops and capacity curve I-G3.10

The hysteresis shows quite narrow loops until the last two cycles of displacement amplitude step 10 (30 mm) and a clear S-shape with a distinct plateau due to the rocking behavior. The uplift at the flanges is shown in Figure 6.29.

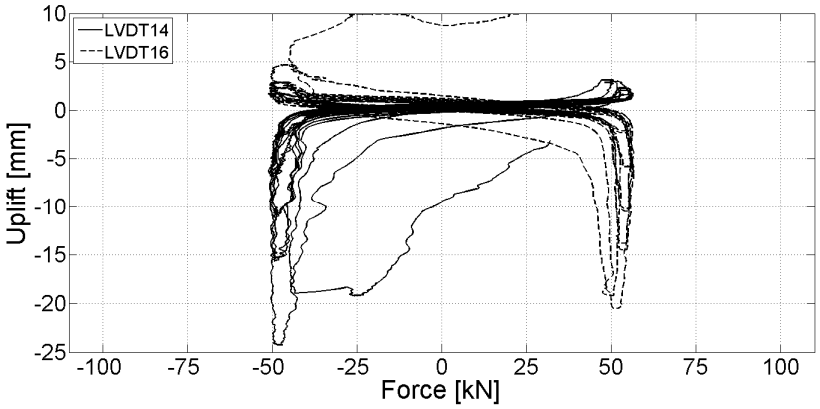

Figure 6.29: I-G3.10: LVDT 14 uplift flange north, LVDT 16 uplift flange south

The capacity curve and its bilinear idealization according to Tomaževič (1999) are shown in Figure 6.30.

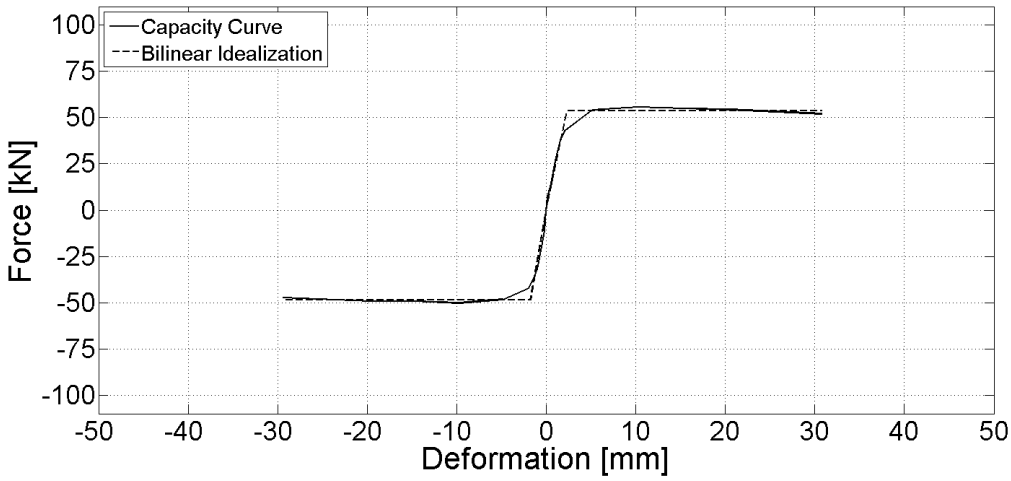

Figure 6.30: Capacity curve and bilinear idealization I-G3.10

All characteristic values of the capacity curve and its bilinear idealization are summarized in Table 6.10.

I-G3.10	**K_0 [kN/mm]**	**K_{eff} [kN/mm]**	**K_{eff}/K_0 [%]**	**V_{max} [kN]**	**V_u [kN]**	**d_u/h_w [%]**	**d_u [mm]**	**d_y [mm]**	**μ [-]**
Pushing	38.23	23.07	60.35	56.61	53.76	2.56	30.77	2.33	13.20
Pulling	55.08	27.67	50.24	51.06	48.65	2.45	29.44	1.76	16.74

Table 6.10:Results I-G3.10

6.9.2.2 Crack Pattern and Failure Mode

After an initial rocking behavior the ultimate failure mode was observed to be toe crushing. The crack pattern at the end of the test after the second cycle of displacement amplitude step 10 (30mm) is shown in Figure 6.31.

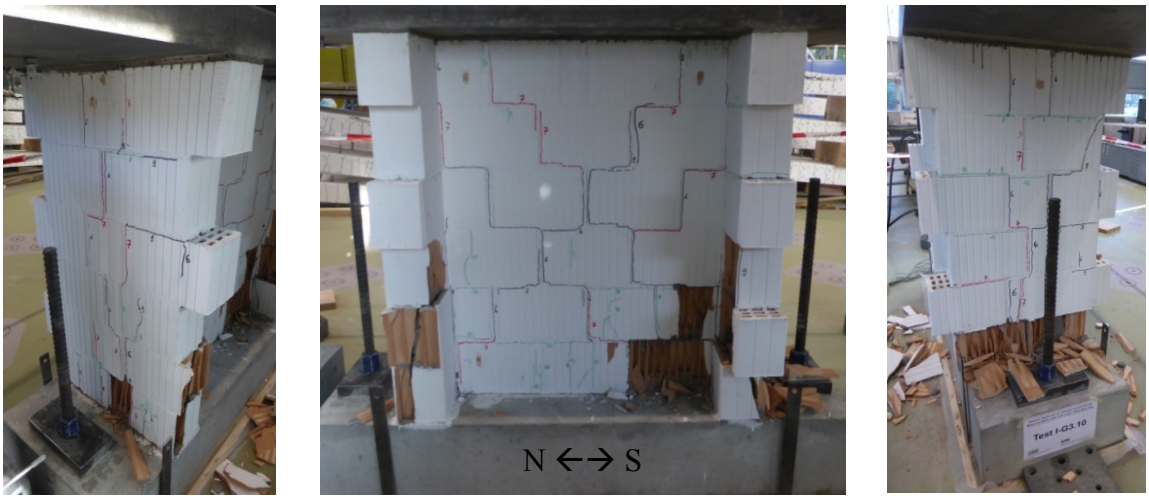

Figure 6.31: Final crack pattern I-G3.10

The propagation of the crack pattern is shown in a series of photos in appendix D. Having a look at the final crack pattern of Figure 6.31 the toe crushing is clearly visible especially at the southern flange where the lowest row of bricks was completely destroyed. Also the web suffered more damage in the pulling direction.

Having a look at the crack pattern at the flange-web intersection it can be seen that there are a lot of vertical cracks concentrated in the middle of the flanges. This may be a sign for a lack in force transmission from the web to the flanges.

When analyzing the crack pattern of the flanges a clear split of both flanges on both sides attracts attention as can be seen in the photos of Figure 6.32. This fact is discussed more in detail in chapter 9.4.

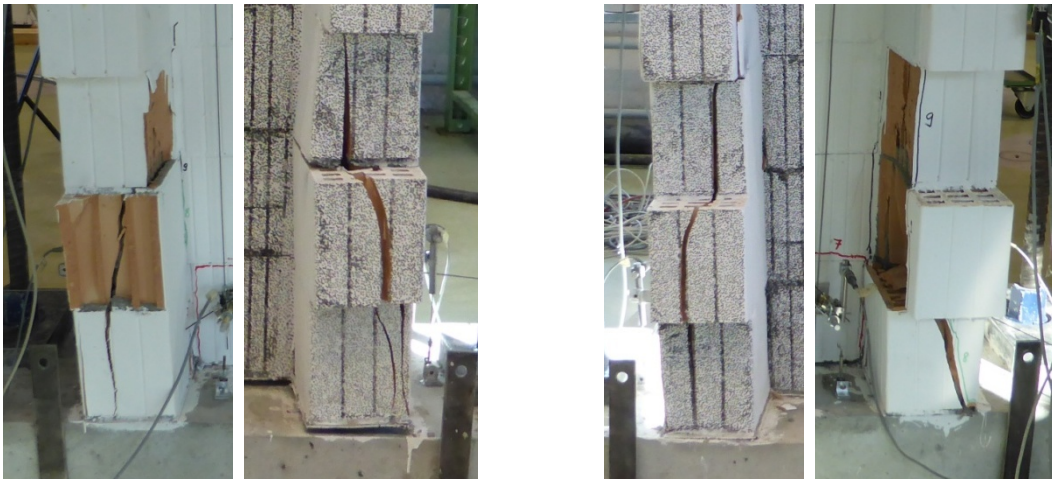

Figure 6.32: Splitting of the flanges I-G3.10: (l) Flange north, (r) Flange south

6.9.2.3 Energy Dissipation

The dissipated energy ratio and the damping ratio are plotted in Figure 6.33. Both values do not change much during the test. The dissipated energy ratio as well as the damping ratio reaches its first peak of 0.64 and 0.06 respectively for the first cycle at a

displacement of 5 mm. After this peak both values are slightly falling until there is another rise in the last cycle where significantly more energy is dissipated. This is also clearly visible in the hysteresis loops shown in Figure 6.28.

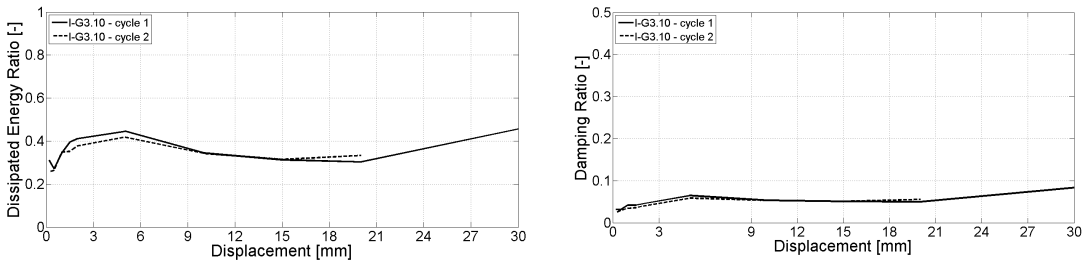

Figure 6.33: I-G3.10: (l) Dissipated energy ratio, (r) Damping ratio

6.9.2.4 Damage SLS Bearing

The 3mm granulate SLS bearing stayed almost perfectly intact during the test as can be seen in Figure 6.34.

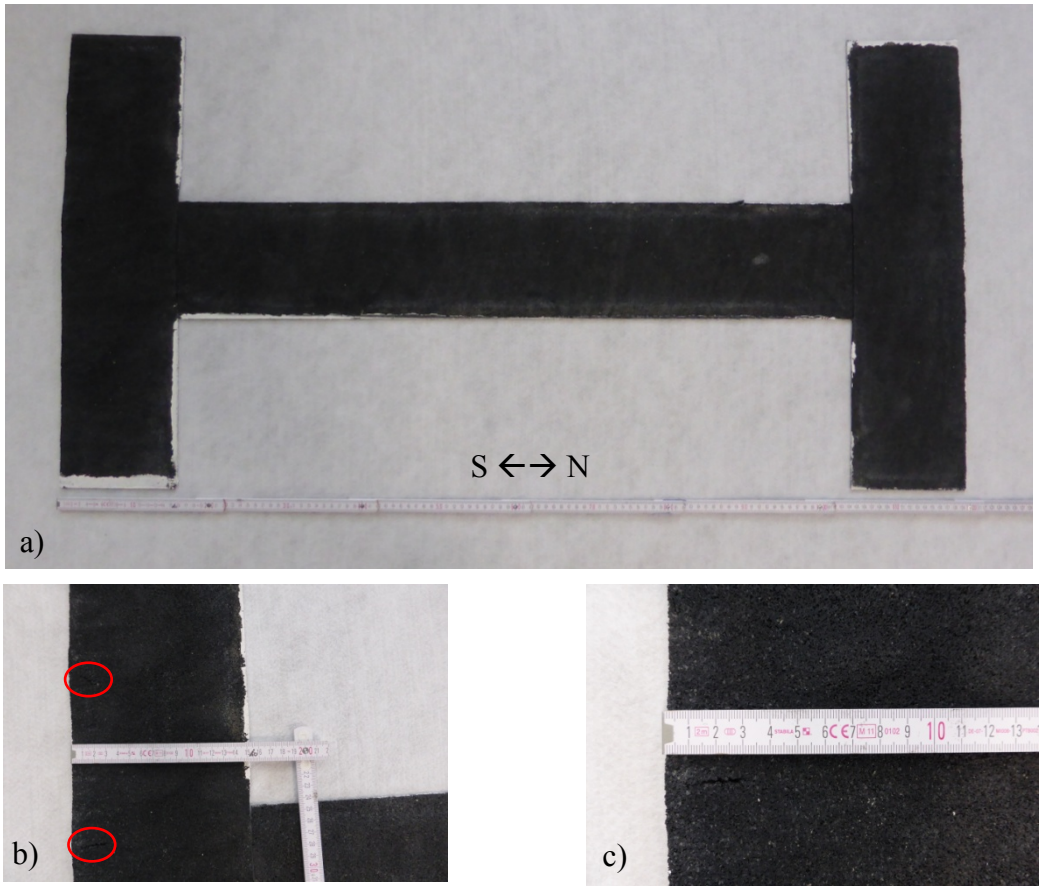

Figure 6.34: (a) Damage SLS bearing I-G3.10, (b) Flange south, (c) Detail flange south

There are only two little scratches on the southern flange with a length of about 2 cm. One of them was found at the end of the web and the other one in a distance of approximately 20 cm to the center of the web.

6.9.3 Specimen I-G3.15

The specimen I-G3.15 was built on the 22nd of January 2014 and was tested on the 15th of May 2014 after a brake in the testing series of the I-shaped specimens. During this brake the test setup was used to conduct some tests about hybrid testing and the control settings were partially changed. Since this changes were not recognized before the start of test I-G3.15 this leads to two failures in the test controlling in the first few cycles. As can be seen in the horizontal force history of Figure 6.35 there was an offset of 16.8 kN in the horizontal force in the first three cycles. This was caused by a failure in the controlling of the vertical hydraulic actuator on the north that accidentally applied no vertical load. This was corrected before starting the forth cycle. In the horizontal displacement history of figure Figure 6.35 it also can be seen that the sixth cycle was repeated. This has been done because up to this cycle the horizontal displacements were controlled by the horizontal actuator and therefore the induced displacements on the top of the wall were too small. Since this mistakes happened at displacements up to 2 mm or less they are not supposed to have significant influence on the maximum force or failure mode of the specimen.

Unfortunately another mistake happened that had significant influence on the results. The test setup is equipped with four safety steel bars preventing the loading beam to move downwards when the hydraulics are turned off. Before each test they have to be loosened. Regrettably this was forgotten this time. To avoid such failures in future tests the check list in appendix G was prepared. Nevertheless the results are presented hereinafter. The influence of the modified boundary condition caused by the safety steel bars is discussed in chapter 8.

The ultimate failure occurred in the first pushing cycle of displacement amplitude step 10 which induces a maximum lateral displacement of 30 mm. The maximum force of 101.34 kN that was reached during the test is marked with a red dot in Figure 6.35.

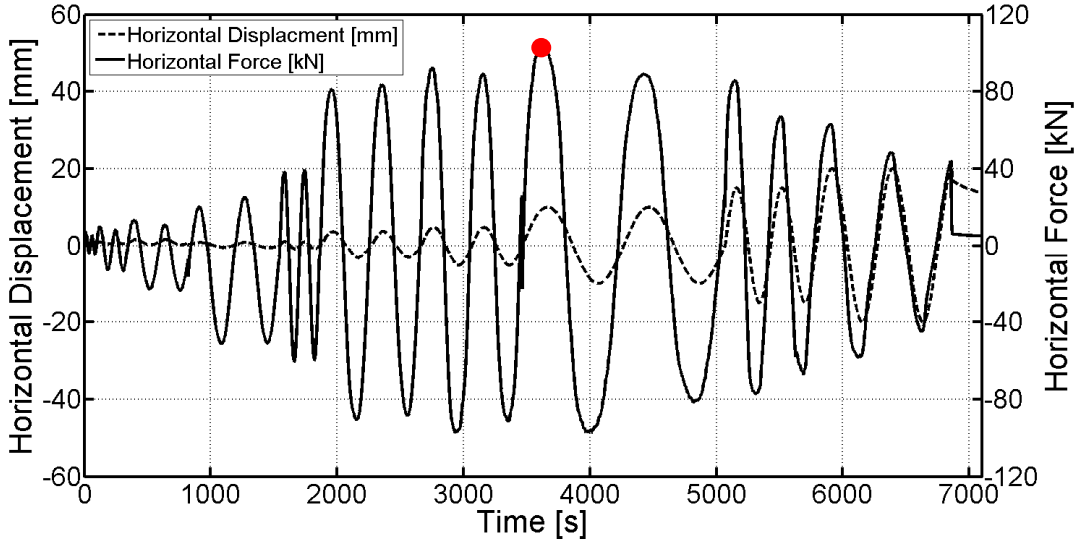

Figure 6.35: Horizontal displacement and horizontal force history I-G3.15

6.9.3.1 Force-Displacement Response

The specimen was tested up to a displacement amplitude of 20 mm. The maximum lateral force of 101.34 kN was reached in the first pushing cycle of amplitude step 7 at a displacement of 10 mm. The hysteresis loops and the corresponding capacity curve are shown in Figure 6.36.

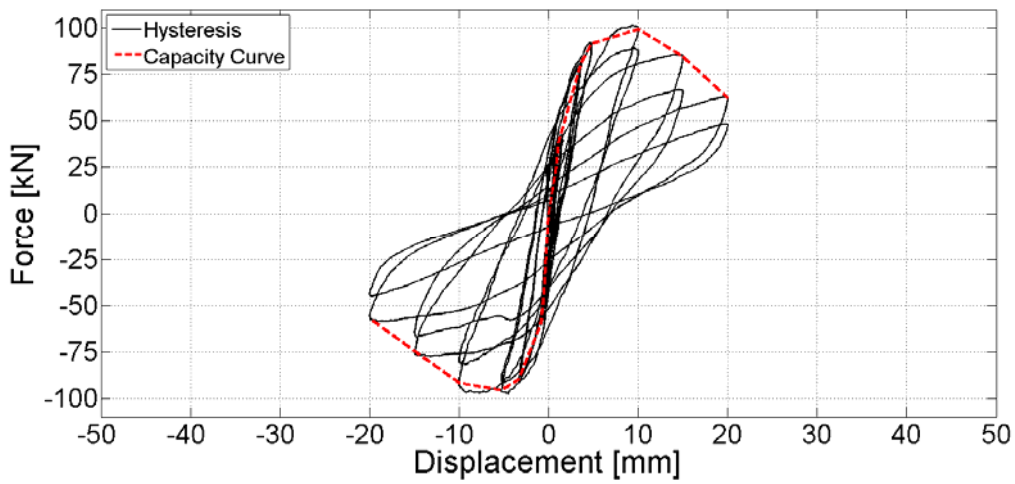

Figure 6.36: Hysteresis loops and capacity curve I-G3.15

The hysteresis shows a distinct strength degradation after the maximum force was reached. Since no rocking was observed as can be seen in Figure 6.37 the hysteresis loops formed no S-shape. Instead the single loops exhibit clear peaks of maximum force and displacement.

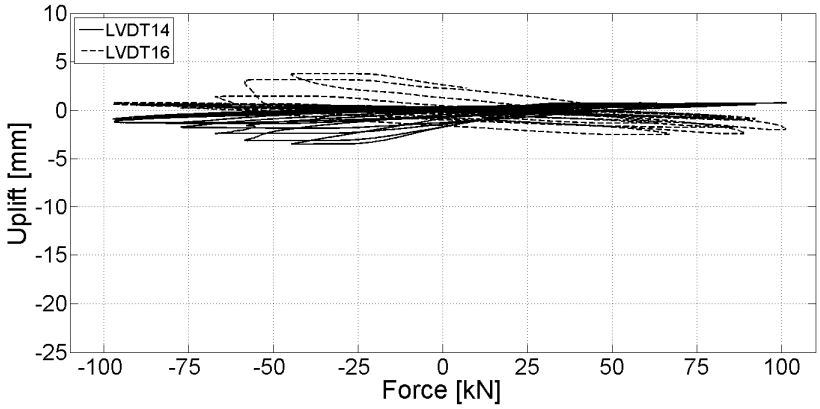

Figure 6.37: I-G3.15: LVDT 14 uplift flange north, LVDT 16 uplift flange south

The capacity curve and its bilinear idealization according to Tomaževič (1999) are shown in Figure 6.38.

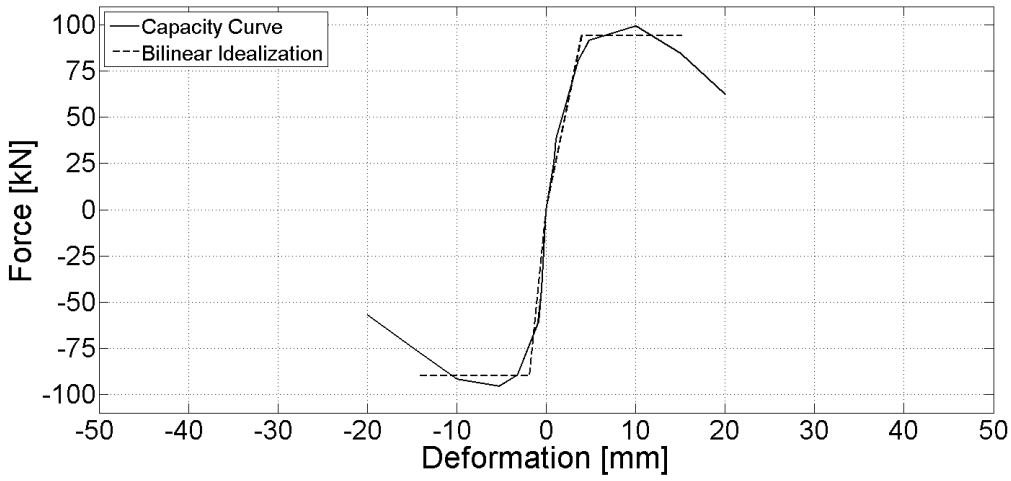

Figure 6.38: Capacity curve and bilinear idealization I-G3.15

All characteristic values of the capacity curve and its bilinear idealization are summarized in Table 6.10.

I-G3.15	K_0 [kN/mm]	K_{eff} [kN/mm]	K_{eff}/K_0 [%]	V_{max} [kN]	V_u [kN]	d_u/h_w [%]	d_u [mm]	d_y [mm]	μ [-]
Pushing	35.33	23.83	67.44	101.34	94.33	1.27	15.19	3.96	3.84
Pulling	88.08	47.57	54.01	97.36	89.80	1.21	14.46	1.89	7.66

Table 6.11:Results I-G3.15

6.9.3.2 Crack Pattern and Failure Mode

Specimen I-G3.15 showed no initial rocking behavior. The ultimate failure mode was observed to be diagonal tension. The final crack pattern at the end of the test at the end of the second pulling cycle of displacement amplitude step 9 (20 mm) is shown in Figure 6.39.

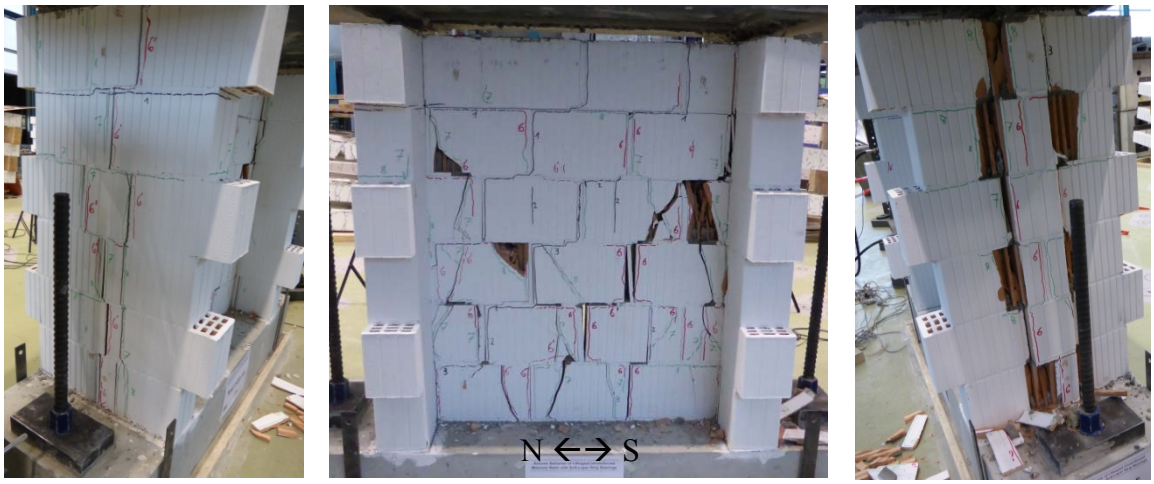

Figure 6.39: Final crack pattern I-G3.15

The propagation of the crack pattern is shown in a series of photos in appendix D. Having a look at the final crack pattern of Figure 6.39 quite a lot of diagonal cracks are visible on the web. The diagonal crack of the web that opened in the end due to the diagonal tension failure can be seen clearly. In some parts the crack follows the head- and bed-joints and there are other parts where it propagates through the bricks which is typical for shear failures at relatively high precompression. The direction of the diagonal crack from the southern top to the northern bottom indicates that the final failure occurred in the pushing direction.

Having a look at the crack pattern at the flange-web intersection there are a lot of cracks concentrated in the middle of the flanges. At the intersection on the south where the flange punched completely through the web the cracks follow the head-joints and in every second course pass through the bricks. This intersection failed in the first pulling cycle of load amplitude step 7. The propagation of the cracks on the flange-web intersection on the southern flange can be seen in Figure 6.40. The intersection on the north is also highly damaged but the web did not punch through the flange even so the intersection seems to be fully cracked, at least on the west side of the flange.

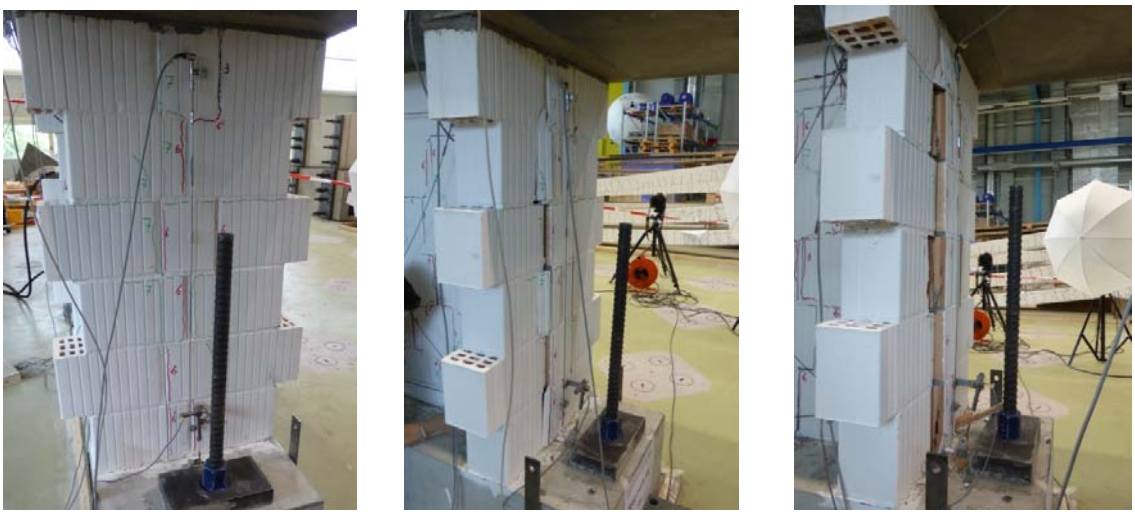

Figure 6.40: Failure of flange-web intersection I-G3.15

When looking at the southern flange the main damage is caused by the web punching through the flange. The rest of the southern flange is almost undamaged. Pretty much the same is observed on the northern flange but the web did no completely punch through the flange on this side. Additional to the concentrated cracks in the middle of the flange there is a horizontal crack in the bed-joint right below the top course which was caused during the first displacement amplitude step when no vertical force was applied on this side of the wall. No splitting of the flanges was observed in this test.

6.9.3.3 Energy Dissipation

The dissipated energy ratio and the damping ratio are plotted in Figure 6.49. Since the displacement on the top of the wall did not reach the target displacements up to an amplitude of 2 mm and no vertical force was applied on the northern end of the wall in the first 3 cycles the energy dissipation was first calculated in the 4th cycle. The energy dissipation before this cycle would not be comparable to the other tests and because the boundary condition changed by reapplying the vertical force on the north a trend analysis in this early range would not make much sense.

After an almost constant rising the dissipated energy ratio as well as the damping ratio reaches its limit of 0.73 and 0.11 in the first cycle at a displacement of 15 mm. After having reached the peak the dissipated energy ratio stays nearly constant until the end of the test. The damping ratio is slightly falling after the peak and ends up with a value of 0.09 (first cycle) at a displacement of 20 mm. The energy dissipation of the second cycle is generally lower than the one of the first cycle except at the peak for the dissipated energy ratio.

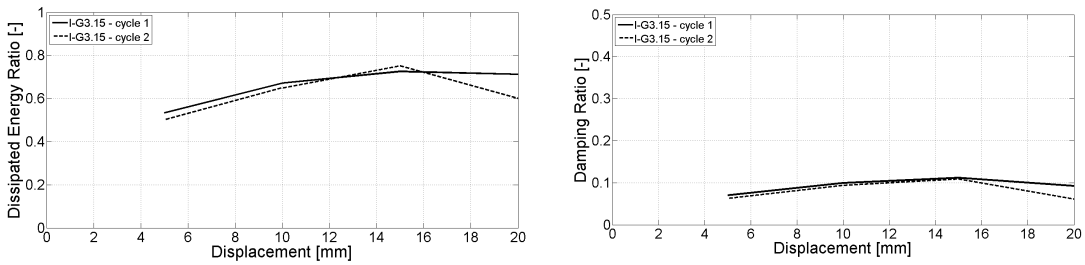

Figure 6.41: I-G3.15: (l) Dissipated energy ratio, (r) Damping ratio

6.9.3.4 Damage SLS Bearing

The 3 mm granulate SLS bearing shows almost no visible damage. Only one single rupture of about 10 cm length was can be seen at a distance of about 40 cm of the north end of the wall (see Figure 6.42 (a)). This rupture was caused by a crack opening in the repetition of load amplitude step 6 (see Figure 6.42 (b)). The rest of the soft-layer stayed perfectly intact.

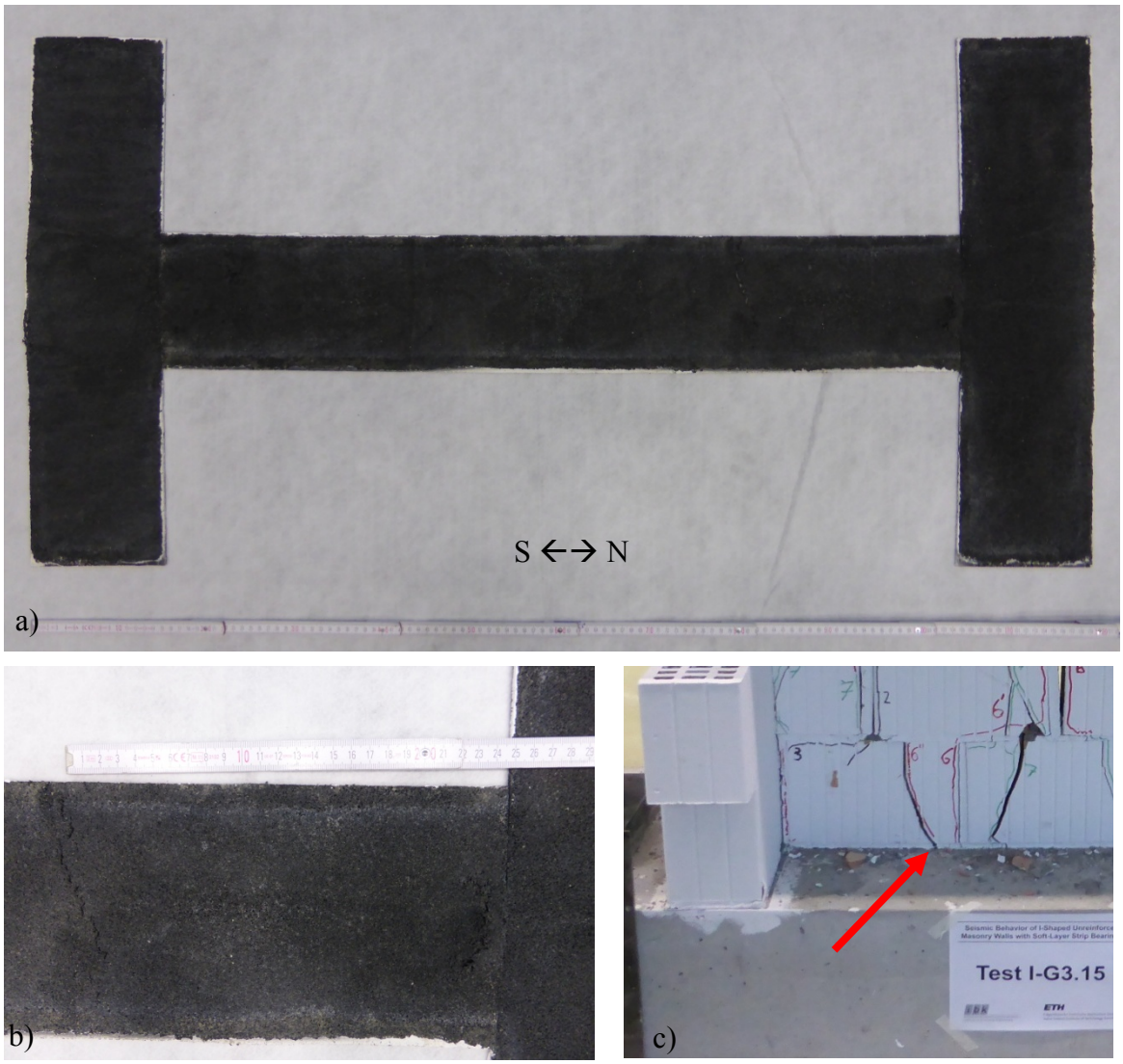

Figure 6.42: (a) Damage SLS bearing I-G3.15, (b) Detail rupture in the web, (c) Crack that caused rupture of detail

6.9.4 Specimen I-G10.10

The specimen I-G10.10, built on the 22th of January 2014, was tested on the 20th of Mai 2014. The ultimate failure occurred in the second pushing cycle of displacement amplitude step 11 which induces a maximum displacement of 40 mm. The displacement and lateral force time history are shown in Figure 6.43. The maximum force that was reached during the test is marked with a red dot.

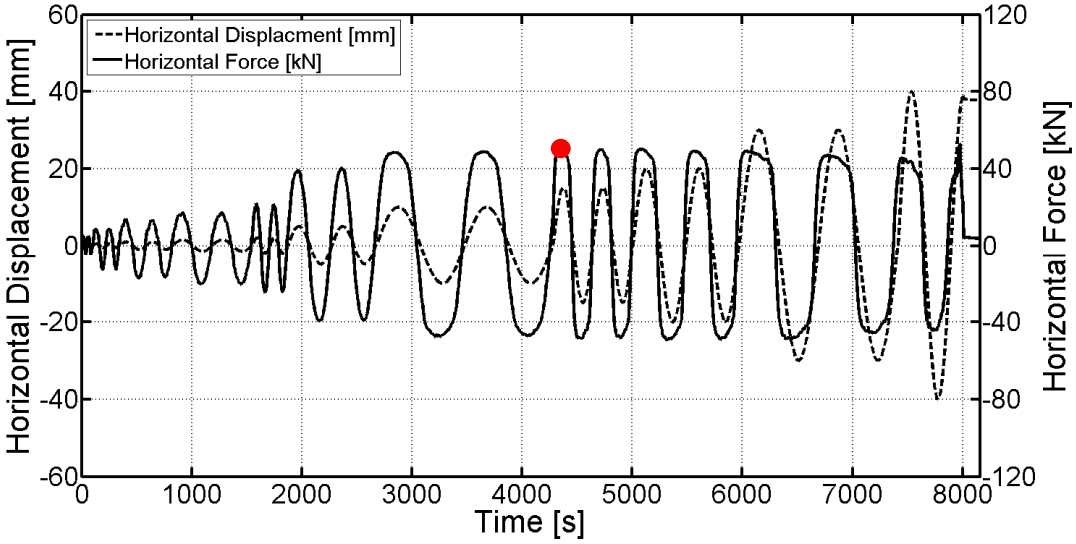

Figure 6.43: Horizontal displacement and horizontal force time history I-G10.10

6.9.4.1 Force-Displacement Response

The test of specimen I-G10.10 was finished at the beginning of the second cycle of amplitude step 11 before the specimen crushed completely. The maximum lateral force of 50.38 kN was reached in the first pushing cycle of amplitude step 8 (15 mm). The hysteresis loops and the corresponding capacity curve are shown in Figure 6.44.

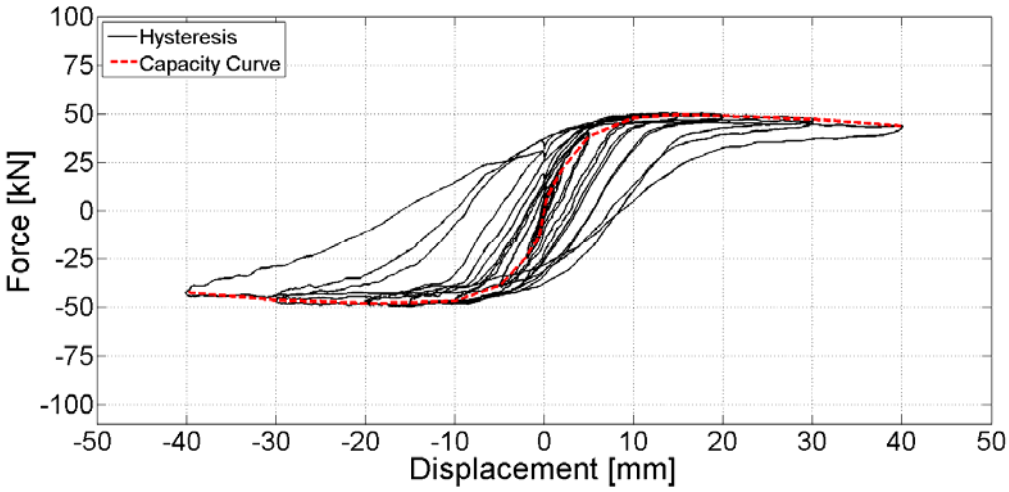

Figure 6.44: Hysteresis loops and capacity curve I-G10.10

The hysteresis shows clear S-shape caused by its pronounced rocking behavior. The resulting distinct plateau at the maximum forces of the cycles is visible in Figure 6.44. The rocking motion is visualized in Figure 6.45. An uplift of more than 2 cm was measured. Almost no strength degradation took place from the yield displacements to the maximum displacements of the cycles.

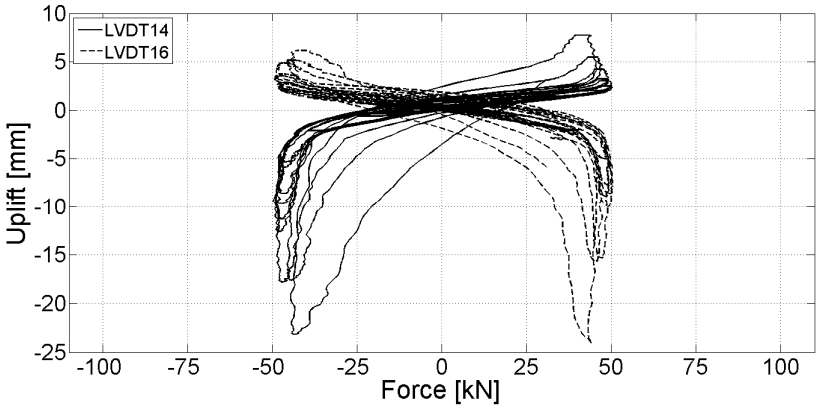

Figure 6.45: I-G10.10: LVDT 14 uplift flange north, LVDT 16 uplift flange south

The capacity curve and its bilinear idealization according to Tomaževič (1999) are shown in Figure 6.46.

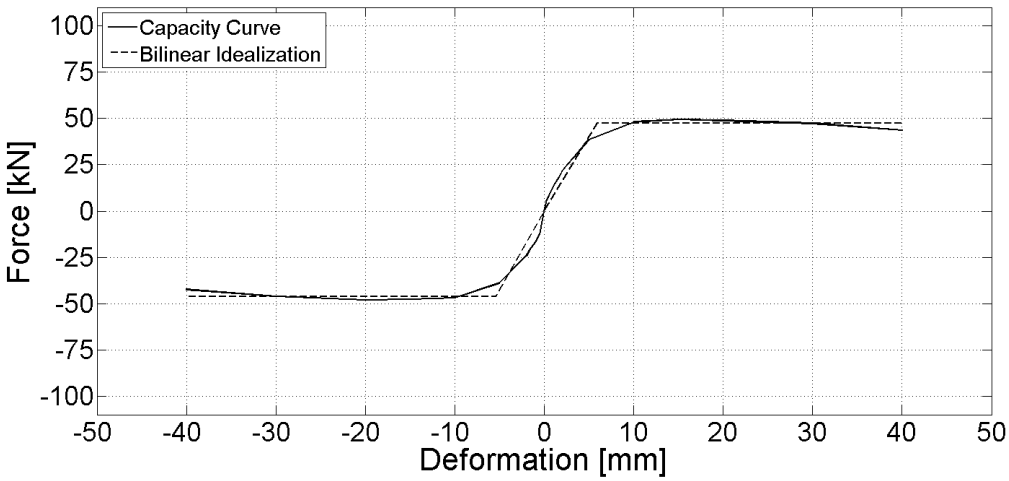

Figure 6.46: Capacity curve and bilinear idealization I-G10.10

All characteristic values of the capacity curve and its bilinear idealization are summarized in Table 6.12.

I-G10.10	**K_0 [kN/mm]**	**K_{eff} [kN/mm]**	**K_{eff}/K_0 [%]**	**V_{max} [kN]**	**V_u [kN]**	**d_u/h_w [%]**	**d_u [mm]**	**d_y [mm]**	**μ [-]**
Pushing	24.56	7.99	32.54	50.38	47.41	3.34	40.03	5.93	6.75
Pulling	23.78	8.56	36.01	49.68	46.40	3.34	40.03	5.42	7.39

Table 6.12:Results I-G10.10

6.9.4.2 Crack Pattern and Failure Mode

After an initial rocking behavior the main ultimate failure mode was observed to be toe crushing. But also some stair stepped sliding occurred in the end as can be seen in Figure 6.47 where the final crack pattern at the end of the test at the beginning of the second pushing cycle of displacement amplitude step 11 (40mm) is shown.

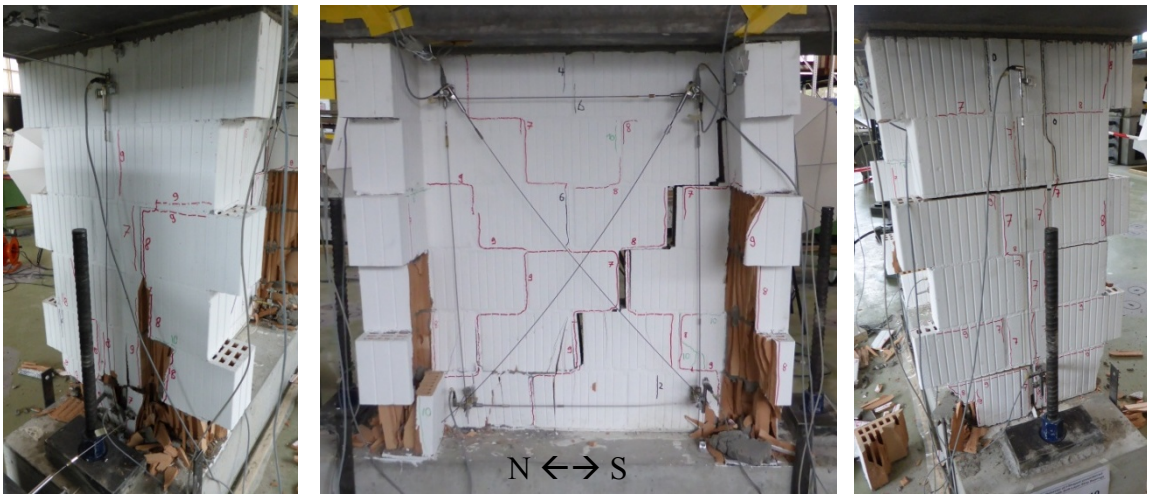

Figure 6.47: Final crack pattern I-G10.10

The propagation of the crack pattern is shown in a series of photos in appendix D. Having a look at the final crack pattern of Figure 6.47 the toe crushing and the sliding failure are clearly visible. On the northern flange that failed in the end the high damage of the lowest row of bricks is clearly visible. When analyzing the crack pattern of the web the diagonal jagged crack following the head- and bed-joints can be seen that indicates the additional sliding failure mode of the specimen. The direction of the diagonal crack approves that the specimen failed in the pushing direction.

Having a look at the crack pattern at the flange-web intersection some cracks concentrated in the middle of the flanges can be seen. But they mainly follow the head-joint and do not propagate through the bricks except of the bottom row on the northern flange where the toe of the wall crashed. No failure of the flange-web intersection could be found.

When looking at the southern flange, beside the vertical cracks in the middle, a distinct horizontal crack through the whole flange is visible and a lateral displacement of the upper part that occurred in the final sliding movement. The northern flange is mainly damaged at the bottom due to the toe crushing failure. Both flanges are highly damaged and split in the lower part as can be seen in Figure 6.48.

Figure 6.48: Splitting of the flanges I-G10.10: (l) Flange north, (r) Flange south

6.9.4.3 Energy Dissipation

The dissipated energy ratio and the damping ratio are plotted in Figure 6.49. The dissipated energy ratio (first cycle) reaches its first peak at a displacement of 5 mm before attaining its maximum of 0.53 at a displacement of 30 mm. The damping ratio is almost constant at a level of 0.05 until it begins to rise at 15 mm displacement and reaches its maximum of 0.10 at 30 mm displacement.

After having reached their maximum both ratios are slightly falling in the end. Comparing the energy dissipation of the first and second cycle it can be seen that from a displacement of about 12 mm the energy dissipation of the second cycle is slightly bigger than the one of the first.

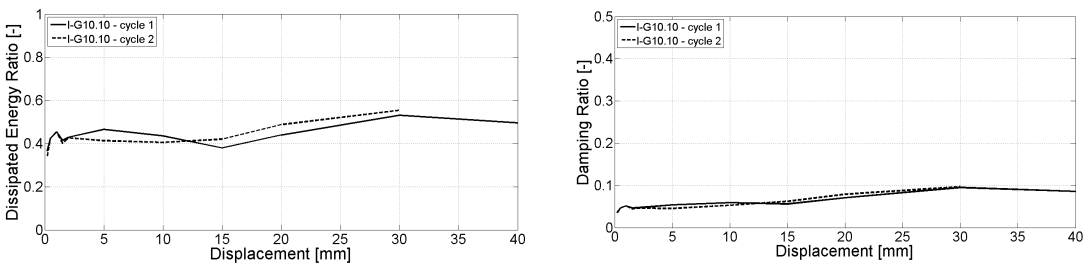

Figure 6.49: I-G10.10: (l) Dissipated energy ratio, (r) Damping ratio

6.9.4.4 Damage SLS Bearing

The 10 mm granulate SLS bearing shows some visible damage especially at the very ends of the web (in the middle of the flanges). The web itself is almost undamaged except of a circular rupture at the south end of the web at the intersection point to the southern flange. The shape of this rupture is rather unusual and after removing the layer from the concrete basement it was found that this rupture happened due to a hole that was drilled into the concrete basement and was not refilled properly.

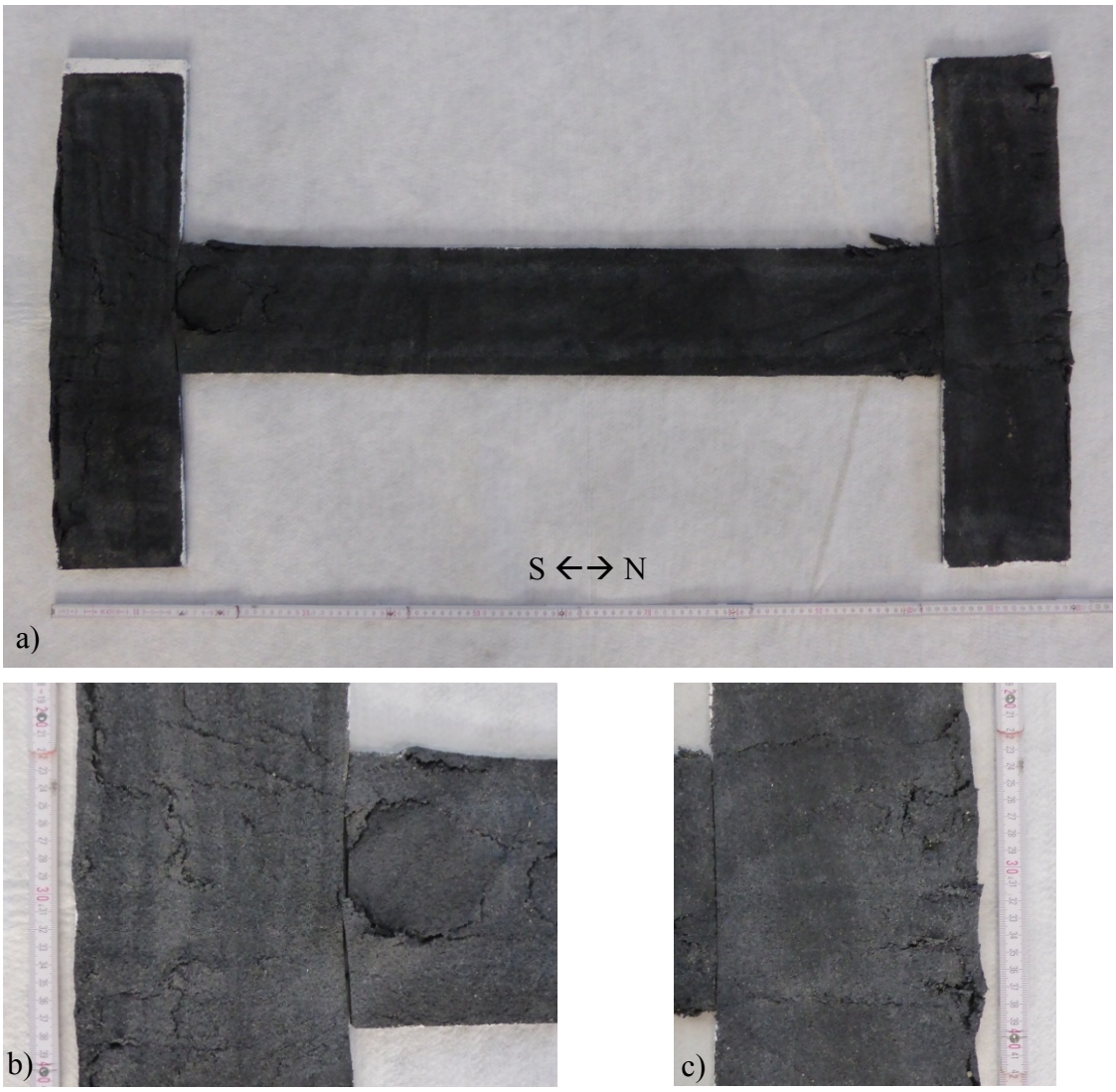

Figure 6.50: (a) Damage SLS bearing I-G10.10: (b) Detail flange south, (c) Detail flange north

6.9.5 Specimen I-G10.15

The specimen I-G10.15 was tested on the 23th of Mai 2014 after having been built on the 22th of January 2014. The ultimate failure occurred in the second pushing cycle of displacement amplitude step 10 which induces a maximum displacement of 30 mm. The displacement and lateral force time history are shown in Figure 6.51. The maximum force that was reached during the test is marked with a red dot.

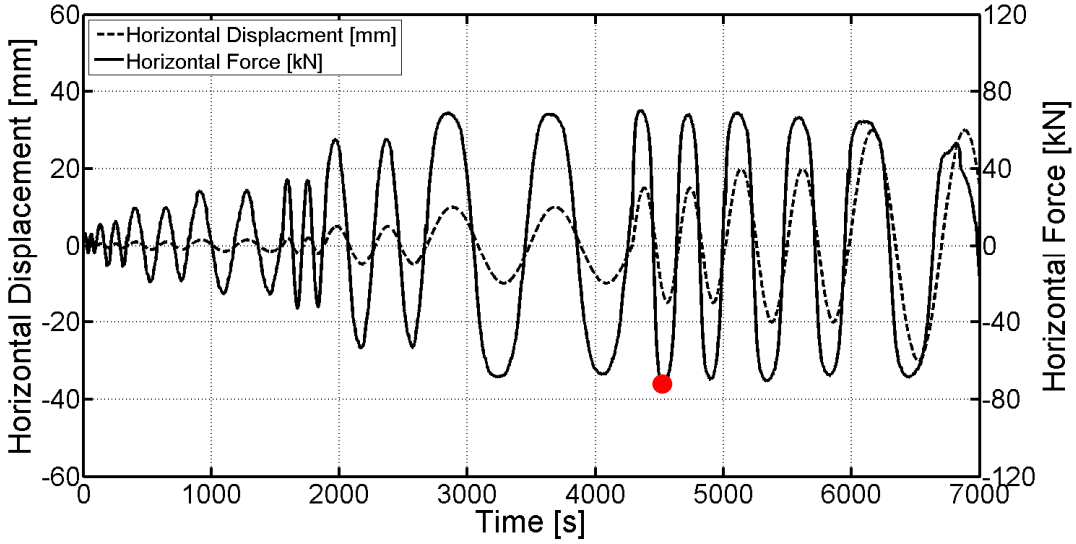

Figure 6.51: Horizontal displacement and horizontal force time history I-G10.15

6.9.5.1 Force-Displacement Response

The test of specimen I-G10.15 was finished at the beginning of the second pulling cycle of amplitude step 10 before the specimen crushed completely. The ultimate failure in diagonal tension happened in the pushing cycle before. The maximum lateral force of 71.11 kN was reached in the first pulling cycle of amplitude step 8 (15 mm). The hysteresis loops and the corresponding capacity curve are shown in Figure 6.52.

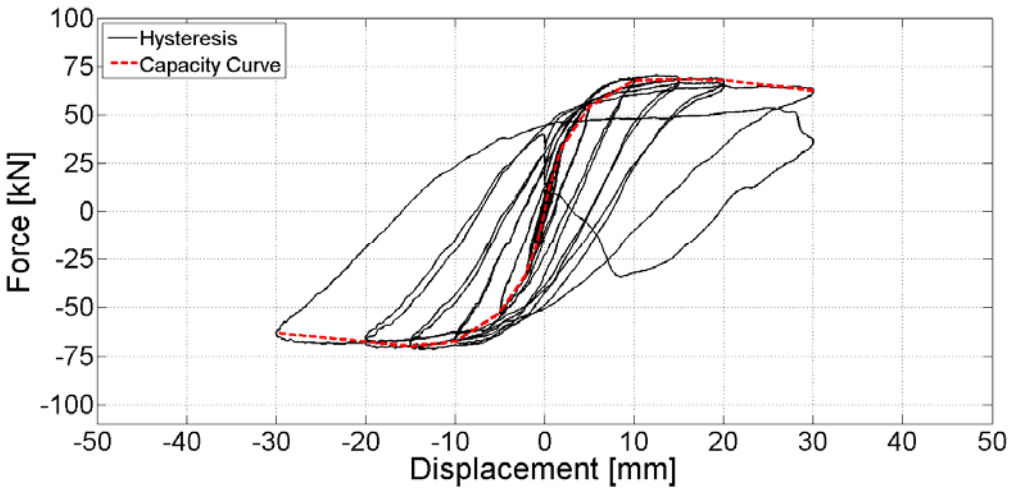

Figure 6.52: Hysteresis loops and capacity curve I-G10.15

The hysteresis shows a S-shape caused by its rocking behavior. This leads to a distinct plateau at the maximum forces of the cycles. And therefore almost no strength degradation took place from the yield displacements to the maximum displacements of the cycles. The rocking behavior is visualized in Figure 6.53.

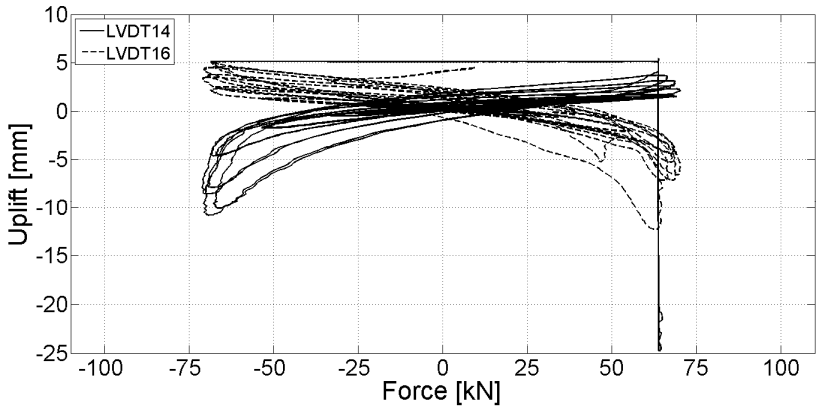

Figure 6.53: I-G10.15:LVDT 14 uplift flange north, LVDT 16 uplift flange south

The capacity curve and its bilinear idealization according to Tomaževič (1999) are shown in Figure 6.54.

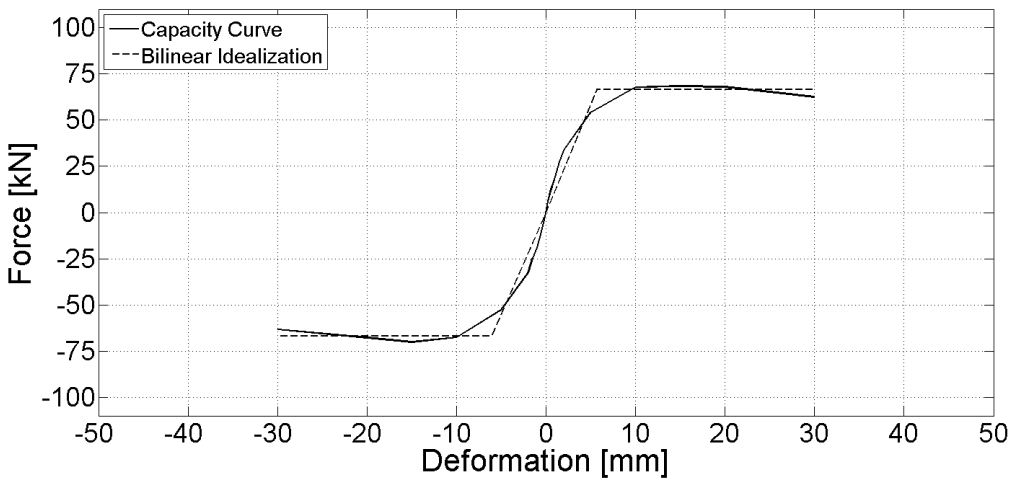

Figure 6.54: Capacity curve and bilinear idealization I-G10.15

All characteristic values of the capacity curve and its bilinear idealization are summarized in Table 6.13

I-G10.15	K_0 [kN/mm]	K_{eff} [kN/mm]	K_{eff}/K_0 [%]	V_{max} [kN]	V_u [kN]	d_u/h_w [%]	d_u [mm]	d_y [mm]	μ [-]
Pushing	30.54	11.75	38.47	70.30	66.51	2.50	30.01	5.66	5.30
Pulling	19.64	11.00	56.04	71.11	67.05	2.50	30.01	6.09	4.93

Table 6.13:Results I-G10.15

6.9.5.2 Crack Pattern and Failure Mode

After an initial rocking behavior the ultimate failure mode was observed to be diagonal tension. The final crack pattern at the end of the test at the beginning of the second pulling cycle of displacement amplitude step 10 (35 mm) is shown in Figure 6.55.

Figure 6.55: Final crack pattern I-G10.15

The propagation of the crack pattern is shown in a series of photos in appendix D. Having a look at the final crack pattern of Figure 6.55 the distinct diagonal crack through the web clearly indicates the failure mode diagonal tension. The direction of the diagonal crack from the southern top to the northern bottom approves that the specimen failed in the pushing direction. The propagation of the diagonal crack through the bricks is typical for a high level of precompression.

Having a look at the crack pattern at the flange-web intersection there are a lot of cracks concentrated in the middle of the flanges. At the intersection on the south the cracks follow the head-joints and also pass through the bricks. This intersection started to fail at the bottom in the first pulling cycle of load amplitude step 7 (10 mm). In the end the web punched through the flange over the entire height. At the intersection on the north the cracks follow primarily the head-joint. Only some single cracks in the lower part of the connection pass through the bricks. No failure of the flange-web intersection could be found on this side.

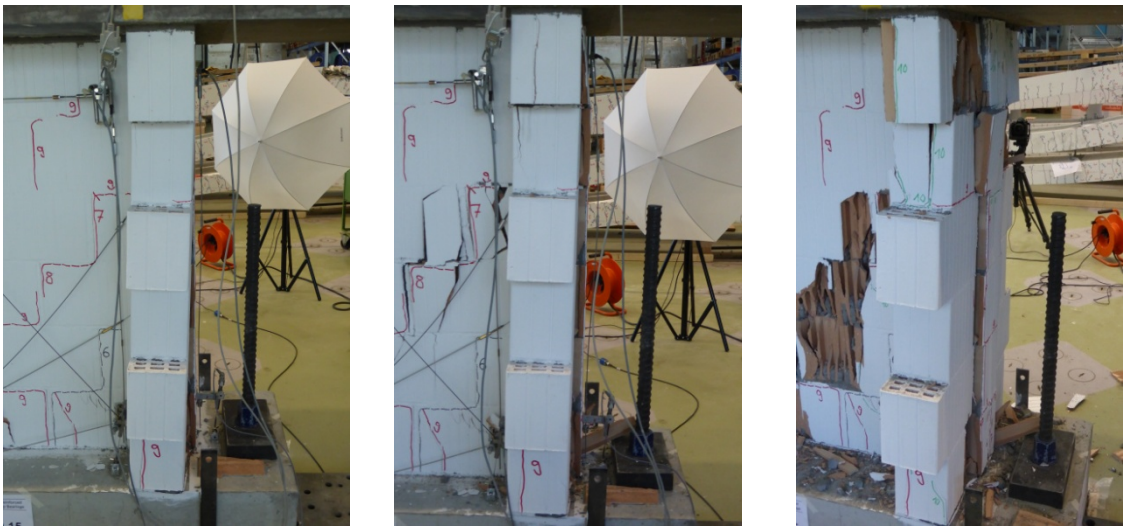

Figure 6.56: Failure of flange-web intersection I-G10.15

When looking at the southern flange the main damage is caused by the web punching through the flange. Furthermore there are two bricks on top of the flange which suffered some damage caused by the shear failure at the very end of the test. On the bottom of the flange not much damage can be found. The northern flange is clearly more damaged at the bottom. Since on this side the flange-web intersection stayed intact the flange contributed more to the transmission of the horizontal force and therefore the bottom is more damaged than at the southern flange. Both flanges are split in the lower part as can be seen in Figure 6.57.

Figure 6.57: Splitting of the flanges I-G10.15: (l) Flange north, (r) Flange south

6.9.5.3 Energy Dissipation

The dissipated energy ratio and the damping ratio are plotted in Figure 6.58. Both values exhibit a constant rising during the test from a displacement of 2 mm. The dissipated energy ratio starts with a value of 0.47 at 2 mm displacement and attends its maximum of 0.76 at a displacement of 30 mm. The damping ratio starts with a value of 0.05 at 2 mm displacement and attends its maximum of 0.14 at a displacement of 30 mm.

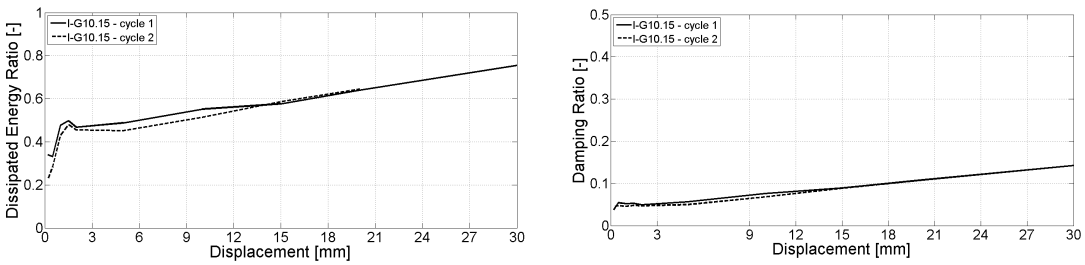

Figure 6.58: I-G10.15: (l) Dissipated energy ratio, (r) Damping ratio

6.9.5.4 Damage SLS Bearing

The 10 mm granulate SLS bearing shows some visible damage especially at the very ends of the web (in the middle of the flanges). The web itself is less damaged except of the connection to the flange on the north. At both connection areas between the web and the flanges a circular rupture is visible. The one at the north is completely cut off from the rest of the layer. As already discussed in the presentation of the results of specimen

I-G10.10 this rather unusual rupture is caused by drilling holes in the concrete basement right under the layer which were not refilled properly (see Figure 6.59 (b)).

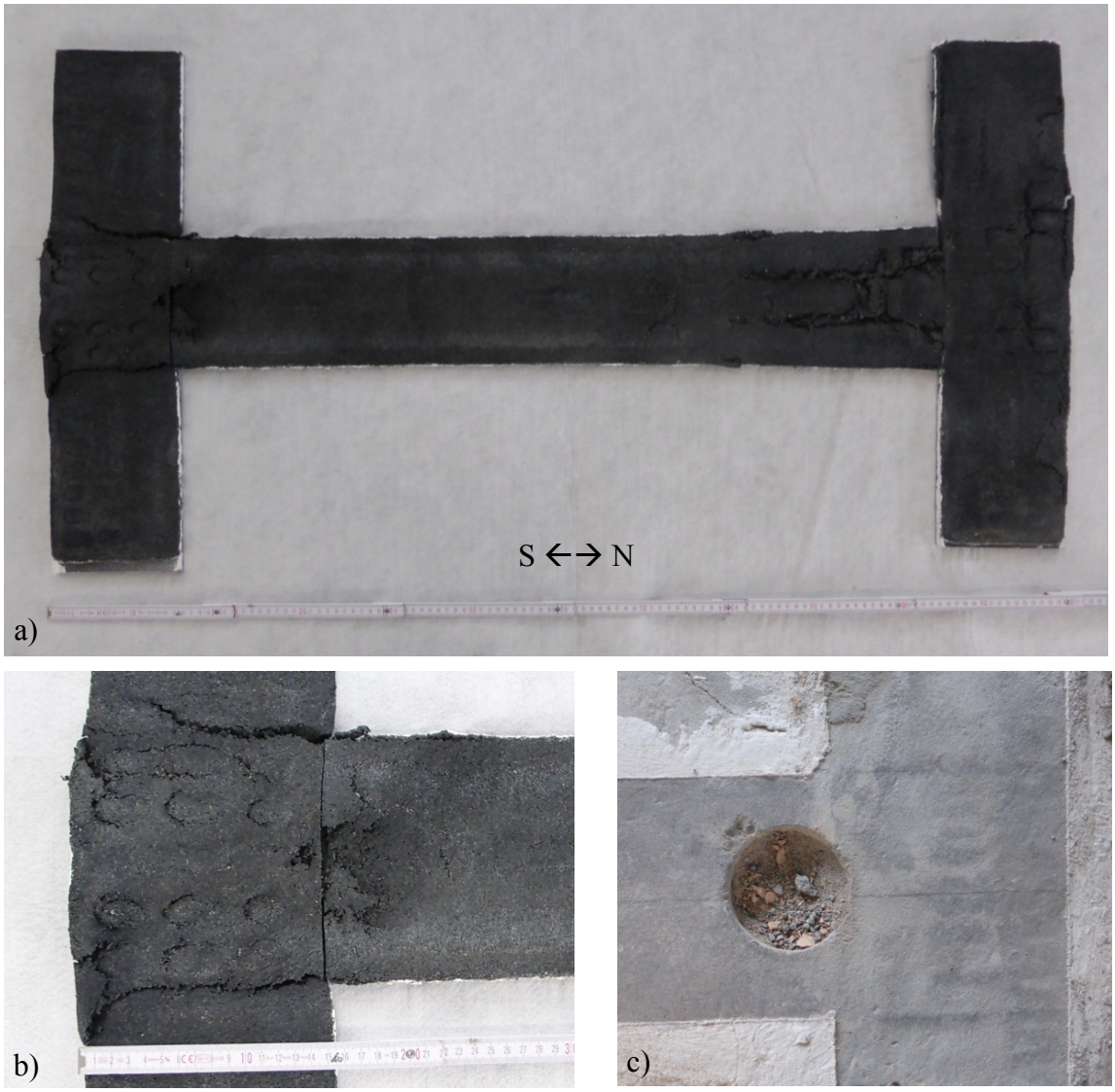

Figure 6.59: (a) Damage SLS bearing I-G10.10: (b) Detail flange south, (c) Drilling hole in the concrete basement flange north

At the southern flange where the web punched through the flange the granulate SLS bearing is almost completely ripped off at the flange-web connection lines.

7 Comparison of Experimental Data and Prediction

An overview of the observed results of the five specimens tested in chapter 6 is given in Table 7.1. The predicted shear strength and failure mode out of chapter 6.7.2 are shown in brackets beside the measured values.

Specimen	Applied precom-pression σ_v [MPa]	Shear strength V_{max} [kN] (Prediction)		Failure mode (Prediction)	
I-0.10	1.0	91.9	(80.9)	V_{dt}	(V_{tc})
I-G3.10	0.6	56.6	(52.6)	V_{tc}	(V_{tc})
I-G3.15	var	101.3	(-)	V_{dt}	(-)
I-G10.10	0.6	50.4	(52.6)	V_{tc}/V_s	(V_{tc})
I-G10.15	0.9	71.1	(76.2)	V_{dt}	(V_{tc})

Table 7.1: Results and prediction of I-shaped URM walls

First of all it can be summarized that all specimens showed an initial rocking behavior, (expect specimen I-G3.15) that was predicted correctly by the theoretical model when the prediction of Figure 6.16 is compared to the achieved shear strength of Table 7.1.

For specimen I-0.10 with no layer and an applied precompression of 1.0 MPa (18.3%) the predicted shear strength of 80.9 kN was exceeded in the test with a value of 91.9 kN. Furthermore the observed failure mode was diagonal tension although toe crushing was predicted. Despite the fact that the shear resistance due to rocking (overturning) and toe crushing was predicted to small the predicted value of 91.5 kN due to diagonal tension (see Figure 6.16) would fit the result almost perfectly. The predicted shear resistance due to sliding with a value of 227.1 kN is very high and therefore was neither expected nor observed in the test.

Having a look at test I-G3.10 and I-G10.10 with a precompression of 0.6 MPa (11.0%) and a granulate SLS bearing the predicted value of 52.6 kN fits well to observed values of 56.6 kN and 50.4 kN respectively. In both cases also the predicted failure mode toe crushing was confirmed by the observations in the tests. The shear resistance due to rocking (overturning) which is only slightly higher than the one due to toe crushing fits to the strong rocking behavior that was observed during both tests. The predicted shear resistances due to sliding and diagonal tension are clearly higher and therefore not supposed to be decisive.

As already mentioned in chapter 6.7.2 for specimen I-G3.15 no prediction is available.

Specimen I-G10.15 with a granulate SLS bearing was tested with a precompression of 0.9 MPa (16.5%). The observed shear strength of 71.1 kN fits quite well to the predicted value of 76.2 kN. However the predicted failure mode toe crushing was not correct. In the test an ultimate failure due to diagonal shear was observed. But it has to be mentioned that in this test before the ultimate failure occurred the web punched through the southern

flange. This fact was not taken into account by the theoretical model that assumes the flange-web intersection to stay intact during the whole test (see assumptions chapter 4.3). To consider this behavior in the theoretical model the shear resistances due to all four failure modes would need to be adjusted. Although the detailed implementation of these adjustments would go beyond the scope of this master's thesis they should be discussed qualitatively hereinafter.

Concerning the failure mode rocking (overturning) the resistance in the direction where the separated flange would be in tension should be corrected downwards because the additional weight of the flange that is separated gets lost. What was observed in the test was that the separated flange stuck to the load transmission plate (as it might also stick to the concrete slab in a building) and therefore the separation had no influence on the shear resistance due to rocking (overturning). This is also confirmed by the results of LVDT 14 and 16 which measure the uplift at the flanges where no difference between both directions can be identified (see Figure 6.53). The resistance due to the failure mode toe crushing in the direction where the separated flange is in compression should also be corrected downwards but maybe less than expected at the first sight. The amount of the reduction depends on the residual ability of the separated flange to contribute to the load transmission. And even after the complete separation it can be assumed that the flange still contributes to the transmission of the additional moment imposed on the top of the wall. Only the contribution to the moment transmission caused by the shear force acting at the top of the wall gets lost. However the exact correction of the shear resistance due to toe crushing would be very demanding. The shear resistance due to the failure mode sliding would also change in a way that it becomes smaller. Since the separated flange contributes still to the transmission of the vertical load but can no longer transfer the resulting horizontal resistance to the rest of the wall. Concerning the failure mode diagonal tension the separation of the flange causes a redistribution of the shear stress in the web. This distribution is represented by the parameter ζ in the model that can be assumed to be equal to 1.0 for I-shaped walls and equal to 1.33 for rectangular walls with an aspect ratio (h/L) of 1 (Yi, 2004). It seems to be reasonable to assume a value of 1.17 for a T-shaped wall as present after the separation of one flange. Interestingly when applying this value in the model the resulting prediction of shear resistance would be equal to 75.3 kN. Assuming this failure mode to be decisive the prediction would fit better to the observed value of 71.1 kN.

All results of the tests, the predicted values and the accuracy of the prediction are shown in Table 7.2.

Specimen	Shear strength V_{max} [kN] (Prediction)	Failure mode (Prediction)	Difference Result – Prediction [%]	Correct prediction of failure mode
I-0.10	91.9 (80.9)	V_{dt} (V_{tc})	-12.0	x
I-G3.10	56.6 (52.6)	V_{tc} (V_{tc})	-7.1	√
I-G3.15	101.3 (-)	V_{dt} (-)	-	-
I-G10.10	50.4 (52.6)	V_{tc}/V_s (V_{tc})	+4.4	√
I-G10.15	71.1 (76.2)	V_{dt} (V_{tc})	+7.2	x

Table 7.2: Accuracy of prediction I-shaped URM walls

All observed and predicted results of the shear strength are repeated and visualized in Figure 7.1.

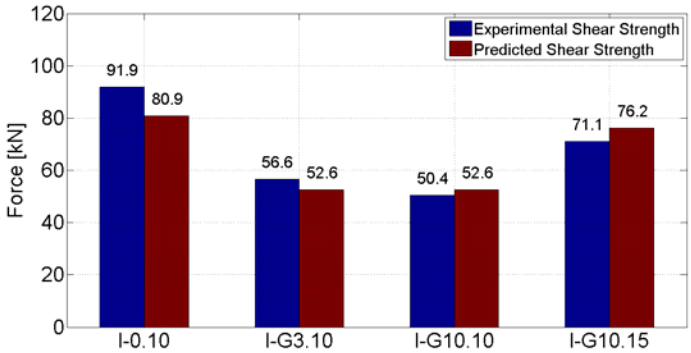

Figure 7.1: Comparison of results and prediction of the shear strength of I-shaped URM walls

Despite the fact that the sample size is very small it can be concluded that overall the model exhibits a mean value of failure in the prediction of the shear strength of 7.7% with a standard deviation of 3.2%. Taking into account the change in the distribution of the shear stress in the test of I-G10.15 where the web pushed though the flange the accuracy of the model is even a little better with a mean value of the failure in the predicted shear strength of 7.4% and a standard deviation of 3.3%. Concerning the failure modes 2 of 4 were predicted correctly.

8 Influence of Boundary Condition

In all tests, except of test I-G3.15, a distinct rocking behavior was observed. This rocking behavior is typical for walls with a high aspect ratio (h/L). The analysis of the statics of the conducted tests in Figure 6.10 illustrates that transferred to the cantilever boundary condition the effective aspect ratio of the wall specimen would be calculated as (h+h')/L. This means the effective aspect ratio or shear span H_0 of the wall specimens with a height according to the cantilever boundary condition is equal to 1.75 or 1.75h respectively. This fact explains the intense rocking behavior which was observed during the tests and can also be clearly seen in the distinct S-shapes of the hysteresis loops. For clearance the difference in the load transfer between the cantilever boundary condition (H_0=1.0h) and the boundary condition for a shear span H_0=1.75h is visualized schematically by means of stress fields in Figure 8.1. The smaller effective length on the bottom of the wall in case of H_0=1.75h leads to the more distinct rocking behavior.

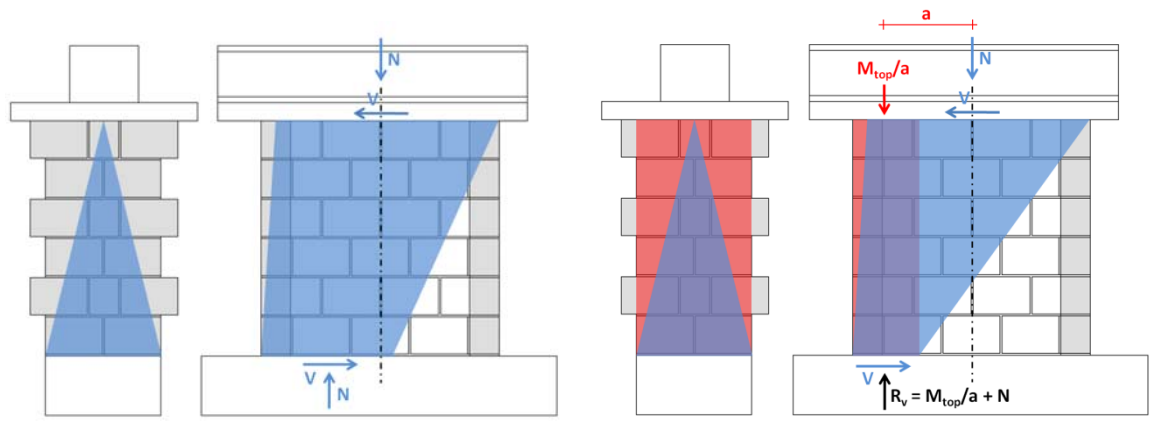

Figure 8.1: Lateral load transfer, (l) H_0=1.0h, (r) H_0=1.75h

The clear S-shape of the hysteresis loops of walls with a high shear span was also found by Petry and Beyer (2014) when they tested rectangular URM walls on full scale and is also described in Gams and Tomažević (2012) where they present the results of rectangular URM walls tested on half scale under different boundary conditions. Furthermore Petry and Beyer (2014) concluded that a higher shear span leads to an increase in the deformation capacity.

In their test series Gams and Tomažević (2012) conducted an interesting test under the boundary condition of a fixed end on the bottom and restraint rotations and vertical displacements on the top. When having a closer look at the measuring results of test I-G3.15 it seems to be reasonable to idealize the boundary condition to the mentioned case of Gams and Tomažević. First the rotations during the test are analyzed. As can be seen in Figure 8.2 they are very small in particular when they are compared to the ones of test I-G10.15 where the rotations were free. And also the difference between the lateral displacement of the horizontal hydraulic actuator and the laser device is very small (see Figure 8.3) indicating rather a fixed-fixed than a cantilever boundary condition.

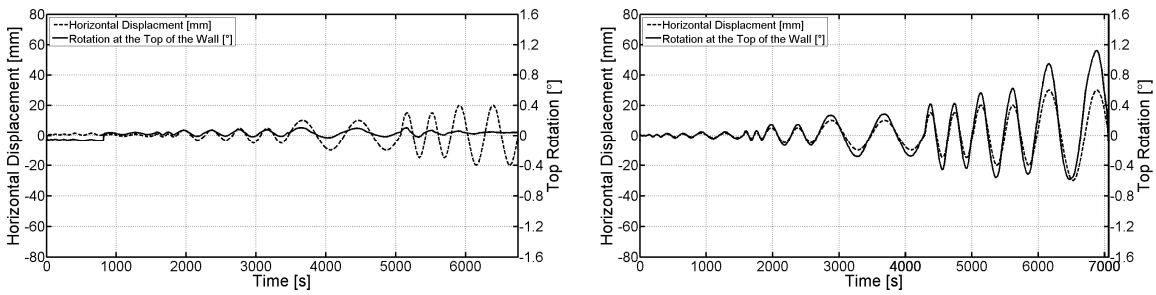

Figure 8.2: (l) Rotation at the top of the wall I-G3.15, (r) Rotation at the top of the wall I-G10.15

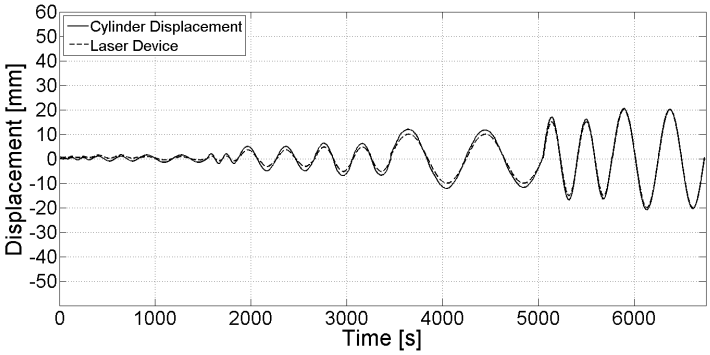

Figure 8.3: Displacement of horizontal hydraulic actuator and laser device I-G3.15

Furthermore the vertical displacements are restrained by the steel bars. Only some small displacements due to the elastic deformation of the steel bars may be possible. No plastic deformations where observed in the context of the investigation of the steel bars after the test. At the end of the test the applied precompression was back-calculated using on the one hand the exact displacement values and corresponding forces of the vertical hydraulic actuators with the tightened safety steel bars and on the other hand the corresponding forces after replacing the loading beam at exactly the same position with the loosened steel bars. This calculation revealed that only 11% of the target precompression of 0.9 MPa were taken by the safety steel bars in the end of the test. And since the wall is less stiff in the end the initial precompression can be assumed to be between 0.8 and 0.9 MPa. What has to be kept in mind is that due to the kinematic relations the precompression is reduced the more the top of the wall is displaced laterally as illustrated in Figure 8.4.

Figure 8.4: Vertical displacement of load transmission plate

The change of the vertical displacement depends on the length of the steel bars and can be calculated according to equation 8-1.

$$\Delta y = R \cdot (1 - cos(\alpha)) \qquad \textit{(Eq. 8-1)}$$

The steel bars exhibit a length of 600 mm and the maximum displacement during the test was 20 mm so the maximum change of the height of the load transmission steel plate was 0.3 mm.

Assuming the fixed boundary condition at the bottom of the wall and the restraint rotations and vertical displacements for test I-G3.15 its results can be compared to the ones of Gams and Tomažević (2012). The hysteresis loops of both tests are shown in Figure 8.5. Wall 3 and 4 were tested by applying a precompression level of 20% and 10%, respectively while specimen I-G3.15 was tested with a precompression level of about 15%.

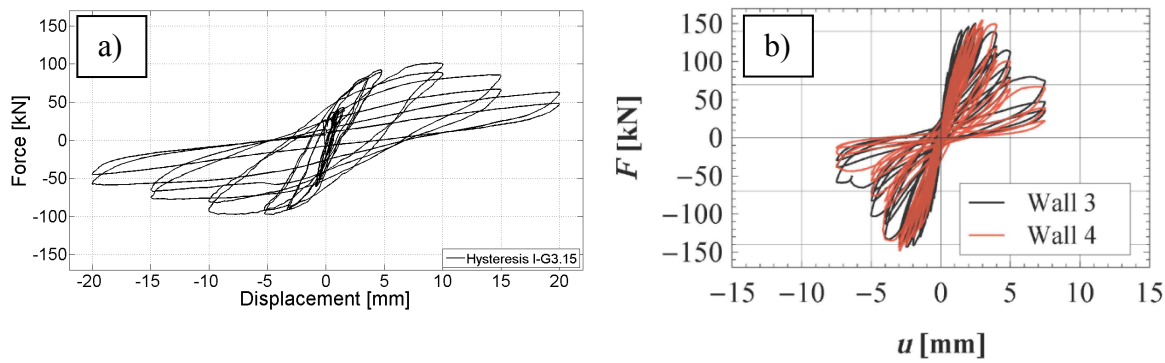

Figure 8.5: (a) Hysteresis loops I-G3.15, (b) Hystersis loops wall 3 and 4 (Gams & Tomažević, 2012)

Both hysteresis loops exhibit no S-shapes what fits to the observations in test I-G3.15 where no rocking was observed. While the shapes of the single loops are quite similar the deformation capacity of specimen I-G3.15 is much higher than the one of walls 3 and 4 of Gams and Tomažević (2012). This difference might be caused by the 3 mm granulate layer which is applied in the test I-G3.15. After having reached the maximum force the strength degradation is much more intense in the tests of Gams and Tomažević (2012). Absolute values of the lateral force and displacement are more complicated to compare because different types of masonry with different material properties were used and there is the difference of the soft-layer too. But the flanges seem not to increase the maximum force which can be explained by the flange-web intersections which were not able to transfer the load, at least not fully. Despite the fact that the shapes of the hysteresis loops of test I-G3.15 and the ones of the tests of Gams and Tomažević (2012) do not fit perfectly it seems to be reasonable to idealize the boundary condition at the top of specimen I-G3.15 as fixed rotations and vertical displacements especially when comparing the shape of the hysteresis to the one of test I-G10.15 which is completely different. Moreover when the capacity curve of test I-G3.15 is compared with the one of test I-G10.15 a higher shear strength and a smaller deformation capacity are observed for specimen I-G3.15 exhibiting a smaller shear span of about H_0=0.5h or a little higher.

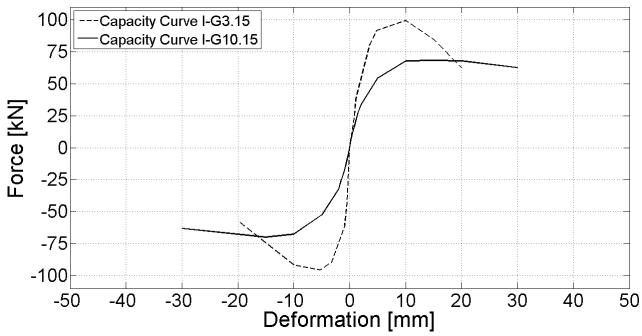

Figure 8.6: Capacity curves I-G3.15 and I-G10.15

These results fit perfectly to the observations of Petry and Beyer (2014) about the influence of the shear span.

9 Influence of SLS Bearing

The influence of an applied SLS bearing in the interface joint can be investigated by comparing the results of test I-0.10 without a soft-layer with the results of test I-G10.15 with a 10 mm granulate soft-layer. Due to the calibration failure of the load cells of the vertical hydraulic actuators specimen I-0.10 was tested at almost the same level of precompression (σ_v = 1.0 MPa) as the specimen in test I-G10.15 (σ_v = 0.9 MPa).

9.1 Force-Displacement Response

The hysteresis loops of a specimen without (red) and of one with an applied SLS bearing (green) are completely different as can be seen in Figure 9.1. In this figure on the right also the capacity curves and their bilinear idealizations are shown.

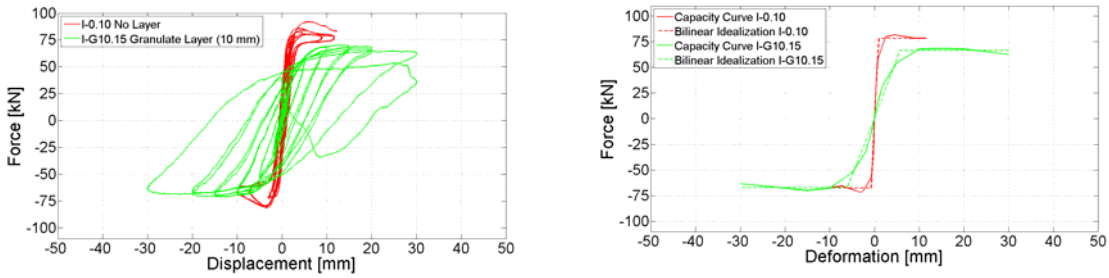

Figure 9.1: Effects of SLS bearing: (l) Hysteresis loops, (r) Capacity curves and bilinear idealizations

A significant effect of the soft-layer is the reduction of the shear strength. In the present case the maximum shear strength is reduced by 23% when a soft-layer is applied. But although this is a negative effect, especially from the point of view of a force-based design approach, the soft-layer also has some serious advantages concerning the seismic performance of the wall. With the applied soft-layer the deformation capacity is much higher. The combination of this two effects lead to a clear reduction of the effective stiffness with an applied soft-layer. And despite the ductility capacity is lower with an applied soft-layer the yield displacement is much higher and therefore the wall rests longer in its elastic range from a displacement-based point of view. This is a serious advantage because the plastic part of the deformation of an URM wall is hard to describe and to calculate in a reliable way. Another advantage of the applied granulate soft-layer is the higher energy dissipation which in discussed in detail in chapter 9.3.

What has to be kept in mind when using a soft-layer is the distinct rocking behavior that is caused. Although in the conducted tests the rocking behavior avoids a fast strength degradation by storing a lot of energy in the higher displacement cycles it can cause harmful dynamic impulses at higher testing frequencies when the stored energy is set free abruptly.

Nevertheless SLS bearings have the potential to enhance the seismic performance of I-shaped URM walls by providing a higher deformation capacity.

9.2 Crack Pattern

An early comparison of the crack pattern at small displacements shows the influence of the applied soft-layer. While the web with an applied soft-layer is still almost perfectly intact the one without a soft-layer exhibits already distinct diagonal cracks. In Figure 9.2 the crack patterns at a displacement of 5 mm are compared.

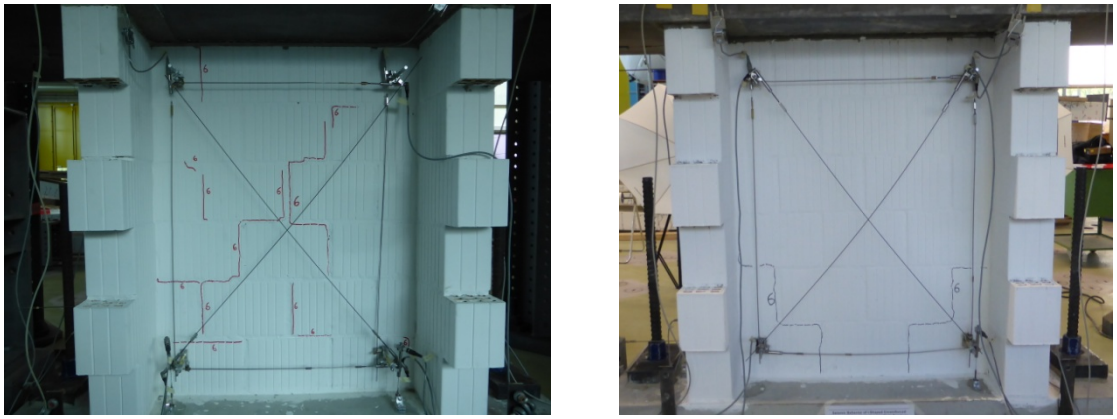

Figure 9.2: Comparison crack pattern at 5 mm displacement: (l) I-0.10, (r) I-G10.15

Although the progress of the crack pattern according to the displacement amplitude steps is completely different the final crack pattern looks similar. Both specimens failed due to diagonal tension. The direct comparison of the final crack pattern of the webs is shown in Figure 9.3.

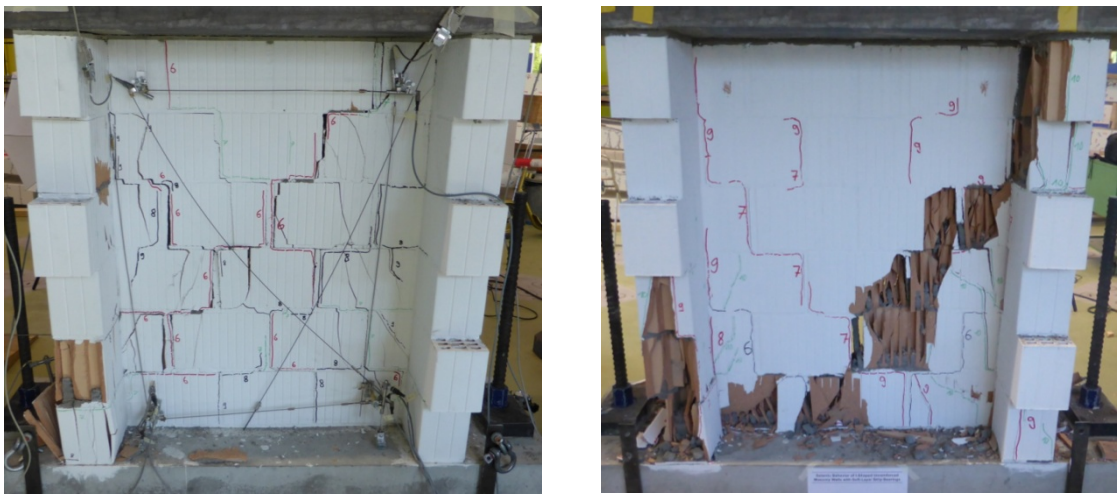

Figure 9.3: Effect of SLS bearing on final crack pattern: (l) I-0.10, (r) I-G10.15

As can be seen in Figure 9.3 there is a difference in the position of the diagonal cracks. This is supposed to happen because in the case with an applied soft-layer the flange-web intersection was hardly damaged (northern flange) or even failed completely (southern flange) while in the case without soft-layer the intersection stayed almost perfectly intact. In the consequence the compressed zone of the bottom of the wall is more concentrated to the edge of the wall in the case without a soft-layer where the flange contributes much

more to the lateral load transmission and therefore shifting the diagonal crack to the left (according to Figure 9.3).

9.3 Energy Dissipation

The energy dissipation is compared in Figure 9.4. While the difference in the dissipated energy ratio is clearly visible the values are much more similar comparing the damping ratios. In both cases the energy dissipation with an applied soft-layer is higher. Except at a displacement of approximately 3 mm the damping ratio without a soft-layer is higher (only first cycle). This may be due to the fact that in this displacement range the specimen without a soft-layer is already in the plastic range and suffering much damage. Therefore it dissipates a lot of energy while specimen I-G10.15 is still in its elastic range.

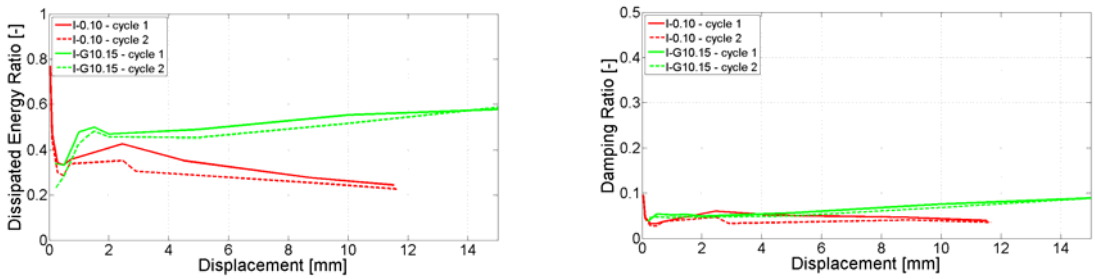

Figure 9.4: Effects of SLS bearing on energy dissipation: (l) Dissipated energy ratio, (r) Damping ratio

The energy dissipation of specimen I-G10.15 is rising when the displacement and damage get bigger.

9.4 Splitting of the Flanges

In all tests, except I-G3.15, a splitting of the flanges was observed as documented in the description of the results in chapter 6.9. In most of the cases the crack occurs almost in the middle of the flange width and propagates through the lowest three rows of bricks.

To explain these observations two possible reasons are discussed which may both contribute to the splitting of the flanges. On the one hand the splitting may be induced by the lateral expansion of the soft-layer which is significantly higher than the lateral expansion of the bricks. The resulting stresses are visualized in Figure 9.5. As a simplification, just to show the effect, the boundary conditions are idealized and the mortar layer between the SLS bearing and the brick is neglected.

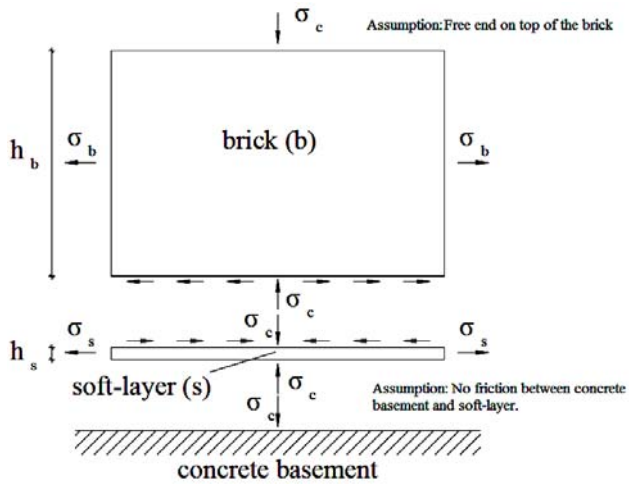

Figure 9.5: Lateral tension induced by SLS bearing

On the other hand the splitting of the flanges may be caused by the incompatibility of displacements that induces lateral tension due to the resulting restraints. As revealed in chapter 9.1 the soft-layer leads to a higher deformation capacity. With higher displacements the flange is bended out of plane due to the deformation shape of the web that is assumed to be approximately parabolic towards the bottom of the wall.

This approach fits to the observation that the effect of splitting is most distinct for specimen I-G10.10 that was exposed to the highest lateral displacement of 40 mm. And it fits also to the observation that the splitting occurs only in the lowest three rows of brick were the curvature is supposed to be the highest. Furthermore this approach is confirmed by the observations in test I-G10.15. In this case the web punched through the southern flange at a lateral displacement of 10 mm. As a consequence the flange did no longer have to follow the displacement shape of the web and could deform separately as can be seen in Figure 9.6.

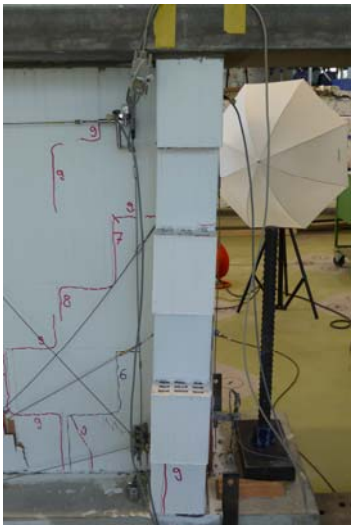

Figure 9.6: Deformation shape of flange after the web punched through I-G10.15

The restraints were therefore smaller (because the curvature got smaller) and the splitting far less distinct compared to the northern flange where the web did not punch through as can be seen in the final crack pattern in Figure 6.55.

10 Effects of the Vertical Load Magnitude

According to the conducted test series the effects of the vertical load magnitude, which is known to have a significant influence on the seismic response of an URM wall, should be visible by comparing the results of test I-G3.10 with those of test I-G3.15 and the results of I-G10.10 with those of test I-G10.15. Since test I-G3.15 was conducted under a different boundary condition the effect of the vertical load magnitude can only be analyzed by comparing the two tests with the 10 mm granulate SLS bearings. This is done in the following sub-chapters. The findings are compared to the conclusions of Vögeli (2014) for rectangular URM walls.

10.1 Force-Displacement Response

The hysteresis loops of both tests and the bilinear idealization of their capacity curves are shown in Figure 10.1. The corresponding mean values (except of the maximum force where the higher value is listed) of the pushing and pulling direction of the idealized capacity curves are listed in Table 10.1.

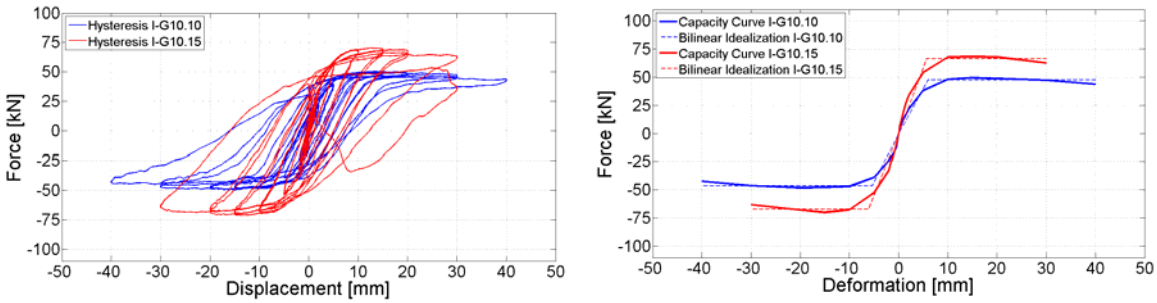

Figure 10.1: Comparison tests I-G10.10 and I-G10.15: (l) Hysteresis loops, (r) Capacity curves and bilinear idealizations

	K_0 [kN/mm]	K_{eff} [kN/mm]	K_{eff}/K_0 [%]	V_{max} [kN]	V_u [kN]	d_u/h_w [%]	d_u [mm]	d_y [mm]	μ [-]
I-G10.10	24.17	8.28	34.28	50.38	46.91	3.34	40.03	5.68	7.07
I-G10.15	25.09	11.38	47.26	71.11	66.78	2.50	30.01	5.88	5.12

Table 10.1:Comparison of tests I-G10.10 and I-G10.15

In Figure 10.1 it can be seen that a higher level of precompression leads to a significant higher shear strength and lower ultimate deformation. After the very beginning of the test where the initial stiffness (K_0) is almost the same for both in the rest of the test with increasing displacements specimen I-G10.15 with a higher level of precompression is acting much stiffer. This significant influence of the vertical load magnitude on the shear strength and deformation capacity is also described in the findings of Vögeli (2014) for the equivalent rectangular URM walls. Furthermore the increased shear strength according to all four failure modes due to the higher precompression can also be seen in

the theoretical model of rectangular and I-shaped URM walls in chapter 5 for a cantilever boundary condition as well as in the adjusted prediction of chapter 6.7.2.

Another change with the level of precompression that could be observed in the tests was the clear reduction of the rocking behavior by increasing the precompression. What seems to be intuitive is confirmed by the results of the LVDT's number 14 and 16 measuring the uplift of the flanges as shown in Figure 10.2. By increasing the precompression from 0.6 to 0.9 MPa the uplift movement is cut to half.

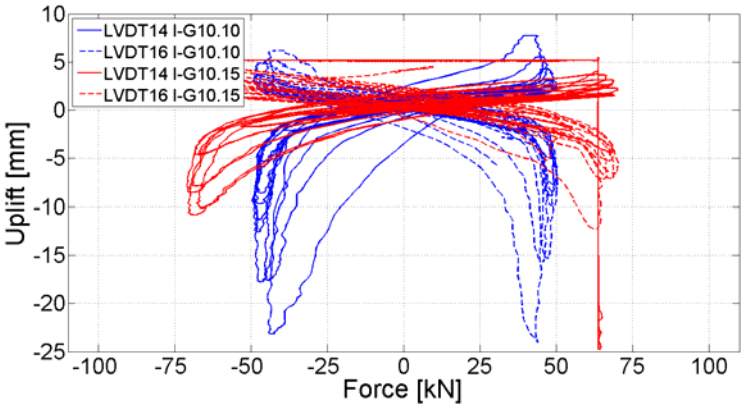

Figure 10.2: Comparison of uplift of tests I-G10.10 and I-G10.15

This finding cannot directly be transferred to a complete structure because a higher precompression is achieved by a bigger mass which leads also to higher lateral forces due to the earthquake excitation. Nevertheless for a fixed horizontal force the system gets more stable with a higher level of precompression.

10.2 Crack Pattern

As already mentioned in the discussion of the results in chapter 6.9 the failure mode of specimen I-G10.10 according to its final crack pattern can be identified as toe crushing combined with a secondary sliding motion. Having a look at the failure mode of specimen I-G10.15 the increased precompression leads to a change in the failure mode from toe crushing to diagonal tension.

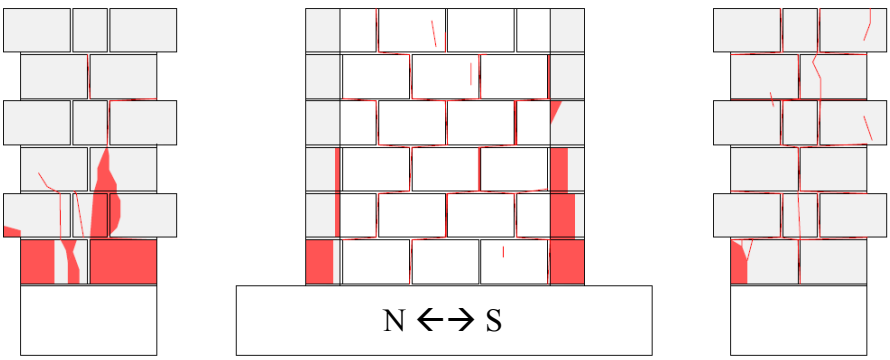

Figure 10.3: Schematic crack pattern I-G10.10

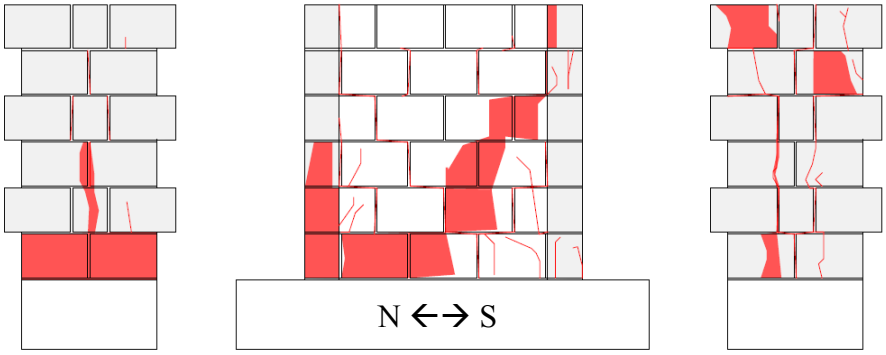

Figure 10.4: Schematic crack pattern I-G10.15

Interestingly Vögeli (2014) observed the same change of failure mode by increasing the precompression for the equivalent rectangular walls. Since he observed the same for the two wall specimens with the thinner 3 mm granulate layer (WG3.10 and WG3.15) this effect seems to be caused primarily by the vertical load magnitude and does not seem to be sensitive to the thickness of the applied granulate SLS layer. Having a look at the prediction of the failure mode of chapter 5 for a cantilever boundary condition the failure mode for specimen I-G10.10 is predicted to be also diagonal tension as for the specimen I-G10.15. Therefore the change of failure mode might be caused by the additional moment and would eventually not be observed for a cantilever boundary condition.

When having a closer look at the flange-web intersection the higher precompression leads to a distinct higher damage. This seems plausible because due to the higher lateral force also the force transmission from the web to the flange is higher, especially in the lower part. In case of specimen I-G10.15 the southern end of the web even punched through the flange. This problem has to be kept in mind when increasing the normal force and has to be closer investigated in future experiments.

10.3 Energy Dissipation

The energy dissipation is compared in Figure 10.5 using the dissipated energy ratio and the damping ratio. For both ratios it can be concluded that with an increasing vertical load magnitude more energy is dissipated. But also the failure mode has to be taken into account which may have a significant influence on the energy dissipation. While in test I-G10.1O toe crushing was observed to be the main failure mode it was diagonal tension for test I-G10.15. No nameable difference was found in the energy dissipation of these two failure modes in the test of rectangular URM walls of Vögeli (2014). On the opposite he observed that a sliding failure, which was not decisive in any of the present tests of I-shaped URM walls, can increase the energy dissipation significantly.

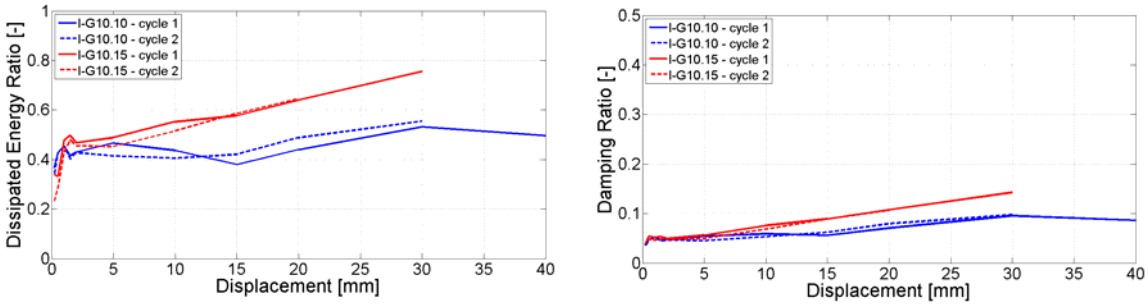

Figure 10.5: Comparison energy dissipation I-G10.10 and I-G10.15: (l) Dissipated energy ratio, (r) Damping ratio

Since Vögeli (2014) did not observe a dependence of the energy dissipation on the vertical load magnitude this may be a specialty of I-shaped walls.

10.4 Damage SLS Bearing

As can be seen in Figure 10.6 the damage of the soft-layer does not differ significantly. In both cases the damage is concentrated at the flange-web intersection and on the outer edge of the flanges. However the damage is slightly higher in the case of specimen I-G10.15 which indicates that the damage of the soft-layer corresponds with the precompression level. The two significant ruptures through the southern flange of specimen I-G10.15 parallel to the web along the intersection lines are caused by the failure of the flange-web intersection described in chapter 11.4 and are not directly related to the vertical load magnitude.

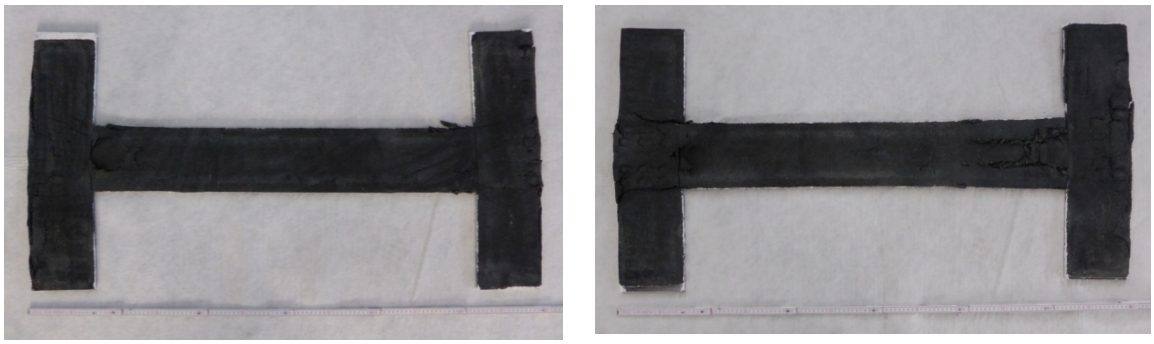

Figure 10.6: Comparison SLS bearing damage: (l) I-G10.10, (r) I-G10.15

The damage of the granulate SLS bearings of the equivalent rectangular URM walls of Vögeli (2014) is hard to identify in the photos of Figure 10.7. But in his comments he describes almost no deterioration in the case of specimen WG10.10 (except of the visible rupture) and some traces of deterioration and plastic deformations in the case of specimen WG10.15 which indicates that he also found the same relation between the damage of the granulate SLS bearing and the vertical load magnitude for rectangular URM walls.

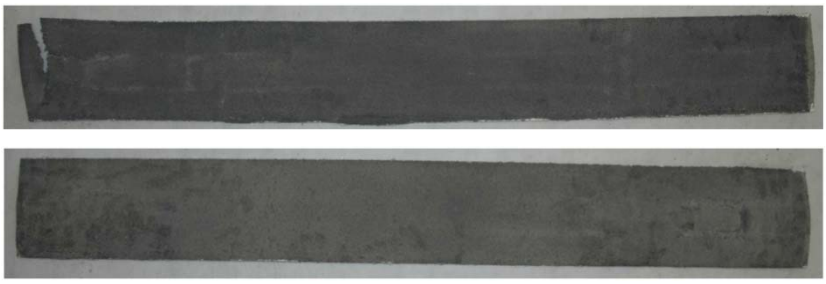

Figure 10.7: Comparison damage SLS bearing: (t) WG10.10, (b) WG10.15 (Vögeli, 2014)

11 Effects of Flanges Based on Experimental Data

In the following chapter the results of the tests on I-shaped URM walls are compared to the results of Vögeli (2014) who conducted tests on rectangular URM walls of the same geometry. Although a direct comparison is not possible due to the different boundary conditions (he used the cantilever boundary condition) the comparison of the observed effects is instructive.

11.1 Force-Displacement Response

In Figure 11.1 the bilinear idealizations of the capacity curves of the conducted tests in chapter 6 are visualized together with the idealized capacity curves of Vögeli (2014). Test I-G3.15 is left out due to the manipulation failure.

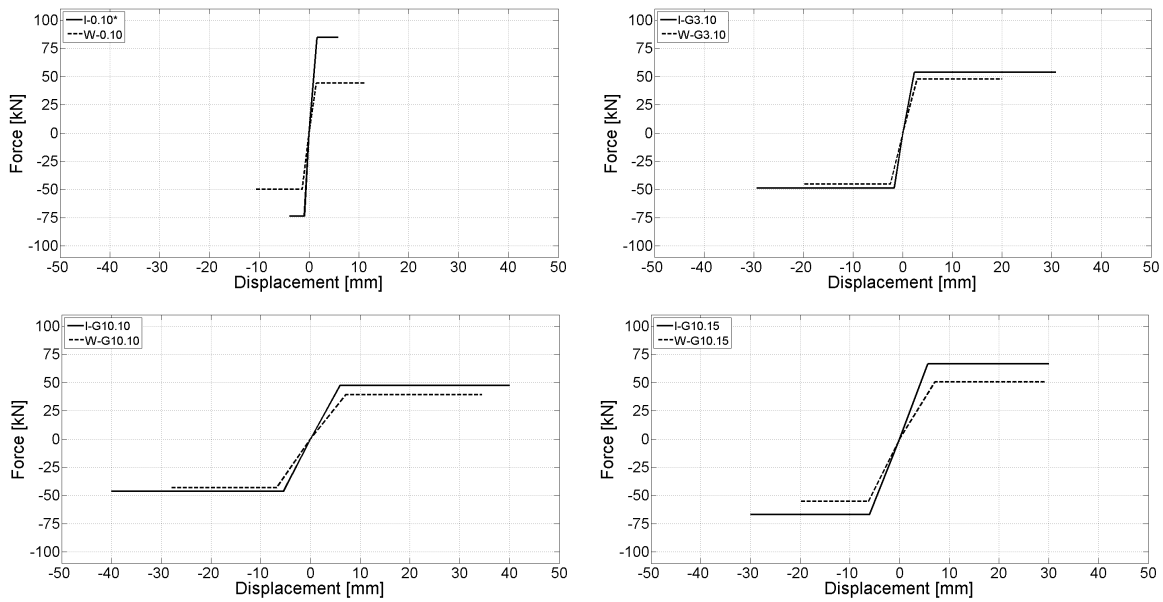

Figure 11.1: Comparison of rectangular and I-shaped URM walls

In Table 11.1 the results of the shear strengths are compared to the results of Vögeli (2014). Except of the test without a layer no big difference in the shear resistance can be seen. But nevertheless the shear strengths of the I-shaped URM tests are all slightly higher. The reason for the significant increase of shear strength for the specimens without a soft-layer is the higher level of precompression that was applied in the test of the I-shaped specimen. That is why this test is marked with a star. A direct comparison of these two tests is therefore not possible.

Specification	Rectangular URM walls V_{max} [kN]	I-shaped URM walls V_{max} [kN]	Increase [%]
0.10	52.5	-	-
0.10*	-	91.9	-
3.10	50.8	56.6	+11.4
3.15	74.6	101.34	-
10.10	46.8	50.4	+7.7
10.15	60.5	71.1	+17.5

Table 11.1:Effect of flanges on shear strength

Even the horizontal load could not be increased much in absolute values the presence of an additional moment in the tests of the I-shaped URM walls lets assume that the shear resistance with a cantilever boundary condition for the same walls could be increased significantly if no shear (diagonal tension) or sliding failure gets decisive. Since the shear resistance of rocking and toe crushing are increased linearly according to equations 6-6, 6-7 and 6-8 the increase could theoretically be up to a value of 75% to attain the same moment at the bottom of the wall as can be calculated out of equation 11-1.

$$(V + x \cdot V) \cdot h = V \cdot (h + h') \qquad \textit{(Eq. 11-1)}$$

Since according to the adjustments of the I-shaped adapted modified effective pier model in chapter 6.7.1 no change of the shear resistance due to diagonal tension happens when the additional moment is applied which means that the shear resistance of the prediction in chapter 6.7.2 is also valid for a cantilever boundary condition. And therefore diagonal tension would get decisive at an increase of the shear force between approximately 0 and 50% according to Table 11.2.

Specimen	Observed V_{max} in the tests with an additional moment [kN]	Predicted V_{max} due to decisive failure mode "Diagonal Tension" for cantilever BC [kN]	Potential increase of shear strength [%]
I-0.10	91.9	91.5	0.0
I-G3.10	56.6	75	32.5
I-G3.15	-	-	-
I-G10.10	50.4	75	48.9
I-G10.15	71.1	87.7	23.3

Table 11.2:Potential increase of shear strength for cantilever boundary condition

The fact that the shear strength of the test without a soft-layer exhibits a potential increase of zero means that the I-shaped specimen without soft-layer and a correct level of precompression of 0.6 MPa would attain the same shear strength with a cantilever boundary condition as the tested specimen with a higher precompression level of 1.0 MPa and an additional moment imposed on top of the wall. Table 11.2 shows a direct

comparison of the observed maximum shear strength with the potential shear strength for a cantilever boundary condition of the I-shaped specimens.

Due to this hypothetical comparison the flanges can increase the shear strength significantly. This effect was already found in the comparison of the theoretical models of rectangular and I-shaped URM walls in chapter 5.

The displacements of the I-shaped URM walls tested in chapter 6.9 are compared to the displacement of the tests of Vögeli (2014) conducted on equivalent rectangular URM walls. Still kept in mind has to be the difference in the boundary condition. Petry and Beyer (2014) found in their experiments that a higher shear span leads to a increase in the deformation capacity. Therefore the ultimate deformations of the I-shaped walls with a shear span of H_0=1.75 are generally expected to be higher than the once of the rectangular walls with a shear span of H_0=1, independent of the effects of flanges.

Specification	**Rectangular URM walls**			**I-shaped URM walls**			**Comparison**
	d_y [mm]	**d_u [mm]**	**μ [mm]**	**d_y [mm]**	**d_u [mm]**	**μ [mm]**	**$\mu_{I\text{-}shaped}$ / $\mu_{rectangular}$ [-]**
0.10	1.7	13.4	7.76	-	-	-	-
0.10*	-	-	-	0.8	10.7	12.87	-
3.10	3.0	19.2	6.42	2.0	30.1	14.97	2.33
3.15	3.1	14.5	4.74	-	-	-	-
10.10	6.9	28.7	4.15	5.7	40.03	7.07	1.70
10.15	6.9	22.9	3.33	5.9	30.01	5.12	1.54

Table 11.3:Effect of flanges on lateral deformation capacity (mean values of pushing and pulling)

In Table 11.3 it can be seen that the I-shaped URM walls attain (as expected) a distinct higher ductility than the equivalent rectangular walls no matter of the thickness of the applied layer. Since Russel et al. (2014) also observed this effect of flanges comparing their I-shaped test to the results of rectangular walls it can be assumed that this effect is not fully due to the higher shear span of the I-shaped walls. For the specimen with a 3 mm granulate layer the ductility of the flanged walls is more than twice as high as for the rectangular one. Overall the effects of the soft-layer thickness and the level of precompression on the ductility factor seem to be very similar for rectangular and for I-shaped URM walls. However the influence of the soft-layer thickness seems to be much stronger than the influence of precompression. More about the influence of the soft-layer thickness can be read in Egeter (2014).

11.2 Energy Dissipation

In Figure 11.2 the energy dissipation of the I-shaped URM walls is compared to the one of the equivalent rectangular URM walls of Vögeli (2014). Tests I-0.10 and I-G3.15 are

left out due to the difference in the level of precompression and the manipulation failure, respectively.

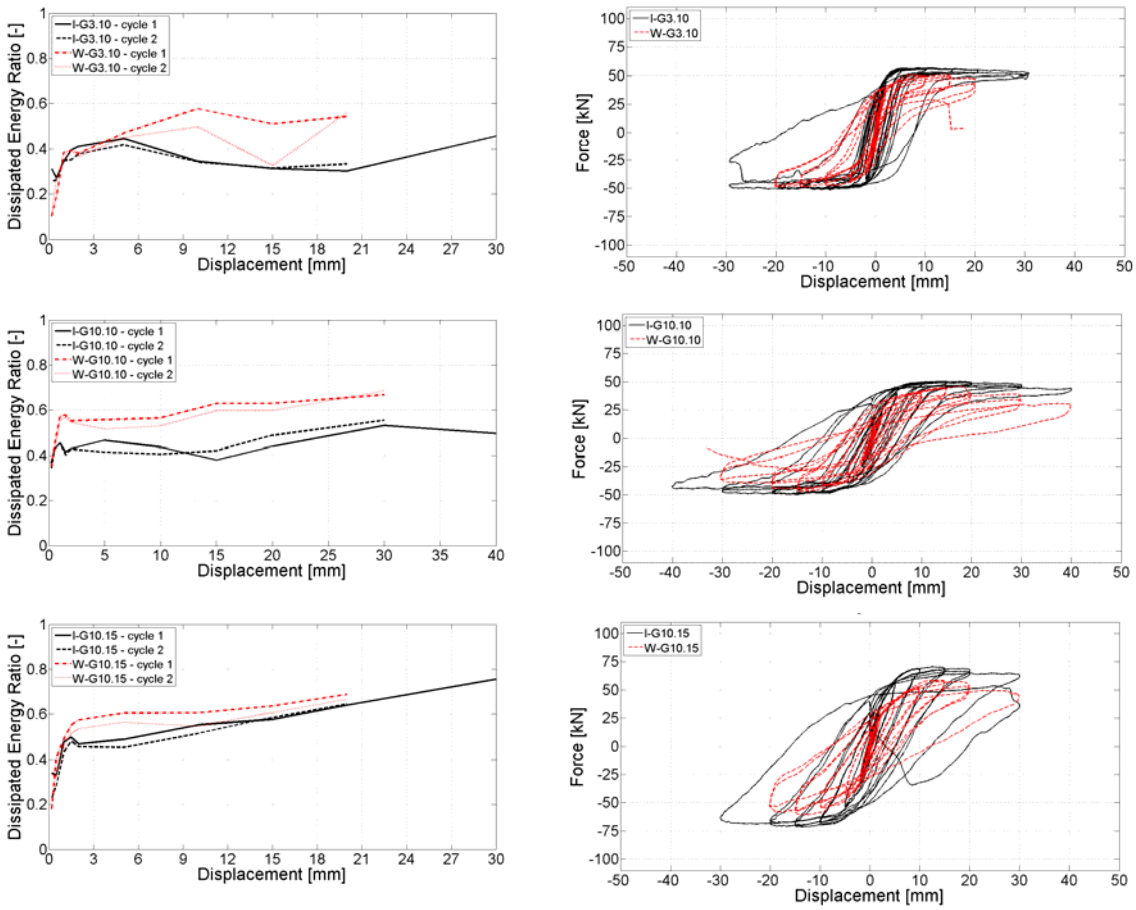

Figure 11.2: Comparison of energy dissipation of rectangular and I-shaped URM walls

As can be seen in Figure 11.2 the URM walls without flanges dissipate more energy. This effect seems to become less distinct for a higher level of precompression. Since the observed failure modes for the I-shaped and the rectangular URM walls are identical the difference can be explained by directly analyzing the hysteresis loops. While the hysteresis loops of the I-shaped URM walls are very narrow in the range of the maximum force of each cycle the hysteresis loops of the rectangular URM walls are wider. This is caused by the additional moment acting on top of the wall in the case of the I-shaped URM walls. This moment leads to a more distinct rocking behavior and therefore higher displacements but causes almost no energy dissipation while for the rectangular wall the same displacement with cantilever boundary condition leads to more damage and therefore higher energy dissipation.

11.3 Damage SLS Bearing

The damage of the granulate SLS bearings of I-shaped and rectangular walls is shown in Figure 11.3. Tests I-0.10 and I-G3.15 are left out due to the difference in the level of precompression and the manipulation failure, respectively.

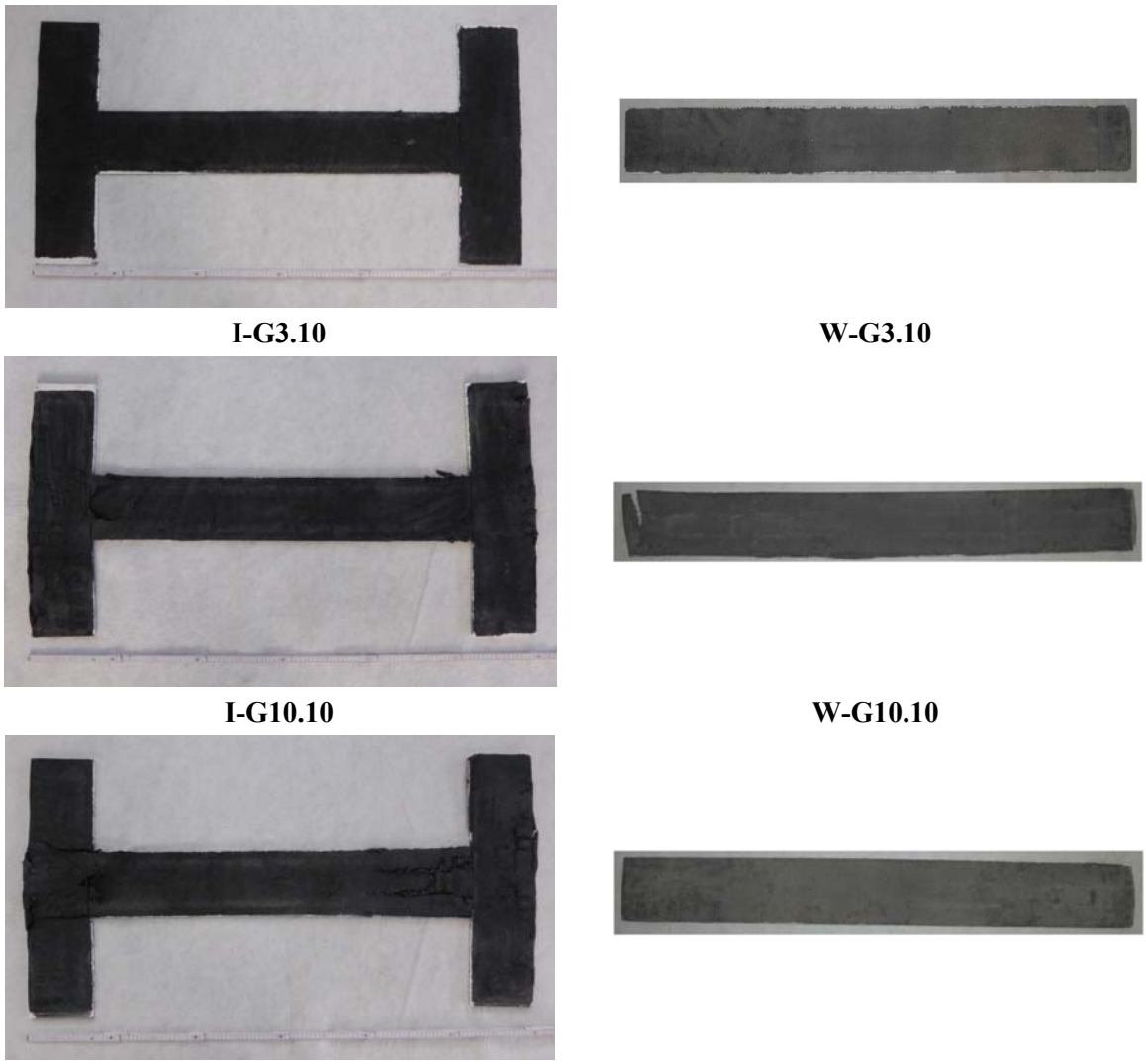

I-G3.10 **W-G3.10**

I-G10.10 **W-G10.10**

I-G10.15 **W-G10.15**

Figure 11.3: Comparison damage SLS bearings I-shaped and rectangular URM walls (Vögeli, 2014)

For the pictured cases the failure mode of each pair (I-shaped and rectangular URM wall) is identical. There is no significant difference in the extent of damage visible. The observed damage in the pictured cases is generally low for I-shaped as well as for all rectangular URM walls. Vögeli (2014) discovered that high damage of granulate SLS bearings is only observed when a sliding failure or at least a combined failure including sliding occurs. This correlates with the observations for I-shaped URM walls where for the failure modes toe crushing (I-G3.10 and I-G10.10) and diagonal tension (I-G10.15) no significant damage was observed. Therefore the flanges do not seem to influence the extent of damage of the granulate SLS bearing.

11.4 Shear Capacity of the Flange-Web Intersection

Comparing the first test of the specimen I-0.10 to the other tests with SLS bearings a clear difference in the crack pattern of the flanges can be observed. When a SLS bearing is applied the flange-web intersection is much more damaged than without a SLS bearing. This may be due to the possibility of a relative displacement between web and flange when a soft-layer is applied. Especially in the lower part of the flange where a lot of force has to be transferred to the flange this intersection tends to be too weak with an applied soft-layer.

During the test of the I-shaped specimens there were two specimens where even a separation of one flange was observed. One of the specimens was I-G3.15 where unintentionally different boundary conditions and a variable precompression were applied. In this test it was observed that the whole web punched through the flange at once as shown in the left photo of Figure 11.4. In contrast for test I-G10.15 it was observed that in a first step the web punched through only in the lower part as shown in the right photo of Figure 11.4 before the intersection failed over the complete height in the end.

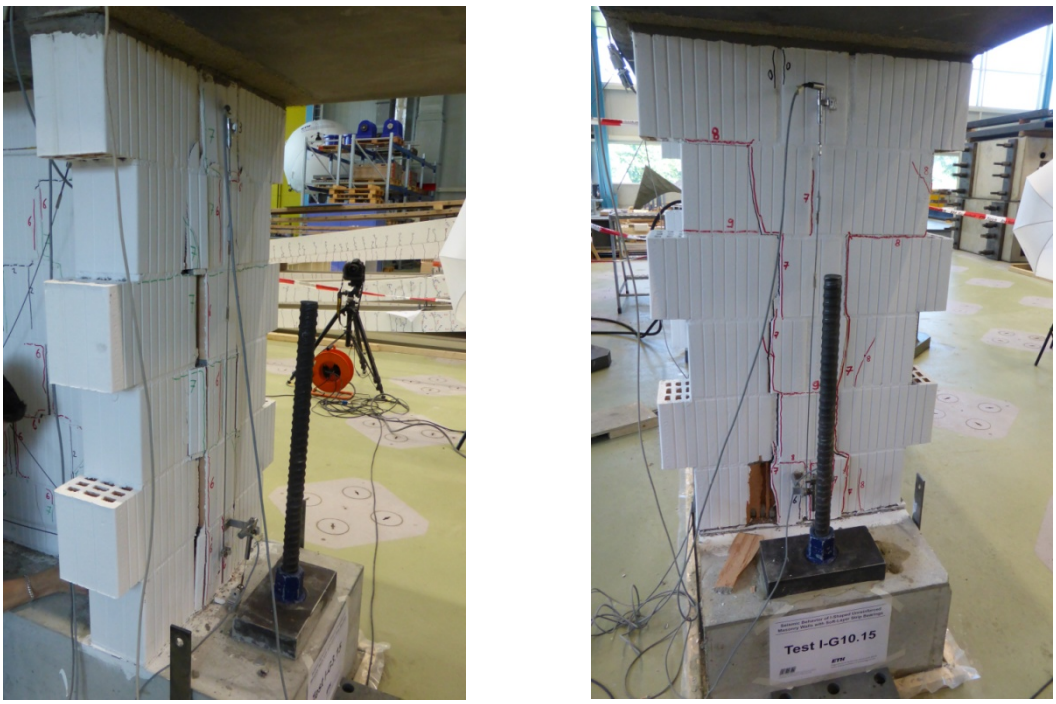

Figure 11.4: Failure of flange-web intersection, (l) I-G3.15, (r) I-G10.15

These observations made it possible to investigate the shear capacity of the flange-web intersection with a header across the shear interface every second course by recalculating the shear resistance. In a first step the shear force was determined at the time step when the intersection failed. Because there was no distinct moment of failure of the flange-web intersection the maximum shear force had to be determined approximately. It was observed that in both cases the intersection failed in the 10 mm cycle.

To calculate the shear stress in the intersection area of the flange and the web an elastic approach can be used as shown in Figure 11.5. This approach is presented in the paper about "Shear Capacity of the Flange-Web Intersections of Brick Masonry Nonrectangular Sections" by Bosiljkov et al. (2010) resulting in the following formula for the maximum shear stress in the flange-web intersection area.

$$f_{ms,exp} = \frac{V_{max} \cdot S}{I \cdot b} \qquad \textit{(Eq. 11-2)}$$

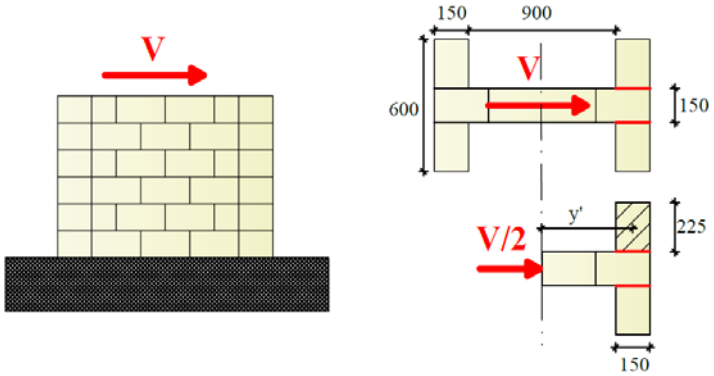

Figure 11.5: Elastic approach flange-web intersection

But with respect to the two-composite characteristics of masonry and the vertical stress distribution in the wall neglecting tension this type of analysis seems not to be accurate for this purpose. So to recalculate the shear stress a plastic approach was used for the stress distribution in the shear area between the flange and the web. Therefore the shear stress is averaged over the height of the failing flange-web intersection. As shown in Figure 11.6 this seems to be reasonable for the failure of specimen I-G3.15 but does not so for specimen I-G10.15 where only a failure of the intersection in the lower part of the flange could be observed. In this case a linear shear stress distribution in the upper part was assumed and a constant distribution at the maximum shear stress in the lower part that failed as visualized in Figure 11.6.

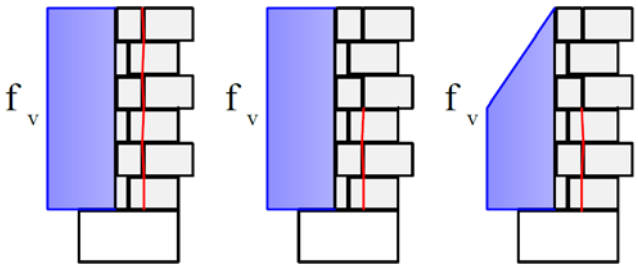

Figure 11.6: Plastic approach shear stress distribution flange-web intersection

The force that needs to be transferred from the web to the flange is estimated according to Figure 11.7. Before the flange-web intersection fails a linear vertical stress distribution at the bottom is assumed and the distribution of the shear resistance at the bottom is calculated proportional to the vertical forces in the different areas. This leads to the

maximum transferred forces from the web into the failing flanges that can be found in Table 11.4. The detailed calculation can be found in appendix F.

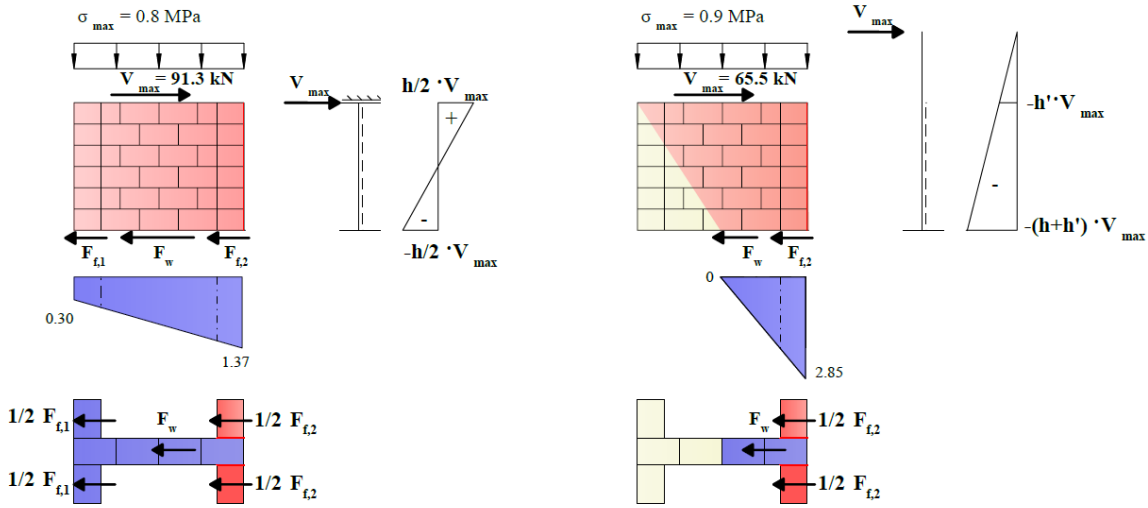

Figure 11.7: Vertical stress distribution before failure of flange-web intersection

The results of the recalculation of the shear capacity of the flange-web intersection are presented in Table 11.4. The maximum shear stress of the intersection is calculated according to the following equations.

I-G3.15: $$f_{ms,exp} = \frac{F_{trans}}{2 \cdot A_{sh}}$$ *(Eq. 11-3)*

I-G10.15: $$f_{ms,exp} = \frac{F_{trans}}{1.5 \cdot A_{sh}}$$ *(Eq. 11-4)*

Specimen	Maximum force V_{max} [kN]	Transferred force F_{trans} [kN]	Shear area A_{sh} [mm^2]	Distribution of shear stress	Shear strength $f_{ms,exp}$ [MPa]
I-G3.15	91.3	30.2	180’000	constant	0.084
I-G10.15	65.5	33.4	180’000	linear / constant	0.12
Average					0.10

Table 11.4:Shear capacity flange-web intersection

Compared to the experimental results of Bosiljkov et al. (2010) the calculated shear strength of 0.10 MPa seems to be quite low. In their tests for an intersection type with a header bonded across the shear interface every second course they found a shear strength of 1.29 MPa, so the recalculated value of Table 11.4 is less than one tenth. However it has to be taken into account that their tests were conducted with different masonry and the direction of testing was different. He tested the intersection with typical Australian brick masonry by pushing down the web vertically until failure. So there is a difference in the loading direction of 90° as also can be seen in Figure 11.8. Furthermore the incompatibility of deformations already mentioned in chapter 9.4 leads to additional

forces in the flange-web intersection which were not taken into account. Therefore it seems reasonable to get lower values but nevertheless they seem to be very small.

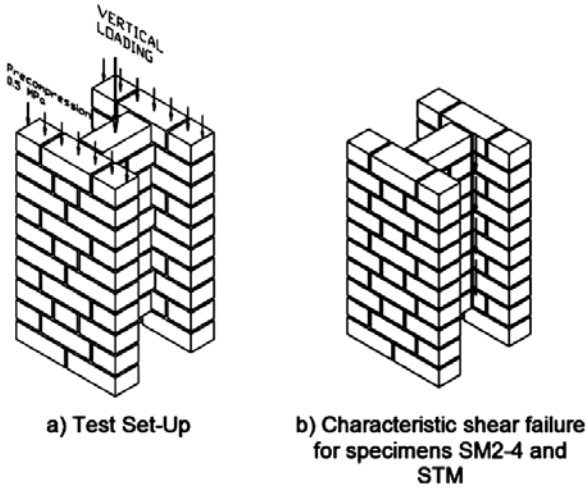

Figure 11.8: Test setup and crack pattern flange-web intersection Bosiljkov et al. (2010)

Nevertheless the shear strength out of the back-calculation can be taken as a first reference. There has to be done definitely more research with focus on this topic.

12 Comparison of Test Results with the Swiss Code SIA 266

In this chapter the shear strength of the tests in chapter 6 is compared to the shear strength according to the Swiss code SIA 266. To calculate the shear strength according to the Swiss code SIA 266 the material properties shown in Table 12.1 are used. The masonry is supposed to be standard masonry although the tests in chapter 6.3.3 revealed that the effective masonry compressive strength is too low for standard masonry. For the friction coefficient in the bed-joints a value of μ_d=0.6 is recommended by SIA 266. Taking into account the safety factor of 1.2 this leads to a characteristic value of μ=0.72 which is almost identical to the value for elastomer presented in chapter 6.3.4 and also used for the case without any layer. Therefore the friction coefficients for elastomer as well as for granulate are chosen according to Table 6.6 of chapter 6.3.4.

Material properties	
f_{xd} [MPa]	3.5
f_{yd} [MPa]	1.05
μ [-]	0.71 (no layer or elastomer) 0.44 (granulate)
μ_d [-]	0.60 (no layer or elastomer) 0.37 (granulate)
γ [kN/m^3]	13

Table 12.1:Material Properties for comparison with SIA 266

For the detailed calculation the iterative procedure mentioned in chapter 3.2.1 is used. The program code and the result-sheets are available in appendix K. There are no advices to take into account the effects of flanges so they are neglected in the calculations. The precompression was set to the levels of the conducted tests of chapter 6 so that the results can be compared. Therefore also the additional moment on top of the wall was taken into account. The results can be seen in Table 12.2. The observed shear strength is repeated for convenience.

Specimen	**Applied precompression**	**Normal force**	**Moment**	**Shear strength SIA 266**	**Shear strength observed**	**Safety factor**
	σ_v [MPa]	**N [kN]**	**M_{top} [kN]**	**V_d [kN]**	**V_{max} [kN]**	**[-]**
I-0.10	1.0	180	28.6	31.8	91.9	2.9
I-G3.10	0.6	108	18.5	20.6	56.6	2.7
I-G3.15	var.	-	-	-	101.3	-
I-G10.10	0.6	108	18.5	20.6	50.4	2.4
I-G10.15	0.9	162	23.8	26.4	71.1	2.7

Table 12.2: Comparison observed shear strength (characteristic level) with SIA 266 (design level)

The comparison of the observed shear strength with the calculated one according to the Swiss code SIA 266 reveals a safety factor from 2.4 to 2.9. For masonry a safety factor of about 2 seems to be reasonable having in mind the complex material behavior and the scattering of the material properties. Therefore the calculated safety factors tend to be too high. This underestimation of the shear strength can have different reasons. In the calculation model according to the SIA 266 some conservative assumptions were made shown on the result-sheets in appendix K. This can lead to slightly too small shear resistances. But a far more significant influence seems to be caused by the negligence of the flanges in the calculation model of the SIA 266. Therefore with the implementation of a suitable model to take into account the effect of flanges on the shear strength a more economic building guideline could be achieved. But for a reliable model more research has to be done. Nevertheless the research in the scope of this master's thesis revealed a potential of improvement since the tests showed that flanges can increase the shear strength.

13 Results of Digital Image Correlation

In the scope of this master's thesis the DIC measurements of two tests, namely I-G10.10 and I-G10.15, were analyzed. In a first step for both tests the photos taken by the camera had to be allocated to the specific lateral displacement states. One the one hand the program controlling the trigger of the camera records the time information of every trigger signal and on the other hand the camera itself records the time of each photo in its meta-data. The allocation was achieved by comparing the time step differences between the photos for both information sources as can be seen in Figure 13.1. The photos are supposed to be correctly allocated when all time step differences are equal. In a separate column the locations are indicated, where a photo was deleted during the allocation process.

Information out of **shooting info** — Information out of **meta-data** of photos

Date: 20.05.2014
Reference Photo: 010_0001

		PC-Information				Camera-Information			Evaluation	
Specimen	Photo number	Time [sec]	PC-Time	Time steps PC	Displacement [mm]	Photo-ID	Camera-Time	Time steps Camera	time step difference PC-Camera	Photo-Jumps
I-G10_10:	1	2.142	05:53:37		0.006	O10_0013	13:12:06			
I-G10_10:	2	153.142	05:56:08	00:02:31	0.007	O10_0014	13:14:37	00:02:31	00:00:00	
I-G10_10:	3	166.142	05:56:21	00:00:13	0.175	O10_0015	13:14:50	00:00:13	00:00:00	
I-G10_10:	4	173.142	05:56:28	00:00:07	0.183	O10_0016	13:14:57	00:00:07	00:00:00	
I-G10_10:	5	183.142	05:56:38	00:00:10	-0.029	O10_0017	13:15:07	00:00:10	00:00:00	
I-G10_10:	6	193.142	05:56:48	00:00:10	-0.195	O10_0018	13:15:17	00:00:10	00:00:00	
I-G10_10:	25	718.142	06:05:33	00:00:07	-0.19	O10_0037	13:24:02	00:00:07	00:00:00	
I-G10_10:	26	732.142	06:05:47	00:00:14	-0.453	O10_0038	13:24:16	00:00:14	00:00:00	
I-G10_10:	27	765.142	06:06:20	00:00:33	-0.159	O10_0039	13:24:49	00:00:33	00:00:00	
I-G10_10:	28	771.142	06:06:26	00:00:06	0.006	O10_0040	13:24:55	00:00:06	00:00:00	
I-G10_10:	29	951.142	06:09:26	00:03:00	0.008	O10_0042	13:27:55	00:03:00	00:00:00	jump
I-G10_10:	30	974.142	06:09:49	00:00:23	0.476	O10_0043	13:28:18	00:00:23	00:00:00	
I-G10_10:	31	1003.142	06:10:18	00:00:29	0.959	O10_0044	13:28:47	00:00:29	00:00:00	
I-G10_10:	32	1057.142	06:11:12	00:00:54	0.468	O10_0045	13:29:41	00:00:54	00:00:00	
I-G10_10:	33	1076.142	06:11:31	00:00:19	-0.001	O10_0046	13:30:00	00:00:19	00:00:00	

Figure 13.1: Allocation of photos DIC

In a second step the absolute displacements as well as the major and minor principal strains are calculated by means of the licensed software Vic2D. Due to the different surface planes of the web and the flanges they have to be calculated separately using the corresponding calibration (see appendix H). The results are discussed in the following sub-chapters.

13.1 Measurement Results Web

The results of the calculations allow to show and compare full-field displacements and strains at all displacement states where a photo was taken. The photos were primarily taken at the maximum lateral displacements in the pushing and pulling cycles and at the zero-positions. In the following the results at the moment of the ultimate failure of the wall specimens are discussed. The corresponding time steps are shown with a red line in the time histories of displacements and lateral forces in Figure 13.2.

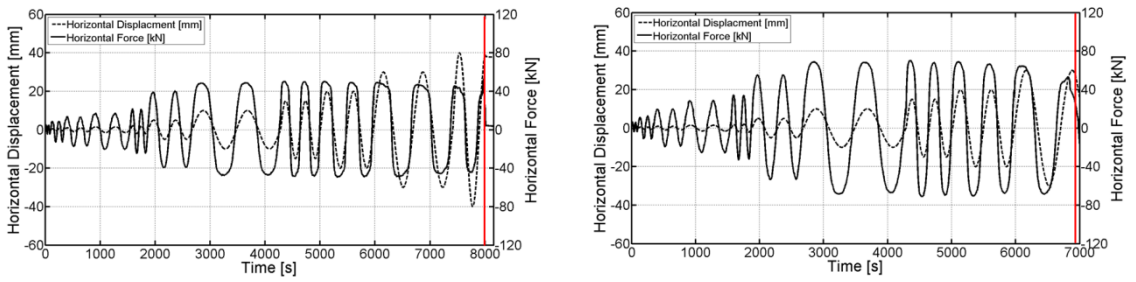

Figure 13.2: Selected time step DIC: (l) I-G10.10, (r) I-G10.15

The vertical and horizontal displacements at the selected time steps are shown in Figure 13.3 and Figure 13.4.

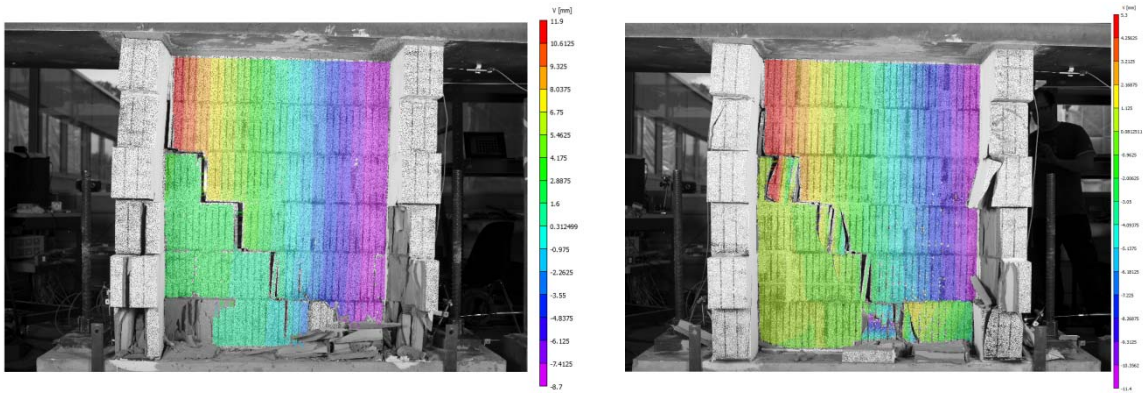

Figure 13.3: Absolute vertical displacement field web: (l) I-G10.10, (r) I-G10.15

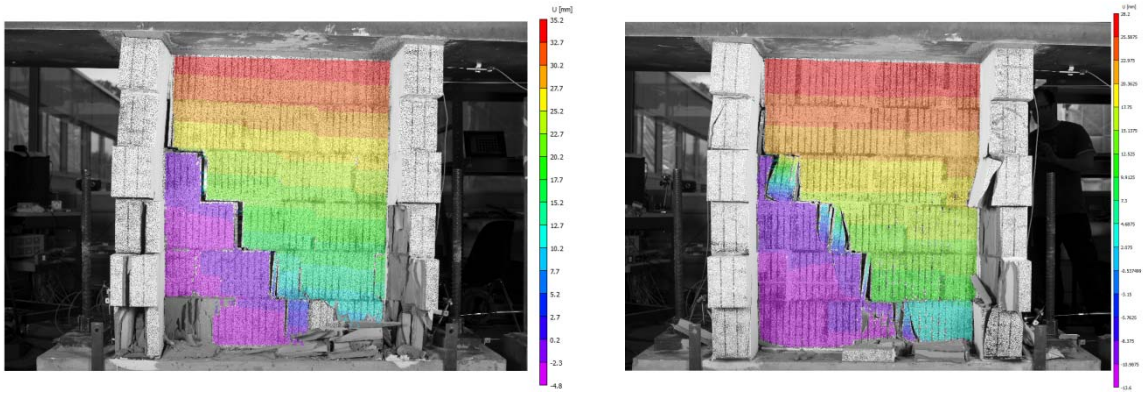

Figure 13.4: Absolute horizontal displacement field web: (l) I-G10.10, (r) I-G10.15

The absolute vertical displacements are negative on the right and positive on the left which seems to be plausible for a failure in the pushing direction (to the right). From the left to the right side of the diagonal cracks a sudden change in the vertical displacement can be observed which also seems reasonable. This change is even more distinct in Figure 13.4 because the displacements along the cracks are higher in the horizontal than in the vertical direction. On the very top of the wall the absolute horizontal displacements are the highest because at this point the lateral displacements are induced by the load transmission plate.

In the photos of test I-G10.15 an abrupt change in the absolute vertical as well as in the absolute horizontal displacements is visible along the first bed-joint in the right corner on the bottom of the wall. This seems to be a mistake in the calculation as no crack formed along this bed-joint. This failure could not be solved even several configurations in the calculation settings were changed and adjusted.

The major principal strain fields are shown in Figure 13.5 and the minor principal strain fields in Figure 13.6.

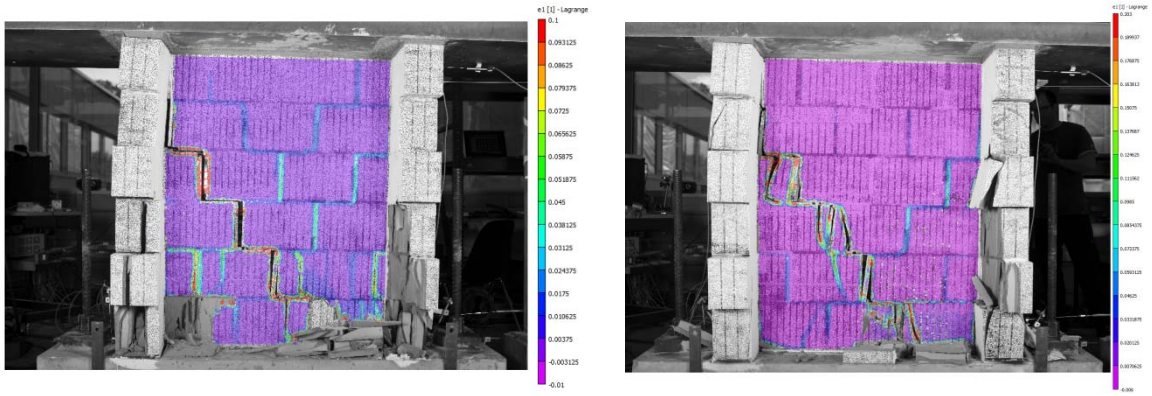

Figure 13.5: Major principal strain field web: (l) I-G10.10, (r) I-G10.15

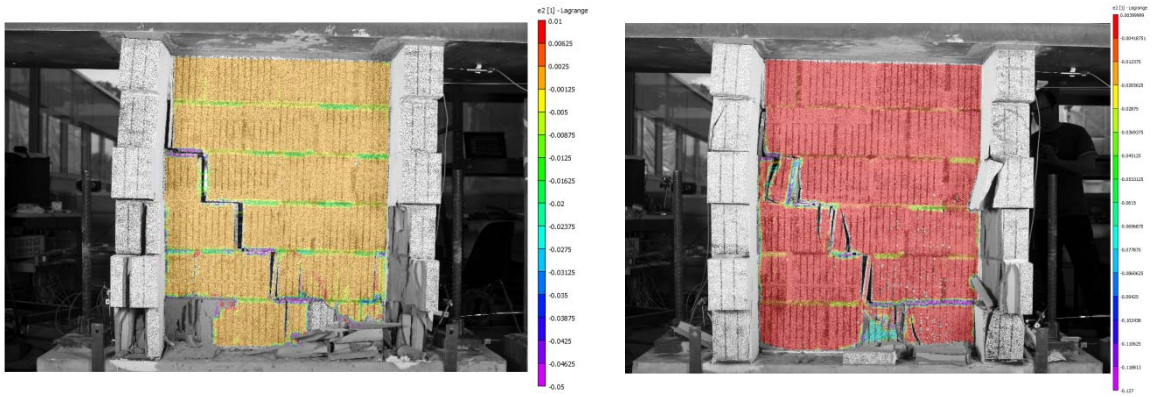

Figure 13.6: Minor principal strain field web: (l) I-G10.10, (r) I-G10.15

The major strains fields reveal positive strains in the head-joints and partially in the bed-joints where the cracks are opening. In the minor strains fields it can be observed that the mortar bed-joints are more compressed than the bricks what seems to be reasonable since the modulus of elasticity of the mortar is smaller than the one of the bricks.

13.2 Measurement Results Flanges

The surface of the flanges consists of two different planes which need a different calibration. Therefore each time six single areas had to be calculated by the software. The results showed that each time only one or two of the six areas where calculated correctly. Concerning the very long calculation time for these six areas, about five times as long as the calculation time for the web, it was supposed that the calculation algorithm had some problems to converge in all six areas at the same time. The problem was solved by

calculating the whole flanges at once and the left and right one separately by using the calibration for the back plane which is supposed to represent the displacements and strains in the flanges more accurate than the free ends of the bricks in the front plane. Therefore only the results in the back plane are correct and there are some discontinuities along the lines where the plane changes. After the calculation the images of the left and right flange could be brought together again because they were taken at the same time step. The results can be seen in the following figures.

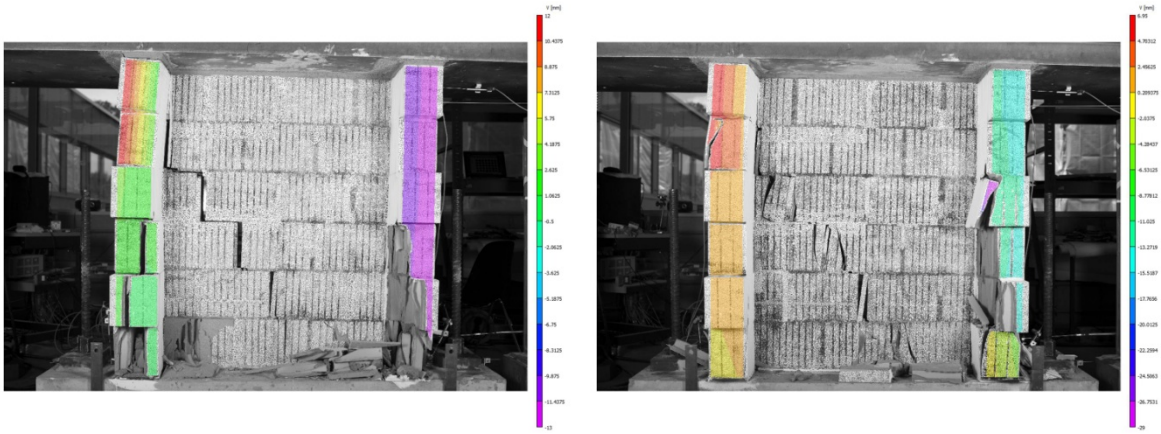

Figure 13.7: Absolute vertical displacement field flanges: (l) I-G10.10, (r) I-G10.15

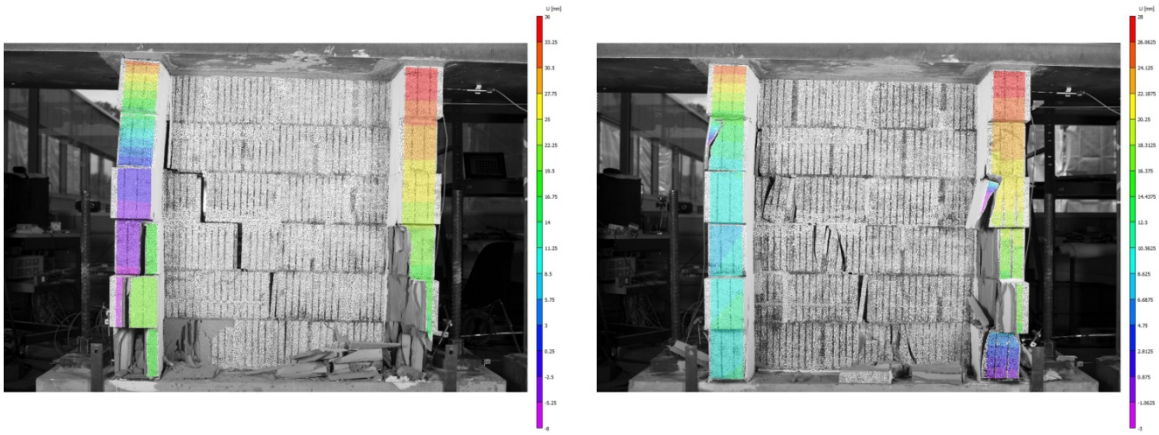

Figure 13.8: Absolute horizontal displacement field flanges: (l) I-G10.10, (r) I-G10.15

Comparing for example the absolute vertical displacements of the flanges to the results of the web it can be seen that the displacements along the vertical intersection lines at the inside of the compressed flanges are almost equal as far as it can be determined by means of the given scales. This seems plausible and confirms the reliability of the DIC data gained in two totally different calculations. The displacement accuracy that could be reached for the flanges is equal to 0.003 mm and therefore the same as for the web.

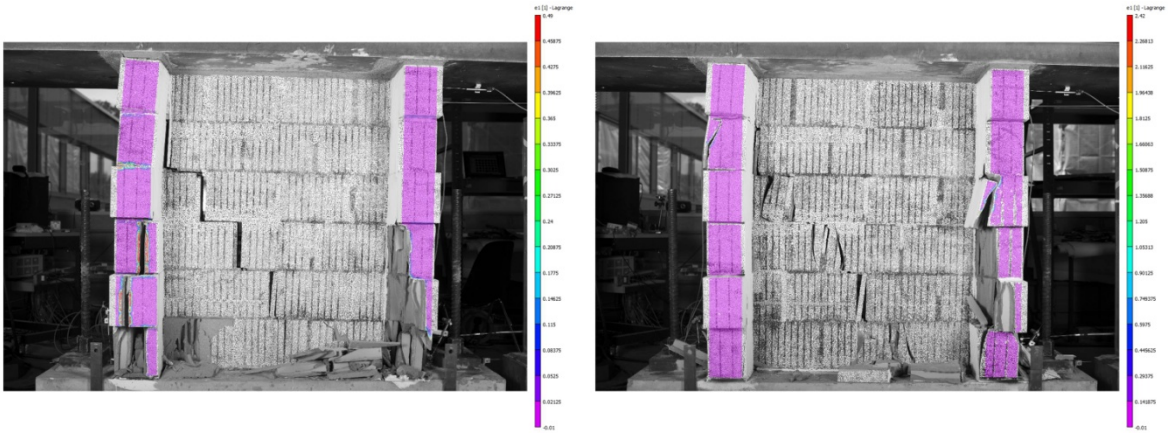

Figure 13.9: Major principal strain field flanges: (l) I-G10.10, (r) I-G10.15

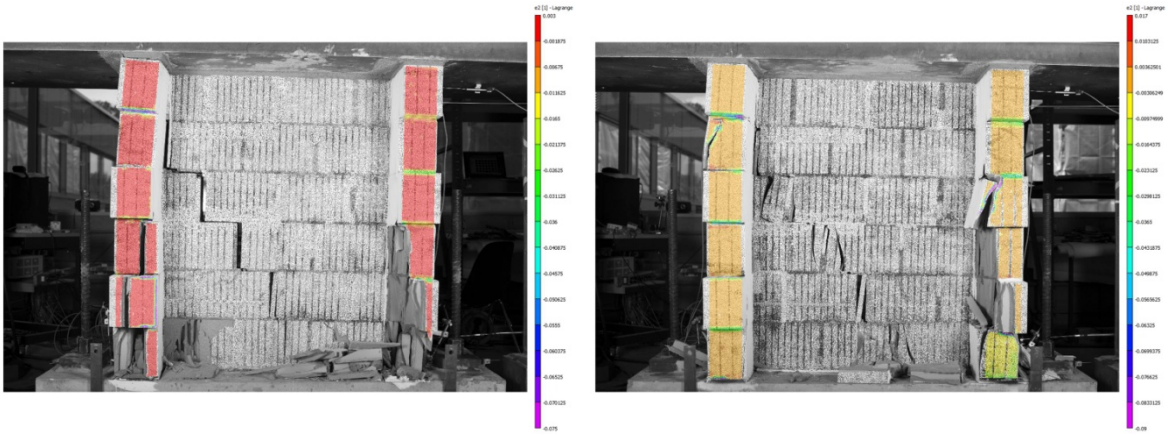

Figure 13.10: Minor principal strain field flanges: (l) I-G10.10, (r) I-G10.15

Also the results of the major and minor principal strains seem to be plausible. The discontinuities along the intersection lines of the different planes are clearly visible.

13.3 Comparison DIC and LVDT

The use of two measurement techniques during the tests allows a comparison of the results. Since the two measurements were conducted on opposite sides of the specimen small differences may occur. The DIC measurements allow not just a full-field displacement analysis but also the calculation of the displacements of a single point. Therefore the measurement of an LVDT can directly be compared to the measurement by means of DIC what has been done in Figure 13.11 and Figure 13.12 for LVDT 2 and 4 of specimen I-G10.10. The comparisons of LVDT 1 to 4 of both specimens can be found in appendix L. But it is noteworthy that not all comparisons are meaningful because some LVDT's did not measure the displacement correctly or even dropped out completely. The measurements by means of DIC therefore seem to be more solid as long as the specially prepared specimen surface stays intact. And even if the surface is partially damaged only the measurements in this limited area stop. In contrast when a fixation point of the LVDT's fails often several measurements are lost completely.

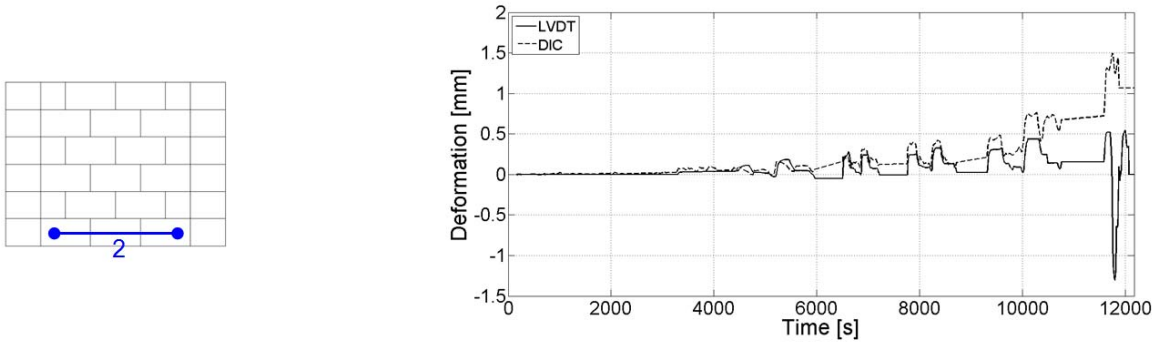

Figure 13.11: Comparison horizontal LVDT 2 with DIC Specimen I-G10.10

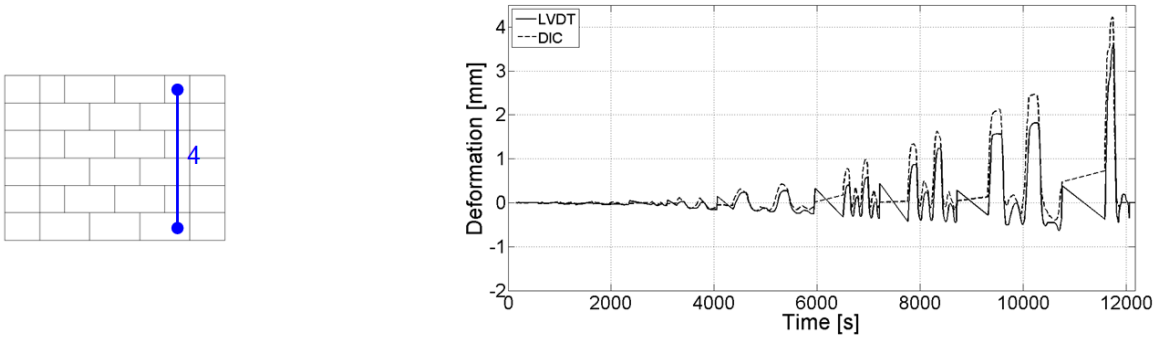

Figure 13.12: Comparison vertical LVDT 4 with DIC Specimen I-G10.10

Overall the comparisons show a very good agreement of the different measurement techniques. In both cases, for the horizontal and vertical comparison, the differences get a little bigger with increasing lateral displacements. The maximum differences are about 0.6 mm which is very accurate taking into account the different measuring sides on the specimen and the accuracy of the LVDT's themselves which is equal to 0.3% of their measuring range, so that would be around 0.2 mm in the present cases. The accuracy of the DIC is a controversial issue because it depends on many factors (Salmanpour & Mojsilović, 2013). The sources of influence were analyzed by Pan et al. (2009) and are shown in Table 13.1.

Errors related to specimen, loading and imaging	Speckle pattern
	Non-parallel between the sensor and the object surface
	Out-of-plane displacement
	Imaging distortion
	Noise during image acquisition and digitization
Errors related to the correlation algorithm	Subset size
	Correlation function
	Sub-pixel algorithm
	Shape function
	Interpolation scheme

Table 13.1:Error sources of DIC (Pan, Qian, Xie, & Asundi, 2009)

Nevertheless according to several studies the accuracy of displacements can be assumed to be equal to 0.01 pixel (Salmanpour & Mojsilović, 2013). In the present case for the

web of specimen I-G10.10 one pixel has a length of 0.29 mm resulting in an accuracy of 0.003 mm which is far more accurate than the measurements of the LVDT's.

14 Conclusions

The comparison of the experimental results with the prediction of the shear strength revealed an acceptable agreement. The calculation of the shear resistance due to the four failure modes rocking (overturning), toe crushing, sliding and diagonal tension according to the adopted modified effective pier model seems to be suitable and the governing shear strength fits well to the observations although the failure mode was not always predicted correctly.

Due to the geometry of the new test setup an additional moment was induced on top of the wall caused by a shear span of the specimens of H_0=1.75. This moment leads to a reduced shear strength compared to a cantilever boundary condition. Furthermore the resulting distinct rocking behavior leads to an overestimation of the deformation capacity in comparison to a cantilever boundary condition. Specimen I-G3.15, tested accidentally with tightened safety steel bars, showed a behavior almost corresponding to a fixed-fixed (rotations and displacements) boundary condition.

The applied granulate SLS bearing on the one hand leads to a reduced shear strength and on the other hand to an increased deformation capacity. Furthermore the energy dissipation is increased by the soft-layer. The load distributing function of the soft-layer leads to less damage at corresponding displacements but also to a distinct rocking behavior. Concerning the flanges in particular, the soft-layer may induce some harmful lateral tension stresses into the mortar and bricks leading to a splitting of the flanges. Since the splitting may also be caused by displacement-caused incompatibilities this phenomena has to be closer investigated before jumping to conclusions. Overall the soft layer has a potential to enhance the seismic performance especially from a displacement-based point of view.

The vertical load magnitude has a significant influence on the seismic response of I-shaped URM walls. It was found that an increased level of precompression leads to a higher shear strength and therefore can also lead to a change in the failure mode. In particular a change in the failure mode from toe crushing to diagonal tension was observed in the tests. The increased level of precompression also leads to a lower deformation capacity and to a stiffer response of the specimen. The initial rocking behavior observed in all tests was cut to half by increasing the precompression by 50%. The energy dissipation according to a higher level of precompression is increased. This effect is more distinct with higher lateral displacements. Concerning the damage of the SLS bearing a slightly higher damage was observed when a higher precompression was applied.

The shear strengths of the tested I-shaped walls are slightly higher than the achieved values of the equivalent rectangular walls tested by Vögeli (2014) although an additional moment was applied. Theoretical considerations revealed possible shear strength increases of about 20 to 50% according to a cantilever boundary condition. Therefore the flanges would lead not just to a small but significant increase in the shear strength. Moreover also the deformation capacity seems to be increased although a relevant part of the observed increase is caused by the higher shear span of the I-shaped specimens. Concerning the energy dissipation it was found that flanges lead to a smaller energy dissipation. No significant influence of the flanges on the damage of the soft-layer was observed.

Concerning the flange-web intersection the tests showed that at high levels of precompression the connection tends to fail due to the increased transfer of the lateral force especially in the lower part of the wall where most of the lateral force is transferred to the flange. By means of back-calculation a shear strength of the flange-web connection of $f_{ms,exp}$ = 0.10 MPa was found. This value seems to be very low and definitely has to be closer investigated in further tests.

The comparison of the test results with the Swiss code SIA 266 reveals safety factors from 2.4 to 2.9. By taking into account the additional shear strength caused by the flanges more economic guidelines could be achieved.

A good agreement is observed when the measurements of the LVDT's are compared to the results of the DIC. It can be concluded that the measurements by means of DIC are much more accurate and solid as long as the specially prepared specimen surface stays intact.

15 References

Ali, Q., Badrashi, Y. I., Ahmad, N., Alam, B., Rehman, S., & Banori, F. A. (2012). Experimental Investigation on the Characterization of Solid Clay Brick Masonry for Lateral Shear Strength Evaluation. *International Journal of Earth Sciences and Engineering, 05*(04), 782-791.

Barandun, A. (2013). *Seismic Behavior of Unreinforced Masonry Walls with Soft-Layer Strip Bearings.* Unpublished Master's Thesis, Swiss Federal Institute of Technology, Zurich.

Bosiljkov, V., Page, A. W., Simundic, G., & Žarnić, R. (2010). Shear Capacity of the Flange-Web Intersections of Brick Masonry Nonrectangular Sections. *Journal of Structural Engineering, 136*(5), 574-585.

Bundesamt für Bevölkerungsschutz. (2003). *Katastrophen und Notlagen in der Schweiz.* Bern: Bundesamt für Bevölkerungsschutz.

Chopra, A. K. (2012). *Dynamics of Structures: Theory and Applications to Earthquake Engineering.* New Jersey: Prentice Hall.

DIN EN 1052-1. (1998). *Prüfverfahren für Mauerwerk - Teil 1: Bestimmung der Druckfestigkeit*. Berlin: Beuth Verlag GmbH.

DIN EN 196-1. (2005). *Prüfverfahren für Zement - Teil 1: Bestimmung der Festigkeit*. Berlin: Beuth Verlag GmbH.

Egeter, J. S. (2014). *Seismic Behavior of I-Shaped Unreinforced Masonry Walls with Soft-Layer Strip Bearings.* Unpublished Master's Thesis, Swiss Federal Institute of Technology, Zurich.

Gams, M., & Tomažević, M. (2012). Experimental Simulation of Seismic Response of Masonry Walls. *15th World Conference on Earthquake Engineering.* Lisbon.

Lee, J.-H., Li, C., Oh, S.-H., Yang, W.-J., & Yi, W.-H. (2008). Evaluation of Rocking and Toe Crushing Failure of Unreinforced Masonry Walls. *Advances in Structural Engineering, 11*(5), 475-489.

Mojsilović, N. (2011). Strength of Masonry Subjected to In-Plane Loading: A Contribution. *International Journal of Solids and Structures, 48*(6), 865-873.

Mojsilović, N. (2012). Masonry Elements with Damp-Proof Course Membrane: Assessment of Shear Strength Parameters. *Construction and Building Materials, 35*, 1002-1012.

Pan, B., Qian, K., Xie, H., & Asundi, A. (2009). Two-Dimensional Digital Image Correlation for In-Plane Displacement and Strain Measurement: a Review. *Measurement Science and Technology, 20*(6), 17-33.

Petry, S., & Beyer, K. (2014). Influence of Boundary Conditions and Size Effect on the Drift Capacity of URM Walls. *Engineering Structures, 65*, 76-88.

Russel, A. P., Elwood, K. J., & Ingham, J. M. (2014). Lateral Force-Displacement Response of Unreinforced Masonry Walls with Flanges. *Journal of Structural Engineering, 140*(4).

Russell, A. P. (2010). *Characterisation and Seismic Assessment of Unreinforced Masonry Buildings.* PhD Thesis, University of Auckland, Auckland.

Salmanpour, A., & Mojsilović, N. (2013). Application of Digital Image Correlation for strain measurements of large masonry walls. *APCOM & ISCM.* Singapore.

Santhosh, K. V., & Roy, B. K. (2012). A Smart Displacement Measuring Technique Using Linear Variable Displacement Transducer. *Procedia Technology, 4*, 854-861.

SED. (2014, March 4). *Swiss Seismological Service*. Retrieved from www.seismo.ethz.ch

SIA 262/1. (2003). *Betonbau - Ergänzende Festlegungen*. Zürich: Schweizerischer Ingenieur- und Architektenverein.

SIA 266. (2003). *Mauerwerk*. Zürich: Schweizerischer Ingenieur- und Architektenverein.

SIA 266/1. (2003). *Mauerwerk - Ergänzende Festlegungen*. Zürich: Schweizerischer Ingenieur- und Architektenverein.

SIA D 0237. (2010). *Beurteilung von Mauerwerksgebäuden bezüglich Erdbeben*. Zürich: Schweizerischer Ingenieur- und Architektenverein.

SN EN 771-1. (2011). *Festlegungen für Mauersteine - Teil 1: Mauerziegel*. Zürich: Schweizerischer Ingenieur- und Architektenverein.

Tomaževič, M. (1999). *Earthquake-Resistant Design of Masonry Buildings.* London: Imperial College Press.

Tomaževič, M., & Weiss, P. (2012). Robustness as a criterion for use of hollow clay masonry units in seismic zones: an attempt to propose the measure. *Materials and Structures, 45*, 541-559.

Tomaževič, M., Lutman, M., & Petković, L. (1996). Seismic Behavior of Masonry Walls: Experimental Simulation. *Journal of Structural Engineering, 122*(9), 1040-1047.

Vogel, T. (2013). *Autographie Erhaltung von Tragwerken.* Zürich: ETH Zürich.

Vögeli, C. (2014). *Seismic Behavior of Unreinforced Masonry Walls with Soft-Layer Strip Bearings.* Unpublished Master's Thesis, Swiss Federal Institute of Technology, Zurich.

Yi, T. (2004). *Experimental Investigation and Numerical Simulation of an Unreinforced Masonry Structure with Flexible Diaphragms.* PhD Thesis, Georgia Institute of Technology, Atlanta.

Yi, T., Moon, F. L., Leon, R. T., & Kahn, L. F. (2005). Effective Pier Model for the Nonlinear In-Plane Analysis of Individual URM Piers. *The Masonry Society Journal, 23*(1), 21-35.

Yi, T., Moon, F. L., Leon, R. T., & Kahn, L. F. (2008). Flange Effects on the Nonlinear Behavior of URM Piers. *The Masonry Society Journal, 26*(2), 31-42.

Appendix A: Overview Test-Results

Appendix B: Summary of Conclusions

Influence of…	Shear strength	Deformation capacity	Ductility	Energy dissipation	Change in failure mode	Damage of SLS bearings
SLS bearing	-	++	--	+	No change	
Flanges*	+	+	+	-	No change	0
Increased vertical load magnitude	++	-	-	+	Change	+

*Influenced by different boundary conditions

Legend:

++	high increase	--	high reduction	0	no influence
+	increase	-	reduction		

Appendix C: Uncorrected Results of Tests

In the following the uncorrected data for each test is presented. Beside the time history of the lateral force and displacement and the hysteresis loops the measurements of all the installed LVDT's are shown. The measurements of the LVDT's were started after the target level of precompression was reached.

The arrangement of the LVDT's is repeated here for convenience.

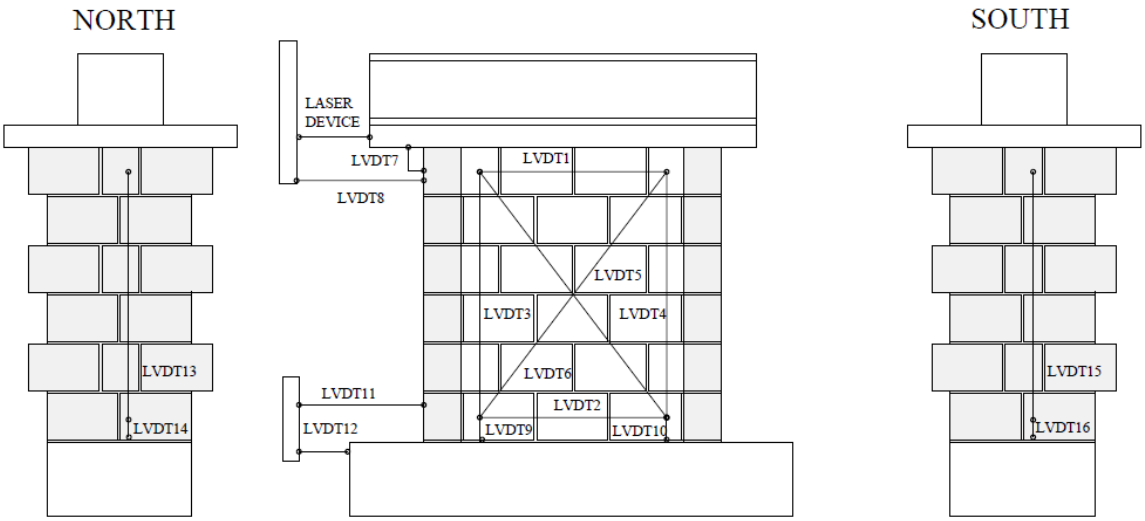

Appendix D: Crack Pattern I-Shaped URM Walls

Appendix E: Adapted Modified Effective Pier Model

Appendix F: Flange –Web Intersection

Appendix G: Checklist HIF Laboratory

Appendix H: DIC–Calibration Points and Applied vertical Stress

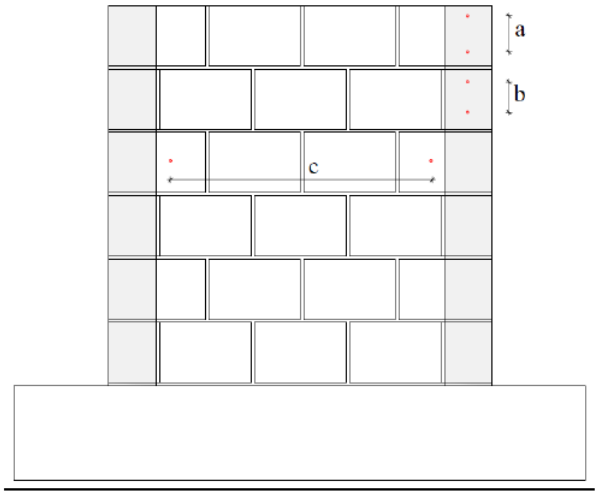

Specimen	a [mm]	b [mm]	c [mm]
I-0.10	-	-	-
I-G3.10	162	143	840
I-G3.15	115	131	804
I-G10.10	111	98	721
I-G10.15	106	118	777

Specimen	A [mm2]	fm [MPa]	force per cylinder [kN]	self-weight of setup [kN]	absolute PC [MPa]	level of PC [%]
I-0.10	315000	5.45	113.6	54.7	1	18.35
I-G3.10	315000	5.45	67.2	54.7	0.6	11.01
I-G3.15	315000	5.45	var	54.7	var	var
I-G10.10	315000	5.45	67.2	54.7	0.6	11.01
I-G10.15	315000	5.45	114.4	54.7	0.9	16.51

Appendix I: Test Report - Mortar

Appendix K: Shear Strength SIA 266

Appendix L: Comparison DIC - LVDT

Appendix M: Data CD

1_Technical Report

2_Presentations

3_Poster

4_Data

- 41_Data HIF Laboratory
  - 411_I-0.10_Final Data
  - 412_I-G3.10_Final Data
  - 413_I-G3.15_Final Data
  - 414_I-G10.10_Final Data
  - 415_I-G10.15_Final Data
- 42_Material Properties
  - 421_Data_Rilem Tests
  - 422_Data_Mortar Tests
- 43_DIC
  - 431_I-0.10
  - 432_I-G3.10
  - 433_I-G3.15
  - 434_I-G10.10
  - 435_I-G10.15
- 44_Prediction Model
- 45_Data Vögeli
- 46_Calculations SIA 266